Politecnico di Milano

School of Industrial and Information Engineering
Master of Science in Engineering Physics

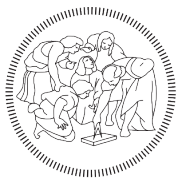

POLITECNICO
MILANO 1863

X-ray spectroscopy based investigations of the electronic states of $CeCu_2Si_2$ and YFe_2Al_{10}: absorption and photoemission

Author:
Andrea Marino

Advisor:
Prof. Dr. Giacomo Claudio Ghiringhelli
Co-advisors:
Prof. Dr. Liu Hao Tjeng
Dr. Andrea Severing
Dr. Andrea Amorese

Academic Year 2018 - 2019

MAX - PLANCK - INSTITUT

FÜR CHEMISCHE PHYSIK FESTER STOFFE

The whole work presented in these pages was carried out at the Max Planck Institute for Chemical Physics of Solids (Dresden), under the supervision of Prof. Dr. Liu Hao Tjeng, Dr. Andrea Severing and Dr. Andrea Amorese.

Contents

Acknowledgments

I am grateful to the people I met in these months: physics is not the effort of one single person, but intense teamwork.

First, I would like to thank Prof. Giacomo Ghiringhelli for suggesting me to contact the Max Planck Institute in Dresden and opening up this opportunity for me. I would also like to thank Prof. Liu Hao Tjeng for taking me on into his group for my Masters's project. His knowledge, experimental and theoretical insight into the physics of correlated electrons have been very inspiring.

My sincere gratitude goes to the two people who were the driving force behind my work, the other two Andrea(s). Andrea Severing, for sharing her knowledge and expertise, directing all the projects I was involved in and showing me the common thread and sense of the things we did, particularly during the last weeks of proofreading and revising. Andrea Amorese, for literally being at my side every day of this period, teaching me about the techniques I used, being there to check my analyses, give suggestions, discuss about physics or answer whatever question I had when, often, things were not clear. Thank you for introducing me to the world of research! It was daunting but extremely exciting at the same time.

I would also like to thank all the people working at the MPI, particularly those who helped me with my project Philipp, Stefano A., Martin, Phoebe and Simone.

I wish to thank all my friends, especially the lifelong and always encouraging Matteo, Federico, Davide, Anna, Chiara, Francesca, and Mickey, for sharing closely the years at Politecnico and facing the challenges along the way with fun, motivation and resilience.

A special thank goes to Stefano. He has been my pillar of support throughout these years.

And lastly, my deepest gratitude goes to my family. They have always reassured me in challenging times and pushed me with no constraints to do the things I wanted. Great merit for any achievement of mine is theirs.

List of Figures

List of Tables

Abstract

Strongly correlated electron systems are typically compounds consisting of transition metals or rare earths, with partially filled d or f bands. The electron-electron interaction within the d or f shell is far from being negligible and the one-electron approach fails at grasping the behaviour of these compounds. Hybridization may exist between localized d or f electrons and the electrons of other bands, such as the wide conduction bands in a metal.

In cerium based intermetallic compounds the low-temperature physics is driven by the interaction of lattice of f electrons with the itinerant conduction electrons. Such materials show a plethora of different ground-states, ranging from antiferromagnetic to unconventionally superconducting and Fermi liquid behaviour with a huge enhancement of the electrons' effective mass. This thesis focuses on the prototypical compound $CeCu_2Si_2$. It was the first unconventional superconductor to be discovered in 1979 and still arouses interest in the scientific community as theoretical and experimental efforts are trying to unveil the superconducting pairing mechanism. Since the interesting properties of the material ultimately stem from the interaction between the f and conduction electrons, knowledge of the f states is of great interest. Polarization dependent soft x-ray absorption spectroscopy has proven to be a powerful tool to obtain information about the symmetry of the $4f$ ground-state. In this work, we investigate the crystal-field ground-state wave-function of $CeCu_2Si_2$ looking at the linear dichroism of polarization dependent soft x-ray absorption spectroscopy at the Ce $M_{4,5}$ edge. In particular, this is done in the temperature range from 250 mK to 250 K, i.e. from well below the superconducting temperature ($T_c = 0.6$ K) to well above the Kondo temperature ($T_K \approx 10 - 20$ K), in order to probe the ground-state wave-function in the mK regime and assess the impact of hybridization as a function of temperature. The experimental data are supported by full-multiplet calculations based on a single-ion crystal-field approach. The overall temperature trend of the linear dichroism is well explained in terms of thermal occupation of excited crystal-field states. Small deviations are discussed in terms of hybridization of f electrons and conduction bands.

We also focus on another compound, YFe_2Al_{10}, where Kondo physics originating from the presence of f electrons is absent. The Fe, however, carries a magnetic moment that does not order down to 0.1 K. This compound has recently attracted interest since it is naturally poised on the verge of ferromagnetic order happening at 0 K and undisguised quantum critical behaviour has been observed. We report an explorative spectroscopical investigation of the role played by the Fe atoms in YFe_2Al_{10}. The valence band soft photoemission spectrum is measured and compared with preliminary density functional theory and dynamical mean-field theory calculations, performed by P. Hansmann at the Max Planck Institute for Chemical Physics of Solids (MPI CPfS), in order to evaluate the role played by correlations in the compound. The x-ray absorption spectrum at the Fe $L_{2,3}$ edge is measured and compared with reference Fe oxide samples in order to assess the valence of Fe in YFe_2Al_{10}. The magnetic moments of the Fe atoms and the magnetic susceptibility are measured by x-ray magnetic circular dichroism at the Fe $L_{2,3}$ edge.

The valence band is better fitted by the calculations when including a modest amount of Coulomb interaction strength between the Fe $3d$ electrons. The difference between the valence of Fe predicted by dynamical mean-field theory and the one suggested by the comparison of the x-ray absorption spectra with oxide references can be interpreted in terms of quite large charge fluctuations. Furthermore, x-ray magnetic circular dichroism data confirm the saturation of the static susceptibility with increasing applied fields and the values of the effective moment of the Fe atoms, in accordance with what has previously been measured with a susceptometer.

Sommario

I sistemi con elettroni fortemente correlati sono tipicamente composti che consistono in metalli di transizione o terre rare, con bande d o f parzialmente piene. L'interazione elettrone-elettrone è lontana dall'essere trascurabile e l'approccio a singolo elettrone fallisce nel cogliere il comportamento di questi composti. Ibridizzazione può esistere tra elettroni localizzati d o f e gli elettroni di altre bande, come le ampie bande di conduzione in un metallo.

Nei composti intermetallici basati sul cerio la fisica a basse temperature è diretta dall'interazione del reticolo di elettroni f con gli elettroni itineranti di conduzione. Questi materiali esibiscono una serie di stati fondamentali diversi, che vanno da antiferromagnetico a superconduttivo non convenzionale e comportamento di liquido di Fermi con un enorme aumento della massa efficace degli elettroni. Questa tesi si concentra sul composto prototipico $CeCu_2Si_2$. Fu il primo superconduttore non convenzionale a essere scoperto nel 1979 e suscita ancora interesse nella comunità scientifica in quanto approcci teorici e sperimentali cercano di svelare il meccanismo di accoppiamento superconduttivo. Poichè le proprietà interessanti del materiale discendono fondamentalmente dall'interazione tra gli elettroni f e quelli di conduzione, la conoscenza degli stati f è di grande interesse. La spettroscopia a raggi x soffici dipendente in polarizzazione si è dimostrata uno strumento efficace nell'ottenere informazioni circa la simmetria dello stato fondamentale. In questo lavoro, investighiamo la funzione d'onda dello stato fondamentale di campo cristallino in $CeCu_2Si_2$ guardando al dicrosimo lineare della spettroscopia a raggi x soffici dipendente in polarizzazione alla soglia $M_{4,5}$ del cerio. In particolare, questo è svolto nell'intervallo di temperature da 250 mK a 250 K, cioè da molto al di sotto della temperatura critica superconduttiva ($T_c = 0.6\,\mathrm{K}$) a molto al di sopra della temperatura di Kondo ($T_K \approx 10 - 20\,\mathrm{K}$), allo scopo di sondare la funzione d'onda di stato fondamentale nel regime dei mK e valutare l'impatto dell'ibridizzazione in funzione della temperatura. I dati sperimentali sono supportati da simulazioni a multipletto completo basati su un approccio a singolo ione. L'andamento complessivo in temperatura del dicroismo lineare è ben spiegato in termini di occupazione termica degli stati eccitati di campo cristallino. Piccole deviazioni sono discusse nei termini di ibridizzazione tra elettroni f e bande di conduzione.

Ci concentriamo anche su un altro composto, YFe_2Al_{10}, dove la fisica Kondo che origina dalla presenza di elettroni f è assente. Il Fe, tuttavia, presenta un momento magnetico che non porta a ordine per temperature fino a 0.1 K. Questo composto ha recentemente attratto interesse dal momento che è naturalmente in procinto di ordinarsi ferromagneticamente a 0 K ed è stato manifestamente osservato comportamento critico quantistico. Riportiamo un'indagine spettroscopica esplorativa del ruolo svolto dagli atomi di Fe in YFe_2Al_{10}. Lo spettro di fotoemissione con raggi x soffici della banda di valenza è misurato e comparato con calcoli preliminari di teoria del funzionale della densità e di teoria di campo medio dinamico, svolti da P. Hansmann presso l'Istituto Max Planck per la Chimica Fisica del Solidi (MPI CPfS), con lo scopo di valutare il ruolo delle correlazioni in questo composto. Lo spettro di assorbimento di raggi x alla

soglia $L_{2,3}$ del ferro è misurato e comparato con gli spettri di referenze di ossidi di ferro, con lo scopo di valutare la valenza del Fe in YFe_2Al_{10}. I momenti magnetici degli atomi di Fe e la suscettività magnetica sono misurati tramite dicroismo magnetico circolare a raggi x alla soglia $L_{2,3}$ del ferro. La banda di valenza è meglio riprodotta dai calcoli se si include un modesta entità di interazione coulombiana tra gli elettroni $3d$ del Fe. La differenza tra la valenza del Fe predetta dalla teoria di campo medio dinamico e quella suggerita dal confronto degli spettri di assorbimento di raggi x con ossidi di referenza può essere interpretata in termini di fluttuazioni di carica. Inoltre, i dati di dicroismo magnetico circolare a raggi x confermano la saturazione della suscettività statica con campi crescenti e i valori del momento magnetico effettivo degli atomi di Fe, in accordo con quanto precedentemente misurato tramite un suscettometro.

Chapter 1

Introduction

When dealing with matter from a quantum point of view, a single particle approach, where the constituents of the quantum system under consideration are effectively treated as independent and non-interacting entities, has proved successful in a wide variety of cases. Strongly correlated electron systems, on the other hand, have proved a much harder nut to crack. They are typically compounds of transition metals or rare earths. The electron-electron interactions are large compared to the one-electron band widths and the charge distribution of the partially filled d or f band is far from the statistical distribution of one-electron theories. A true many-body approach is needed to describe the behaviour of correlated electrons [19]. Strongly correlated systems make up a large class of insulators and electronic materials showing exotic electronic and magnetic properties, such as spin-charge separation, metal-insulator transition and heavy-fermion behaviour.

Interactions even exist between localized d or f electrons and the electrons of other bands, such as the wide conduction bands in a metal. The interplay between localized and itinerant electrons leads to a number of interesting consequences. In this Chapter, a short introduction to magnetic impurities in a metal is presented. First, the case of an isolated impurity leading to the Kondo effect is treated; then, the situation of impurities sitting regularly on lattice sites, the so-called Kondo lattice, is considered, along with the ensuing exotic behaviour leading for example to heavy-fermion or mixed-valence systems. A more detailed presentation can be found in Chapter 13 of Ref. [3] and references therein, upon which this introduction is based. Here we just report a phenomenological and qualitative introduction.

1.1 The Anderson impurity model

Let us consider a transition metal impurity in an ordinary metal. It turns out the impurity may loose or retain its magnetic moment. The former possibility can be qualitatively explained in the following way: when the localized electron level, that is for example the d level of the impurity E_d, overlaps with the continuous spectrum, electrons on this level may acquire a finite lifetime due to the possibility for, e.g., a d electron with spin $\uparrow$ to escape into the conduction band, whereby in its place a conduction electron comes, possibly with opposite spin $\downarrow$. As a result the moment is reduced or completely quenched.

The situation gets more complicated once we consider the possibility that the localized d level lies deep below the Fermi level, thus hindering the previous mechanism. The problem of the appearance of magnetic moments at impurity sites in metals was treated by P. W. Anderson [20]. The Hamiltonian he considered can be written as:

$$H = \sum_{\boldsymbol{k},\sigma} \epsilon_{\boldsymbol{k}} c^{\dagger}_{\boldsymbol{k},\sigma} c_{\boldsymbol{k},\sigma} + \epsilon_d \sum_{\sigma} d^{\dagger}_{\sigma} d_{\sigma} + U n_{d\uparrow} n_{d\downarrow} + \sum_{\boldsymbol{k},\sigma} (V_{\boldsymbol{k}} c^{\dagger}_{\boldsymbol{k},\sigma} d_{\sigma} + c.c) \tag{1.1}$$

where the first term considers the energy of the conduction electrons, the second that of the d impurity electrons, the third term accounts for the repulsive interaction between d electrons and the last term models the correlation between d and conduction electrons through a $d-c$ hybridization matrix $V_{\boldsymbol{k}}$. The simplistic outcome of the so-called Anderson impurity model can be stated in the following terms. If the impurity state E_d with spin $\uparrow$ is well below the Fermi level and is occupied, then an energy U is needed to put another electron in the same level with opposite spin $\downarrow$. One may think that the second electron is to be placed in a state at energy $E_d + U$, which for large U will lie above the Fermi level and be unoccupied. This is the case of an impurity possessing a magnetic moment. On the other hand, if the $d-c$ correlation, which is modelled as hybridization within the model, is strong, then the number of spin $\uparrow$ electrons at E_d decreases and so does the energy of the spin $\downarrow$ state located at $E_d + U n_{d\uparrow}$. These two levels will effectively move towards each other by approaching the Fermi level. If the hybridization is strong enough and U low enough, a non-magnetic state can ensue.

1.2 The Kondo effect

The Anderson model is still based upon a mean-field assumption: when one goes beyond mean-field it turns out that the magnetic impurity is screened and eventually disappears as $T \to 0$. This is the essence of the Kondo effect. Historically, it dates back to 1934 when de Haas *et. al* [1], by measuring the resistivity of a gold wire with a small amount of impurities, found a minimum at about 4 K, followed by an unexpected increase below that temperature (Fig. 1.1). An explanation was provided by Kondo in 1964 [21], when he considered the scattering of electrons with magnetic impurities in the framework of the Anderson impurity model, and predicted an antiferromagnetic exchange interaction between the localized impurity moment and the itinerant electrons in a metal. The application of third order perturbation theory shed light on a term in the scattering rate due to the magnetic impurities having a logarithmic dependenc on $\frac{1}{T}$, thus causing the resistivity to increase at very low temperature. The resistivity can be written as:

$$R(T) = R_0(T) + R_K \left(1 + c \log\left(\frac{\epsilon_F}{T}\right)\right) \tag{1.2}$$

where besides the usual scattering term $R_0(T)$ a new logarithmic term also appears. Here J is the exchange coupling constant between conduction and d electrons, R_K and c are constants. The onset of the Kondo effect is reached around the Kondo temperature T_K, giving the typical temperature scale for the behaviour of the system. The resistivity does not diverge as $T \to 0$ since the perturbation approach is no longer valid well below T_K. The results of Kondo may also be interpreted as the formation of a singlet bound-state because of the antiferromagnetic interaction of the conduction electrons with the localized moments. The magnetic impurity is *screened* by the tendency of conduction electrons with opposite spin with respect to the impurity to come closer to it and form a screening cloud. At high temperatures the process is not effective and the system behaves as a localized magnetic impurity but as $T < T_K$ the screening becomes relevant. The process is depicted in Fig. 1.2.

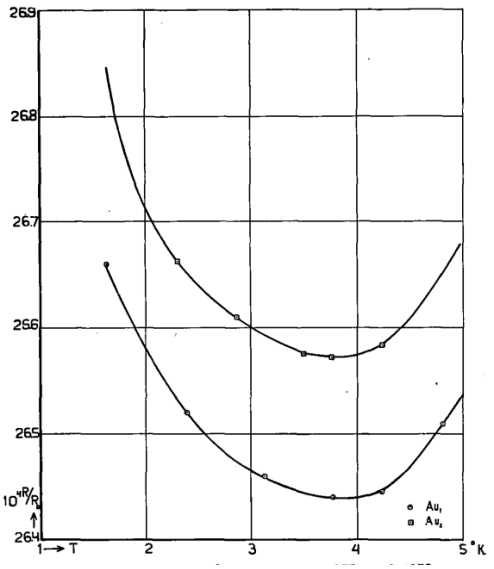

Figure 1.1: *Figure from [1]. Au resistance in the temperature range from 1 K to 5 K. The minimum is located at* $T_K \approx 4K$.

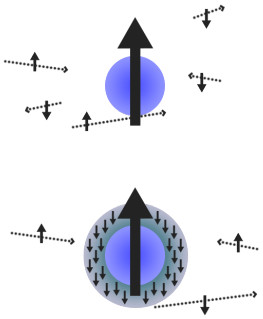

Figure 1.2: *Pictorial representation of a magnetic impurity in the sea of conduction electrons above* T_K *(top) and below* T_K *(bottom), where the Kondo screening is active, the impurity is screened by the conduction electrons and the antiferromagnetic coupling gives rise to a Kondo singlet state.*

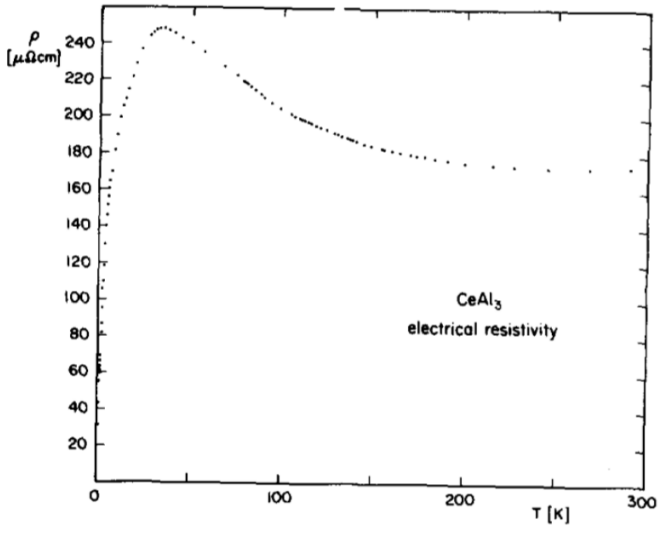

Figure 1.3: *Figure from [2]. Temperature dependence of the resistivity of a* $CeAl_3$ *single crystal. The increase of* $\rho(T)$ *at low temperature can be seen, followed by its decrease.*

1.3 Kondo lattice materials

So far only an isolated magnetic impurity in a metallic host has been considered, with energy E_d lying well below the Fermi level and thus having an occupancy close to integer. It is interesting to extend the picture to systems where multiple impurities are present on a lattice structure and where the energy of the impurities lies closer to ϵ_F. This is the case for heavy-fermion (HF) compounds. They are typically lanthanide- or actinide-based intermetallic compounds chacterized by a partially filled f shell, typically Ce or Yb compounds (having respectively one f electron and one f hole in their ground state) or other materials based e.g. on U, Pr, Sm and Pu [22, 23]. It is a well known fact that the f wave-functions are radially well localized, so that overall the scenario is that of a lattice of localized f impurities. Again, the physics is driven by the interaction of the impurities, or rather of the f electrons, with the sea of itinerant conduction electron. Also in intermetallic heavy-fermion compounds the resistivity $\rho(T)$ increases as the temperature decreases, in analogy to the Kondo effect of an impurity in a metallic host. The resistivity of $CeAl_3$ as a function of temperature is reported in Fig. 1.3 as an example. Besides the increase with decreasing T, however, another trend is also evident: as T decreases, $\rho(T)$ goes through a maximum before starting to decrease again at very low T. This is due to coherence effects that f electrons (impurities) experience when sitting on a lattice with translational symmetry.

The extension of the Anderson model to the case of a lattice of impurities leads to the so-called Anderson lattice Hamiltonian:

$$H = \sum_{\boldsymbol{k},\sigma} \epsilon_{\boldsymbol{k}} c^{\dagger}_{\boldsymbol{k},\sigma} c_{\boldsymbol{k},\sigma} + \epsilon_f \sum_{\sigma,i} f^{\dagger}_{\sigma,i} f_{\sigma,i} + U \sum_i f^{\dagger}_{i\uparrow} f_{i\uparrow} f^{\dagger}_{i\downarrow} f_{i\downarrow} + \sum_{i,\boldsymbol{k},\sigma} (V_{i,\boldsymbol{k}} c^{\dagger}_{\boldsymbol{k},\sigma} f_{\sigma,i} + c.c) \quad (1.3)$$

Eq. 1.3 is analogous to Eq. 1.1, with the first two terms considering the energy of conduction and f electrons respectively, the third term accounting for $f-f$ electron interactions and the last term modelling $c-f$ hybridization. However, it should be noted that a new index i is now being considered, running over all lattice sites. A similar approach was followed by Doniach in 1977 [24] to extend the Kondo formulation of the problem to a Kondo lattice. Once the lattice nature of the problem has been implemented, one may turn the attention to the influence of the difference between the energy of the impurity E_f and the Fermi level ϵ_F, starting from the case where $E_f << \epsilon_F$.

The competition between two opposing effects governs the system:

1. An inter-site interaction, where the conduction electrons can mediate the coupling between the f electrons via the Rudermann-Kittel-Kasuya-Yoshida (RKKY) interaction, leading to a magnetically ordered ground-state.

2. An on-site interaction, whereby the conduction electrons screen the local f magnetic moments and lead to a non-magnetic ground-state, as given by Kondo effect.

Both effects share a magnetic origin and crucially depend on the exchange coupling J and on the density of conduction electrons $N(0)$. Nevertheless, their outcome is different: the latter favours a non-magnetic ground state, where localized singlet states arise from the antiferromagnetic coupling between f and conduction electrons, while the former induces a magnetically ordered (usually antiferromagnetic) ground-state, where the conduction electrons mediate the interaction of the f moments via the oscillation of their spin density. The ordering temperatures below which the two effects are relevant also exhibit a different behaviour. The Kondo temperature scale is characterized by an exponential dependence

$$T_K \propto \frac{1}{N(0)} e^{-\frac{1}{N(0)J}} \tag{1.4}$$

The RKKY interaction, instead, scales quadratically with the exchange coupling:

$$T_{RKKY} \propto J^2 N(0) \tag{1.5}$$

On the whole then, for small J the RKKY interaction dominates and magnetic order is formed, while for larger J the Kondo lattice screening favours the formation of a paramagnetic ground-state of strongly correlated electrons. The exchange coupling constant can be written as [3]:

$$J = \frac{2V^2}{\epsilon_F - E_f} \tag{1.6}$$

where V is the hybridization strength. If $E_f << \epsilon_F$, the system possesses magnetic order at low temperature. As E_f gets closer to the Fermi energy the Kondo scale starts becoming predominant. Contextually, the occupation of the f levels is close, but not equal, to unity, with only partial delocalization of the f electrons. The presence of the Kondo effect can be linked to the appearance of a Kondo resonance peak in the density of states near the Fermi level. In this regime, then, the system may be described as a Fermi liquid, but with huge enhancement of the electron effective mass m^*. This is the heavy-fermion regime: the partial delocalization of f electrons due to hybridization leads to the formation of heavily-dressed quasi-particles, with $m^* \approx 10^3 m_0$, where m_0 is the free electron mass. Experimentally, this was first observed by Andres *et al.* in 1975 [25] by measuring a specific heat coefficient of $CeAl_3$ about a thousand times larger than that of usual metals. However, it should be noted that this is true only at low temperature, since at high T the screening is no longer effective, leading to a paramagnetic response of the localized moments and a Curie-Weiss-like dependence of the susceptibility. Fig 1.4 shows what is known as Doniach phase diagram, plotted for T as a function of the energy of the f impurity E_f.

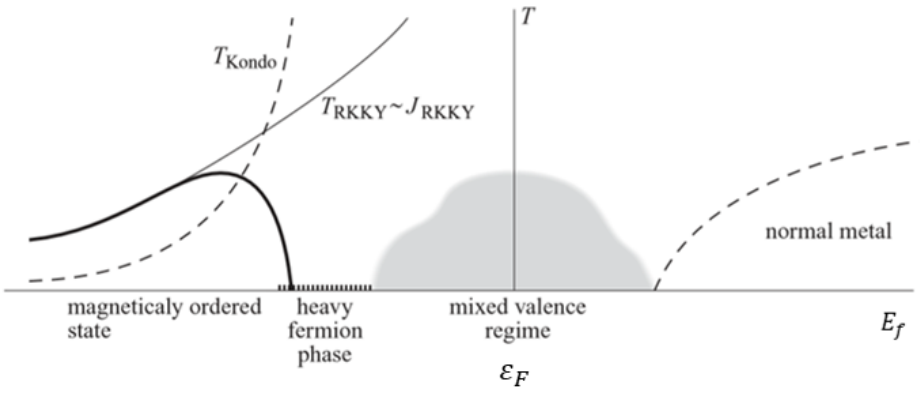

Figure 1.4: *Figure adapted from [3]. $T - E_f$ Doniach phase diagram illustrating the phases that can develop in heavy-fermion systems depending on the energy of the impurity level E_f.*

Looking at the left-hand side of Fig. 1.4 it can be seen that as E_f gets closer to the Fermi level, the magnetic ordering critical temperature T_C starts to decrease due to Kondo screening of the moments. This can lead to T_C reaching zero and the formation of

a so-called quantum critical point (QCP) at the transition between magnetically ordered and heavy-fermion regimes.

A few more words need to be spent on this matter. A QCP relates to a quantum phase transition, that is a phase transition happening at 0 K in whose vicinity the coherence length of the quantum fluctuations increases greatly. In non-zero temperature classical phase transitions the fluctuations at the critical point are governed by classical physics, the size of quantum fluctuations being much smaller than the thermal energy scale of the system k_BT. Even more outstanding among the characteristics of zero-temperature quantum phase transition is that, unlike classical finite-temperature phase transitions, the fluctuations and critical behaviour are extended to a wide portion of the phase-diagram and actively influence the properties of the system. This is because, at zero temperature, the critical fluctuations are quantum mechanical in nature, in the sense they stem from Heisenberg's uncertainty principle. As a consequence, it is of particular interest that close to the QCP the system can no longer be described as a Fermi liquid. Quantum criticality was first observed in Au-doped $CeCu_6$ [26]. It may also occur that unconventional superconductivity happens in the proximity of the QCP, possibly and usually resulting from a magnetically mediated pairing mechanism. This was first observed for $CeCu_2Si_2$ by Steglich *et al* [12] in 1979, paving the way for reasearch into unconventional superconductivity and proving that magnetism and superconductivity are not irreconcilable. Other examples are $CeCu_2Ge_2$ [27], $CeCoIn_5$ [28], $CeIn_3$ [29] and many others like $CePd_2Si_2$ [30] or $CeRh_2Si_2$ [31].

On the whole, it is clear that the class of materials under consideration exhibits a rich variety of ground-states, leading to a multitude of fundamental and exotic physical phenomena and posing the experimental and theoretical challenge to gain insight into them. Tuning J it is possible to move from a magnetically ordered ground-state to the heavy-fermion regime. In between the two, one may also find a QCP, possibly surrounded by a superconducting dome, below which unconventional superconductivity is observed. The interplay derives from the magnitude of the exchange coupling constant J, whose magnitude depends on the energy difference between the f levels E_f and the Fermi level ϵ_F, as given by Eq. 1.6. When $\epsilon_F - E_f$ becomes small, then J_{ex} gets larger and the system moves from an AFM ground-state to a heavy-fermion behaviour (see Fig. 1.4). The tuning of J is practically achieved by some external control parameter δ, which can be pressure, chemical substitution or a magnetic field, intervening in influencing the lattice density and therefore the degree of hybridization. This is summarized in the $T-J$ Doniach phase-diagram, reported in Fig. 1.5, where the rich physics of heavy-fermion systems is displayed.

Nonetheless, this is not the end of the story. Looking again at Fig. 1.4, if E_f gets very close to ϵ_F, hybridization effects become very strong and the occupation of the f shell varies noticeably from integer. This is the *mixed-valence* regime. The ground-state wave-function can be written as a superposition of states accounting for the different f electron configurations. Usually Ce adopts the valence 3^+, so that the $4f$ configuration is f^1. For an intermediate valence Ce compound, however, as e.g. $CePd_3$ [32], the ground-state is a mixture of $4f^n$ configurations and can be written as:

$$|\psi_{ground}\rangle = c_0 \left|f^0\right\rangle + c_1 \left|f^1\underline{L}\right\rangle + c_2 \left|f^2\underline{\underline{L}}\right\rangle \tag{1.7}$$

where, besides the usual trivalent contribution f^1, the tetravalent and bivalent contributions f^0 and f^2 coming from hybridization to the conduction electrons is also present. $\underline{L}$ and $\underline{\underline{L}}$ denote the number of ligand holes. The f^1 configuration is still the dominating one, but there are now sizeable contributions of f^0 and also f^2. The total valence of Ce in $CePd_3$ is ≈ 2.8 [33].

Finally, if the f levels come even closer to ϵ_F to the point of going above it, the f electrons will spill into the conduction band and the system will be a non-magnetic

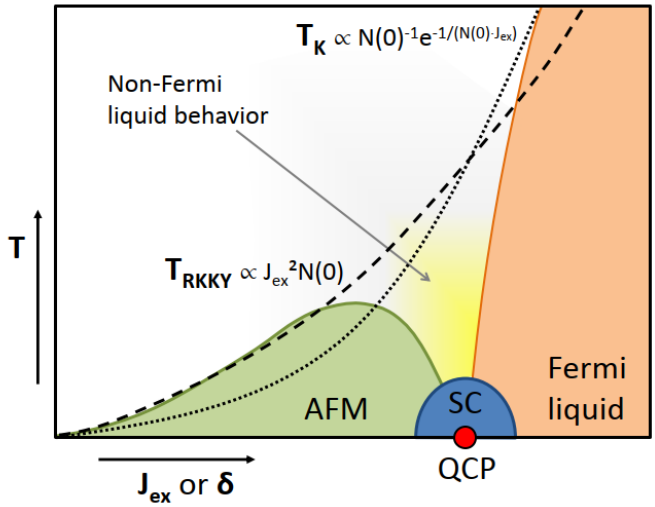

Figure 1.5: *Figure from [4]. Doniach phase diagram illustrating the competition between the the RKKY and Kondo interactions, as a function of the exchange coupling J_{ex} or of an external control parameter δ. If $T_{RKKY} < T_K$ the ground-state is localized and antiferromagnetic, if $T_K > T_{RKKY}$ the ground-state is a Fermi liquid, with partial delocalization of the f electrons and heavy-fermion behaviour. In the region between the two regimes a quantum critical point may be found, where the system can be described as a non-Fermi liquid and unconventional superconductivity may appear.*

normal metal with empty f levels.

1.4 Crystal-field

When a magnetic ion sits within a lattice, not only are the f electrons affected by the hybridization with the surrounding conduction electrons, but they also experience the crystal-field that originates from the surrounding atoms and which reflects the local point symmetry. The ensuing wave-function of the crystal field states shows a strong anisotropy, which may affect their interaction with the environment. For example, in case of hybridization of $4f$ and conduction electrons, symmetry aspects are important. For the introduction of the crystal-field formalism it is useful to start from the consideration of the localized electrons in an hypothetical free atom and to progressively consider the interactions adding up to a satisfactory description of the localized states located in a crystalline environment.

1.4.1 From an isolated atom to the crystal-field

Seeing an atom as a system with N electrons of mass m and charge -e and a nucleus with a very large mass compared to that of the electrons and charge Ze, the Hamiltonian for an atomic system can be written as:

$$H = H_0 + H_{SO} + H_{ee} \tag{1.8}$$

where H_0 comprises the kinetic energy of the electrons and their interaction with the nucleus:

$$H_0 = \sum_i \frac{p_i^2}{2m} - \sum_i \frac{Ze^2}{r_i} \tag{1.9}$$

H_{SO} takes the spin-orbit interaction into account:

$$H_{SO} = \sum_i^N \zeta_i(r) \mathbf{l}_i \cdot \mathbf{s}_i \tag{1.10}$$

and H_{ee} considers the interaction between electrons:

$$H_{ee} = \frac{1}{2} \sum_{i \neq j} \frac{e^2}{r_{ij}} \tag{1.11}$$

The summations above run over all electrons. p_i and r_i are the electrons momentum and position, ζ_i the spin-orbit coupling constants, $\boldsymbol{l_i}$ and $\boldsymbol{s_i}$ the angular and spin momenta.

One may now consider the atom as sitting in a crystalline environment. The attempts at this endavour by the so-called crystal-field theory date back to the 1930s [34, 35] and are based upon the following assumption: in a purely electrostatic model, the attention is drawn on a single atomic site within the crystal and the crystalline environment is modelled by an electrostatic potential exerted by the neighbouring atoms, seen as point-charges, on the outer electron shell of the ion in the atomic site under consideration. This is an effective model, in an actual crystal structure atoms are kept together by various and complex bonding mechanisms. However, the $4f$ shell in the lanthanide series (see Fig. 1.6) is particularly well-localized, so that the overlap with orbitals from neighboring ligands is very small. In this sense the wave-functions have atomic-like character and the ionic picture upon which crystal-field theory is based does indeed work well.

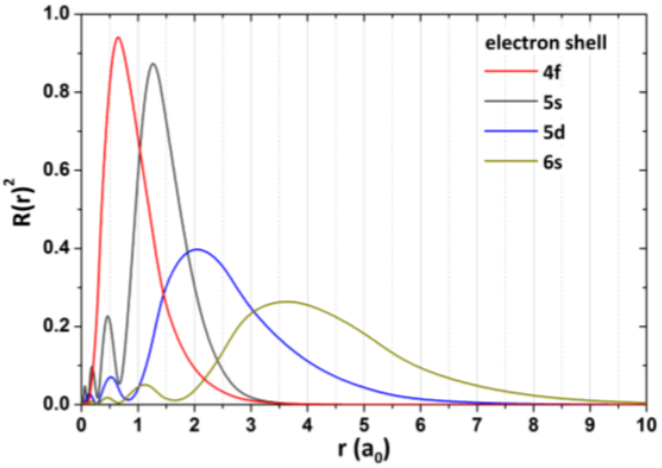

Figure 1.6: *Radial part of the wave-function of $4f$, $5s$, $5d$ and $6s$ electrons as calulated by the Hartree-Fock method for Ce^{3+} [4].*

A crystal-field Hamiltonian $H_{CF} = -eV_{CF}$ is added to the Hamiltonian for an atomic system, where V_{CF} is the crystal-field or Madelung potential exerted by the surrounding point-like charges on the central ion under consideration. In order to assign the good quantum numbers to the problem it is useful to compare the magnitude of

the crystal-field potential with the other terms of the free-atom Hamiltonian. For rare earths systems one finds $H_{CF} < V_{SO} < H_{ee}$, while for transition-metal complexes $V_{SO} < H_{CF} < H_{ee}$ [36].

1.4.2 Parametrization of the crystal-field

In order to provide an adequate mathematical description of the crystal-field potential, we consider the eigenfunctions of the free-atom Hamiltonian $\Psi_{nlm}(r,\theta,\phi) = R_n^l(r)Y_l^m(\theta,\phi)$, written as the product of a radial and an angular part following the usual notation for the quantum numbers n, l and m. We then apply an analogous separation to the crystal-field potential by expanding it in spherical harmonics $Y_l^m(\theta,\phi)$:

$$V_{CF}(r,\theta,\phi) = \sum_{k=0}^{\infty}\sum_{m=-k}^{k} A_k^m r^k \sqrt{\frac{4\pi}{2k+1}} Y_k^m(\theta,\phi) = \sum_{k=0}^{\infty}\sum_{m=-k}^{k} A_k^m r^k C_k^m(\theta,\phi) \quad (1.12)$$

where Y_k^m are the renormalized spherical harmonics:

$$Y_k^m(\theta,\phi) = \sqrt{\frac{(k-m)!}{(k+m)!}} P_k(\cos\theta) e^{im\phi} \quad (1.13)$$

and $P_k(\cos\theta)$ are the Legendre polynomials. The matrix elements $\langle\Psi_p| H_{CF} |\Psi_j\rangle$ of the crystal-field Hamiltonian are given by:

$$H_{p,j}^{CF} = -e\sum_{k=0}^{\infty}\sum_{m=-k}^{k} A_k^m \left\langle R_{n_p}^{l_p}(r)\right| r^k \left|R_{n_j}^{l_j}(r)\right\rangle \sqrt{\frac{4\pi}{2k+1}} \left\langle Y_{l_p}^{m_p}(\theta,\phi)\right| Y_k^m(\theta,\phi) \left|Y_{l_j}^{m_j}(\theta,\phi)\right\rangle \quad (1.14)$$

The integrals over the radial part $\left\langle R_{n_p}^{l_p}(r)\right| r^k \left|R_{n_j}^{l_j}(r)\right\rangle$ can be calculated for a free atom in the Hartree-Fock approximation using Cowan's code [37]. The integrals over the angular part $\left\langle Y_{l_p}^{m_p}(\theta,\phi)\right| Y_k^m(\theta,\phi) \left|Y_{l_j}^{m_j}(\theta,\phi)\right\rangle$ can be calculated analytically. This leaves us with the A_k^m to be determined experimentally to fully characterize the crystal field. However, since the radial wave functions in a free atom may be different to those of an atom in a solid, it is convenient to redefine such parameters by including the integral over the radial part:

$$\tilde{A}_k^m = A_k^m \left\langle R_{n_p}^{l_p}(r)\right| r^k \left|R_j^{l_j}(r)\right\rangle \quad (1.15)$$

All the summations above involve an infinite number of k values. Fortunately, several constraints intervene in limiting the number of parameters to a finite and manageable set.

Constraints on the crystal-field parameters

In this paragraph the constraints limiting the number of necessary crystal-field parameters are schematically reported:

- The integrals over the angular part in equation 1.14 can be expressed using the $3j$ symbols [37]. From a mathematical viewpoint, a triangular inequality holds, involving that only those matrix elements with $k \leq l_p + l_j$ can be non-vanishing.

- it can be seen that $k + l_p + l_j$ must be even, since otherwise the angular term $\left\langle Y_{l_p}^{m_p}(\theta,\phi)\right| Y_k^m(\theta,\phi) \left|Y_{l_j}^{m_j}(\theta,\phi)\right\rangle$ in 1.14 would involve the integration of an odd function, which vanishes.

- Since the Hamiltonian matrix has to be hermitian, that is $H_{pj} = H_{pj}^*$, we must have $A_k^m = (-1)^m A_k^{-m}$. This means that it is only sufficient to determine the parameters A_k^m with $m \geq 0$

- The crystal-field potential must be invariant under symmetry operations of the point group relating to the symmetry of the cluster. If there is a C_z^q symmetry axis, then the crystal-field potential itself must comply to that:

$$V_{CF}(r,\theta,\phi) = V_{CF}\left(r,\theta,\phi+\frac{2\pi}{q}\right)$$

  Since the ϕ dependence in 1.14 is contained in the $e^{im\phi}$ factor of the spherical harmonics, this implies $e^{im\phi} = e^{im\left(\phi+\frac{2\pi}{q}\right)}$, which is true if

$$m = Nq$$

  where N is an integer. In turn, it follows that the crystal-field can only mix states that differ in the J_z quantum number by the order of the rotational symmetry, given this the symmetry axis is chosen as the quantization axis:

$$\Delta J_z = q \tag{1.16}$$

1.4.3 Ce^{3+} in tetragonal crystal-field

In this section, we deal with the derivation of the crystal-field states of the rare-earth Ce^{3+} ion in tetragonal crystal-field as an example. In Chapter 3 the crystal-field of $CeCu_2Si_2$ was studied.

For rare-earths $H_{CF} < V_{SO} < H_{ee}$ with these three terms being of the order of 10 meV, 100 meV and 1 eV. The Coulomb repulsion has to be considered first and since the eigenstates of the Coulomb operator are also the eigenstates of the spin and angular momentum operators, the resulting multiplets can be described by the quantum numbers S and L. Spin-orbit is weaker than the Coulomb repulsion; thus, the LS coupling scheme (or Russel-Saunders) can be applied, leading to the coupling of $\mathbf{L}$ and $\mathbf{S}$ to the total angular momentum $\mathbf{J}$ and a further multiplet splitting of different J. Since the coupled spin and angular momentum are in principle no longer conserved independently, whereas $\mathbf{J} = \mathbf{L} + \mathbf{S}$ is, J is the appropriate quantum number, L and S only to a good approximation. Each J level is $(2J+1)$-fold degenerate. The introduction of the crystal-field breaks the spherical symmetry of the system and J is not rigorously a good quantum number any longer. Nevertheless, since for rare earths the crystal field splitting is usually small compared to the spin-orbit splitting it is still reasonable to use J as a quantum number. The $(2J+1)$-fold degeneracy of each spin-orbit split level is lifted by the crystal field. Let us now focus on the Ce^{3+} ion and apply the considerations reported above to this specific case of a crystal-field with tetragonal symmetry.

The starting point is the $4f^1$ configuration, whose LS terms are perturbed and split by the spin-orbit interaction first and by the crystal-field then. The Hund's rule ground state has $L = 3$ and $S = \frac{1}{2}$. Because of spin-orbit coupling, states with different J are split ($J = |L \pm S| = \frac{5}{2}, \frac{7}{2}$) and since the shell is less than half-filled, the ground state is the $J = \frac{5}{2}$ multiplet. The further $(2J+1)$-fold degeneracy of the J_z states within the two multiplets is then lifted by the crystal-field. However, since those J_z states are

generally not eigenstates of the crystal field Hamiltonian too and do not comply to its symmetry, they are not simply split but also intermixed.

As for the parametrization of the crystal field acting on $4f$ electrons, $l_p = l_j = 3$, meaning that because of the constraints mentioned in Section 1.4.2 the allowed values for k are $k = 0, 2, 4, 6$. The expression of the crystal-potential 1.12 reduces to:

$$V_{CF} = A_0^0 r^0 C_0^0 + \sum_{m=-2}^{2} A_2^m r^2 C_2^m + \sum_{m=-4}^{4} A_4^m r^4 C_4^m + \sum_{m=-6}^{6} A_6^m r^6 C_6^m \tag{1.17}$$

The tetragonal symmetry of the crystal-field is described by the D_{4h} point group. The presence of a four-fold rotational symmetry allows for a reduction of the values of m to $m = 0, 4$. The crystal-field potential can then be written as:

$$V_{CF} = A_0^0 r^0 C_0^0 + A_2^0 r^2 C_2^0 + A_4^0 r^4 C_4^0 + A_4^4 (C_4^4 + C_4^{-4}) + A_6^0 r^6 C_6^0 + A_6^4 r^6 (C_6^4 + C_6^{-4}) \tag{1.18}$$

Furthermore, since we can only consider A_k^m terms with positive m, we are now left with six parameters to characterize the crystal-field. These parameters, however, are the mere coefficients of an expansion, with no straightforward physical interpretation. In order to get a better insight into the physics, it is useful to look at the at crystal-field Hamiltonian matrix, written in the basis of the J, J_z states that are the eigenstates of the spherical Hamiltonian. Without entering into the details of its composition, I just report its overall structure here:

$$\begin{bmatrix} H_{J=\frac{7}{2}}(A_k^m, \zeta) & H_{mix}(A_k^m) \\ H_{mix}(A_k^m) & H_{J=\frac{5}{2}}(A_k^m, \zeta) \end{bmatrix} \tag{1.19}$$

It is made up of four submatrices: the two on the diagonal describe the $J = \frac{7}{2}$ and $J = \frac{5}{2}$ multiplets respectively, while the off-diagonal submatrices refer to the mixing between them. The presence of these off-diagonal terms is due to the fact the the J, J_z states are no longer the eigenstates of the crytal-field Hamiltonian, which induces a mixing between them. Off-diagonal terms are also present in the $J = \frac{5}{2}$ and $J = \frac{7}{2}$ sub-matrices for the same reason, involving a mixing of pure J_z states within the same multiplet. However, one should consider that the mixing between the J_z states from the the $J = \frac{5}{2}$ multiplet with the J_z states from the the $J = \frac{7}{2}$ multiplet can be neglected, since in rare earths the spin-orbit coupling is much larger than the crystal-field. In other words the H_{mix} sub-matrices in eq 1.19 are unimportant. Furthermore, the parameter A_0^0 is only present on the main diagonal of the Hamiltonian matrix and thus only involves an energy shift of all crystal-field states, without implying mixing between them. From a physical point of view such a term represent the monopole, isotropic part of the crystal-field expansion. The same is true for the spin-orbit coupling constant ζ. In the following we may as well neglect these two terms and consider the $J = \frac{5}{2}$ submatrix, since we are only interested in the ground-state and first excited states:

$$\begin{bmatrix} \frac{1}{21}(-6A_2^0 + A_4^0) & 0 & 0 & 0 & \frac{1}{3}\sqrt{\frac{2}{7}}A_4^4 & 0 \\ 0 & \frac{2A_2^0}{35} - \frac{A_4^0}{21} & 0 & 0 & 0 & \frac{1}{3}\sqrt{\frac{2}{7}}A_4^4 \\ 0 & 0 & \frac{8A_2^0}{35} - \frac{2}{21}A_4^0 & 0 & 0 & 0 \\ 0 & 0 & 0 & \frac{A_2^0 8}{35} - \frac{2}{21}A_4^0 & 0 & 0 \\ \frac{1}{3}\sqrt{\frac{2}{7}}A_4^4 & 0 & 0 & 0 & \frac{2A_2^0}{35} - \frac{A_4^0}{21} & 0 \\ 0 & \frac{1}{3}\sqrt{\frac{2}{7}}A_4^4 & 0 & 0 & 0 & \frac{1}{21}(-6A_2^0 + A_4^0) \end{bmatrix} \tag{1.20}$$

Notice that only three parameters (A_2^0, A_4^0 and A_4^4) are now needed to characterize the crystal-field. As mentioned in the previous section, only those states differing in their J_z quantum number by the order of the rotational symmetry axis in the quantization direction can mix. In the present case, the four-fold rotational symmetry axis of the tetragonal crystal-field imposes $\Delta J_z = 4$, meaning that the $J_z = \pm\frac{1}{2}$ state can only mix with the $J_z = \mp\frac{7}{2}$ states, so that the $J_z = \pm\frac{1}{2}$ is a pure state in the $J = \frac{5}{2}$ multiplet. Furthermore, $J_z = \pm\frac{5}{2}$ can mix with $J_z = \mp\frac{3}{2}$. This is also immediately evident from 1.20: the matrix is written on the basis of the J_z states and its colomns, from left to right, and lines, from top to bottom, correspond to $J_z = +\frac{5}{2}, +\frac{3}{2}, +\frac{1}{2}, -\frac{1}{2}, -\frac{3}{2}, -\frac{5}{2}$. It can be seen that the $J_z = \pm\frac{1}{2}$ of the $J = \frac{5}{2}$ multiplet state does not mix indeed.

Finally, we come to the eigenstates of the tetragonal crystal-field written in terms of the $\left|J = \frac{5}{2}, J_z\right\rangle \equiv |J_z\rangle$ pure states:

$$\begin{aligned} |1\rangle = \Gamma_7^- &= \alpha \left|\pm\frac{5}{2}\right\rangle - \beta \left|\mp\frac{3}{2}\right\rangle \\ |2\rangle = \Gamma_6 &= \left|\pm\frac{1}{2}\right\rangle \\ |3\rangle = \Gamma_7^+ &= \beta \left|\pm\frac{5}{2}\right\rangle + \alpha \left|\mp\frac{3}{2}\right\rangle \end{aligned} \tag{1.21}$$

with energies E_1, E_2 and E_3, which are functions of the A_k^m parameters and of either α or β. The last two parameters have to comply, because of normalization, to:

$$\alpha^2 + \beta^2 = 1 \tag{1.22}$$

Plots of the charge density of the pure J_z states within the $J = \frac{5}{2}$ multiplet are reported in Fig. 1.7 and a schematic illustration of the energy levels scheme for Ce 3^+ in a tetragonal crystal field is reported in Fig. 1.8.

The A_k^m parameters do not have any direct physical meaning. For this reason, again, we prefer to consider more physical quantities and describe the states in equation 1.21 in terms of α (also known as mixing parameter) and the crystal field splittings ΔE_{21} and ΔE_{31}, instead of A_2^2, A_4^0 and A_4^4. Upon diagonalizing matrix 1.20 one finds the relation between the A_k^m, ΔE_{21}, ΔE_{31} and α:

$$\begin{aligned} \Delta E_{21} &= \frac{1}{105}\left(36A_2^0 + 15A_4^0 - \sqrt{(}4(9A_2^0 - 5A_4^0)^2 + 350(A_4^4)^2)\right) \\ \Delta E_{31} &= -\frac{2\left(624A_2^0 + 260A_4^0 + 53\sqrt{4(9A_2^0 - 5A_4^0)^2 + 350(A_4^4)^2}\right)}{11025} \\ \alpha &= -\frac{1}{\sqrt{1 + \frac{-18A_2^0 + 10A_4^0 + \sqrt{324(A_2^0)^2 - 360A_2^0A_4^0 + 100(A_4^0)^2 + 350(A_4^4)^2}}{350(A_4^4)^2}}} \end{aligned} \tag{1.23}$$

and

$$\begin{aligned} A_2^0 &= \frac{5}{12}((-5 + 6\alpha^2)\Delta E_{21} + 4\Delta E_{32}) \\ A_4^0 &= \left(\frac{3}{2} - 6\alpha^2\right)\Delta E_{21} + 3\Delta E_{31} \\ A_4^4 &= -3\sqrt{\frac{7}{2}}\alpha\sqrt{1-\alpha^2}\Delta E_{21} \end{aligned} \tag{1.24}$$

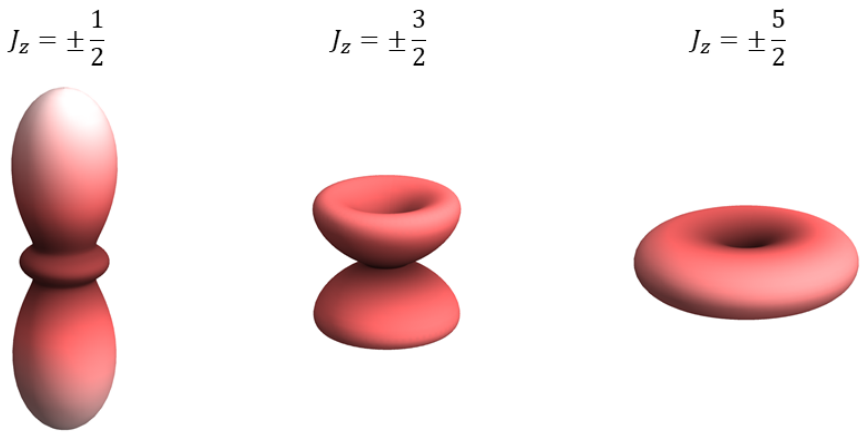

Figure 1.7: *Charge densities of the crystal-field split $J = \frac{5}{2}$ multiplet pure J_z states.*

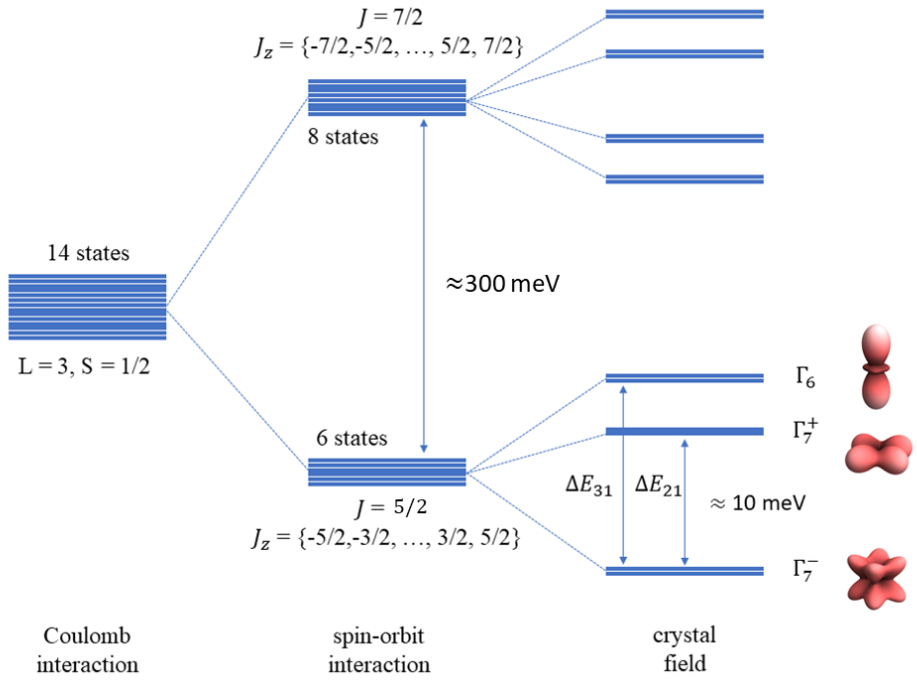

Figure 1.8: *Energy levels scheme of Ce 3^+ in a tetragonal crystal-field. The spin-orbit interaction splits fourteen degenerate states into the six-fold degenerate $J = \frac{5}{2}$ and eight-fold degenerate $J = \frac{7}{2}$ multiplets. The crystal field lifts the $(2J + 1)$- fold degeneracy of these two multiplets. The charge density of the lowest crystal-field states is also plotted, in the case of a mixing parameter $\alpha = 0.3$.*

1.5 Aspects investigated in this thesis

When considering a magnetic moment in a metallic host, the interaction between the localized moment and the conduction band gives rise to a multitude of interesting physical phenomena. Therefore, the study and characterization of the states at the moment sites plays a central role in the understanding of these systems. The symmetry and degeneracy of the ground-state is influenced by the crystal-field, so that the knowledge of the crystal-field states is of great importance. Other interesting aspects may be the valence and magnetic properties of the impurity, and how these are affected by the environment.

In this thesis, the aspects mentioned above are investigated by means of x-ray spectroscopies. The experimental and theoretical techniques utilized in this work are described in Chapter 2. The two compounds under investigation are the following.

- **$CeCu_2Si_2$** The first unconventional superconductor to be discovered, it is a prototypical example of heavy-fermion compound, where Ce Kondo lattice interacts with the conduction electrons. Chapter 3 is dedicated to the examination of the crystal-field ground-state wave-function of $CeCu_2Si_2$.

- **YFe_2Al_{10}** Y does not belong to the lanthanide series and $4f$ electrons are absent in the unit cell. The Fe atoms, surrounded by an Al host, are the protagonists of the physics and the focus of analysis. Their magnetic properties, valence and degree of correlation are investigated in Chapter 4.

Chapter 2

Experimental techniques

X-ray spectroscopy is used for the investigation of the electronic structure of molecules, liquids and solids. Especially core-level spectroscopy, as a local probe, has been very successful in determining the valence and orbital character of d or f elements in solids. When light is shone on a sample, photons can be scattered, absorbed or annihilated via the photo-electric effect. The last two processes are the basis of x-ray absorption spectroscopy (XAS) and photo-electron spectroscopy (PES) respectively. These are the techniques utilized in this thesis and are the focus of the present chapter.

2.0.1 Synchrotron radiation

XAS experiments, as well as PES ones, require very brilliant light in the x-ray regime. Such a requirement is met by modern synchrotrons.

The term synchrotron radiation refers to the electromagnetic radiation emitted by charged particles moving at relativistic speed on a circular orbit. Modern synchrotrons usually make use of electrons. In general, any charged particle, when moving on a non-linear trajectory, emits light. However, the radiation emitted by a charged particle moving at low speed ($v << c$) resembles that of a classical dipole, whereas a charged particle travelling at very high speed ($v \approx c$), as is the case for electrons in a synchrotron, emits light in a narrow cone tangentially to its orbit. This is pictorially illustrated in Fig. 2.1 .
Besides the peculiar emission divergence, synchrotron light is characterized by many further impressive aspects. A broad range of energies is available, ranging from the infrared to hard x-rays and a photon flux of up to 10^{19} photons per second can be reached, compared to the 10^{10} per second of a common laboratory x-ray lamp.

Fig. 2.2 shows what a modern synchrotron looks like. Electrons are created by an electron gun and then fed into a linear accelerator, which accelerates them to energies of several MeV. They then enter the booster ring, where they are accelerated to energies of the order of the GeV, before entering the storage ring. In both these rings the electrons are kept in a circular orbit by bending magnets. Radio-frequency cavities along the storage ring make up for energy losses of the electrons. The broad spectrum of radiation generated during the bending of the electrons' trajectory is guided towards the beamlines, where the beam is optimized by monochromators, focusing mirrors, slits or other optical devices before reaching the end-stations, where the sample is located. In third generation synchrotrons, other so-called insertion devices are used to improve the intensity and brightness of the beam. These are collocated in the linear sections of the storage ring and are made of a periodic structure of magnets. In a wiggler, magnets with alternating polarities are placed to form a multipole magnet. Upon going through

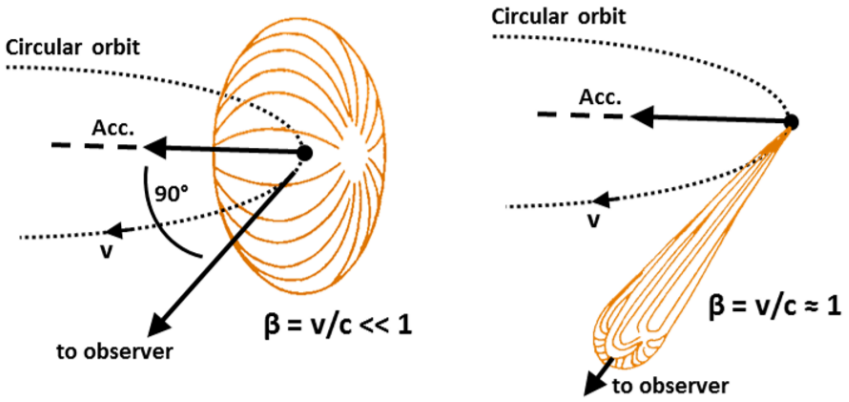

Figure 2.1: *Qualitative depiction of radiation emitted by a charged particle travelling on a circular orbit at low speed (left) and at relativistic speed (right). Figure taken from [4]*

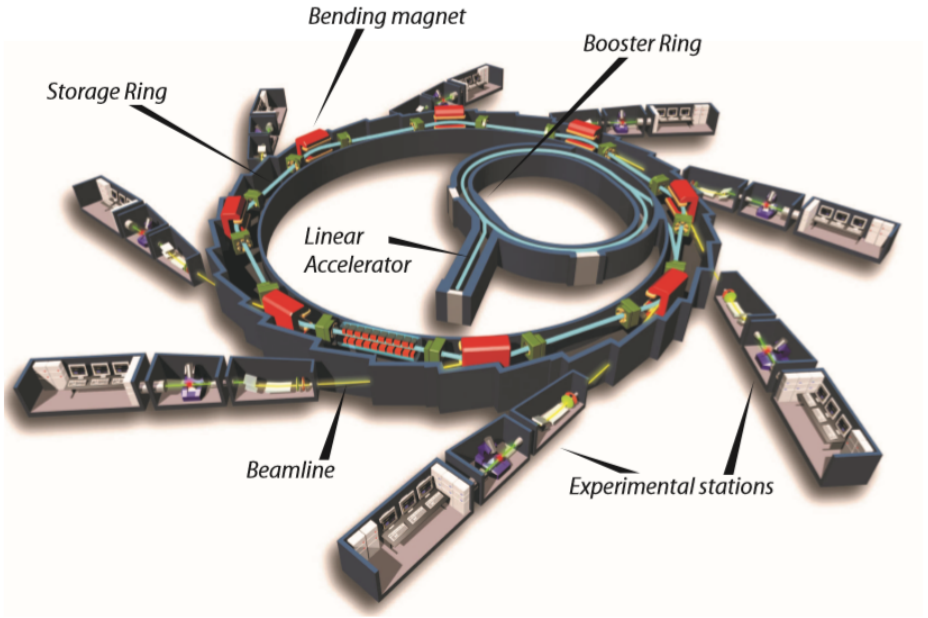

Figure 2.2: *Layout of a modern synchrotron. Figure taken from [5]*

the device, the electrons wiggle in an oscillatory trajectory in the plane of the orbit, and such additional bends intensify the radiation. The more common undulators rely on the same mechanism, but smaller wiggling angles are used, so to exploit interference effects in order to get a very intense and monochromatic beam. The undulators may also allow to produce linearly and circularly polarized light at the same time.

2.1 X-ray absorption spectroscopy

2.1.1 Theoretical background

An absorption experiment consists in irradiating a sample and measuring the amount of radiation absorbed by it. In x-ray absorption spectroscopy, one excites a deeply bound core electron into an unoccupied valence state by means of a photon. The energy of the photon is tuned to an absorption edge, that is to the binding energy of a core level, so that a steep intensity minimum can be registered when the process occurs. On top of that, the fact that synchrotron radiation is used guarantees very high spectral intensities. Since the binding energies depend on how strongly the electrons are bound to the nucleus, or in other words to the number of protons in it, XAS is an element-specific technique. In the nomenclature used in XAS to label the peaks in the spectra the principal quantum number of the photo-excited electron is replaced by the letters K, L, M, ..., and the orbital quantum number is expressed starting from the energetically lowest core-hole sub-shell by numbers (1,2,3,...). So, for example, the excitations from the spin-orbit split $2p_{\frac{3}{2},\frac{1}{2}}$ sub-shells into the $3d$ shell are labelled $L_{2,3}$, the excitations from the spin-orbit split $3d_{\frac{5}{2},\frac{3}{2}}$ sub-shells into the $4f$ shell are called $M_{4,5}$. In the case of rare-earths, the $M_{4,5}$ absorption edge, located between 800 eV and 1700 eV, is of particular interest.

Let us concentrate on the theoretical description of the absorption process and spectrum, following Ref. [38]. The Hamiltonian for an atomic system interacting with radiation reads:

$$H = H_{rad} + H_{atom} + H_{int} \tag{2.1}$$

H_{atom} is the atomic Hamiltonian, comprising the electrons-nucleus, spin-orbit, electron-electron interactions and the crystal-field. H_{rad} is the radiation Hamiltonian:

$$H_{rad} = \sum_{\boldsymbol{k}\lambda} \hbar\omega_{\boldsymbol{k}} \left(n_{\boldsymbol{k}\lambda} + \frac{1}{2} \right) \tag{2.2}$$

where $\mathbf{k}$ is the wave-vector and λ the polarization. The interaction Hamiltonian H_{int} can be approximated in perturbation theory and its first term, neglecting the spin, can be written as:

$$H_{int}^{(1)} = \frac{e}{mc} \sum_i \boldsymbol{p}_i \cdot \boldsymbol{A}(\boldsymbol{r}_i) \tag{2.3}$$

Here $\boldsymbol{A}$ is the vector potential, $\boldsymbol{p}_i$ are the electrons momenta. H_int[1] describes resonant processes like x-ray absorption. The probability W_{fi} of a transition between two states induced by the absorption of a photon with energy $\hbar\omega$ is given by Fermi's golden rule:

$$W_{fi} = \frac{2\pi}{\hbar} \left| \langle \psi_f | \hat{T} | \psi_i \rangle \right|^2 \delta(E_f - E_i - \hbar\omega) \tag{2.4}$$

Here ψ_f and ψ_i are the final and initial states, respectively, and $\hat{T}$ is the transition operator. The full derivation is reported in Ref. [38]. Only the first order term of H_{int} is considered, since we are dealing with a resonant process. Here we only underline that the transition operator can be written in the following way:

$$\hat{T} = e^{i\frac{\omega}{c}\hat{\boldsymbol{n}}\cdot\boldsymbol{r}} \hat{\boldsymbol{e}} \cdot \boldsymbol{p} \tag{2.5}$$

Here $\hat{\boldsymbol{e}}$ and $\hat{\boldsymbol{n}}$ are the light polarization and propagation vectors, $\boldsymbol{r}$ and $\boldsymbol{p}$ describe the position and momentum of the excited electron. The exponential factor in Eq. 2.5 can be expanded in a power series. Since the wavelength of the radiation is considered to

be much larger than the spatial extension of the electron orbital scale in the soft x-rays regime only the first-order term is relevant. This is the dipole approximation. The transition operator can then be written as:

$$\hat{T} \approx \boldsymbol{p} \cdot \hat{\boldsymbol{e}} \equiv \hat{D} \tag{2.6}$$

The spectral intensity I of an absorption experiment is proportional to the transition probability:

$$I \propto \sum_f |\langle \psi_f | \, \boldsymbol{p} \cdot \hat{\boldsymbol{e}} \, | \psi_i \rangle|^2 \delta(E_f - E_i - \hbar\omega) \tag{2.7}$$

Throughout this Chapter we will refer explicitly to the $M_{4,5}$ edge of rare-earth compounds, and in particular the absorption process of a Ce^{3+} ion in a tetragonal environment, of which data are presented in Chapter 3. For a rare-earth system the $M_{4,5}$ absorption edge is given by the transition between a $|\psi_i\rangle = \left|3d^{10}4f^n\right\rangle$ and a $|\psi_f\rangle = \left|3d^9 4f^{n+1}\right\rangle$ state. In the case of Ce^{3+} we have $n = 1$. The final state configuration $\left|3d^9 4f^2\right\rangle$ consists of $10 \cdot 14 \cdot 13/2 = 910$ different states. Which of these states are accessible in the absorption process is determined by dipole selection rules. These and the interpretation of XAS spectra are the topic of the following section.

2.1.2 XAS spectra

As an example, let us consider the absorption spectrum of $CeCu_2Si_2$ (Fig. 2.3). It is useful to consider the selection rules governing the absorption process and the physical interaction leading to the multiplet structure in Fig. 2.3, in order to gain a better understanding of the features present in a spectrum.

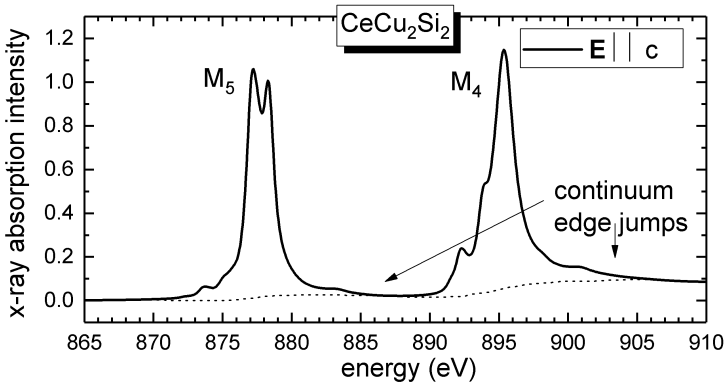

Figure 2.3: *XAS spectrum of $CeCu_2Si_2$ at 250 mK acquired with the electric field vector $\boldsymbol{E} \parallel c$, being c the tetragonal axis with four-fold rotational symmetry. The spectrum is characterized by the presence of the M_5 and M_4 absorption edges, each made up by a multiplet structure. Continuum edge jumps occur right after the main absorption edges, symbolized by the dashed line.*

Selection rules

The spectral intensity is proportional to $\left|\langle \psi_f | \, \hat{D} \, | \psi_i \rangle\right|^2$, where $\hat{D}$ is the dipole transition operator. The integral $\langle \psi_f | \, \hat{D} \, | \psi_i \rangle$ is non-vanishing only if the integrand is even: since

the dipole transition operator $\hat{T}$ is odd, transitions are allowed only if the final state has different parity compared to the initial state. The dipole selection rules follow from these symmetry considerations and the conservation of spin and angular momentum. The selection rules are:

$$\begin{aligned}
&\Delta l = \pm 1;\\
&\Delta j = 0, \pm 1;\\
&\Delta m_l = 0, \pm 1;\\
&\Delta m_s = 0;\\
&\Delta L = 0, \pm 1;\\
&\Delta S = 0;\\
&\Delta J = 0, \pm 1
\end{aligned}$$

where l is the orbital, m_j the magnetic, m_s the spin and j the total angular momentum quantum numbers of the electron, while capital letters refer to the atom.

Multiplets

The spectrum in Fig 2.3 has two main features: the large splitting between the M_5 and M_4 edge and the multiplet structure within each edge.

The former is due to the large spin-orbit coupling of the $3d$ core hole in the final state. In an XAS experiment at the Ce 3^+ $M_{4,5}$ edge, the initial state is the crystal-field ground-state of the $3d^{10}4f^1$ configuration when measuring at low enough temperatures so that only the ground-state is populated. A photon with energy ≈ 900 eV is shone on the sample and an electron is excited from the $3d$ subshell to the $4f$ subshell, leaving a $3d$ core hole behind. The hole can be in the $3d_{\frac{3}{2}}$ sub-shell, lower in energy and producing the M_5 edge, or in the $3d_{\frac{5}{2}}$ sub-shell, higher in energy and producing the M_4 edge, i.e. we have two possibilities: the $3d^4_{\frac{3}{2}}3d^6_{\frac{5}{2}}4f^1 \rightarrow 3d^4_{\frac{3}{2}}3d^5_{\frac{5}{2}}4f^2$ transition (M_5) and the $3d^4_{\frac{3}{2}}3d^6_{\frac{5}{2}}4f^1 \rightarrow 3d^3_{\frac{3}{2}}3d^6_{\frac{5}{2}}4f^2$ transition (M_4).

The one-electron picture is the simplest approach to describe the spectral features of either edge in Fig 2.3. In this framework, we should expect the XAS spectrum to be made up of two peaks, relative to the $3d_{\frac{3}{2}}$ and $3d_{\frac{5}{2}}$ sub-shells. Moreover, the ratio of the integrated intensities of the M_4 and M_5 edges should be $\frac{6}{4}$, because the $3d_{\frac{3}{2}}$ state is 4-fold, whereas the $3d_{\frac{5}{2}}$ is 6-fold degenerate. In reality, the spectrum is characterized by a complex multiplet structure (see again 2.3), since in correlated materials electron-electron and electron-hole interactions are far from being negligible. The electron-hole pair in the final state, in particular, is a strongly interacting system and is known as an *exciton*. A comparison between the simulation with and without interactions is reported in Fig 2.4. The importance of electron-electron and electron-hole interactions is evident there. The one-electron approach usually works for K edges ($1s$ to $2p$), but for transitions into the d or f shell ($L_{2,3}$ edges of transition metals and $M_{4,5}$ edges of rare-earths) the great overlap of the core and valence wave-functions in the excitonic final state hinders the single particle approach: the system can only be understood as a many-body wave-function. Excitons are highly bound and localized, meaning that they give rise to a sharp and distinct multiplet structure. A schematic representation of the absorption process at the Ce $M_{4,5}$ edge is depicted in Fig. 2.5.

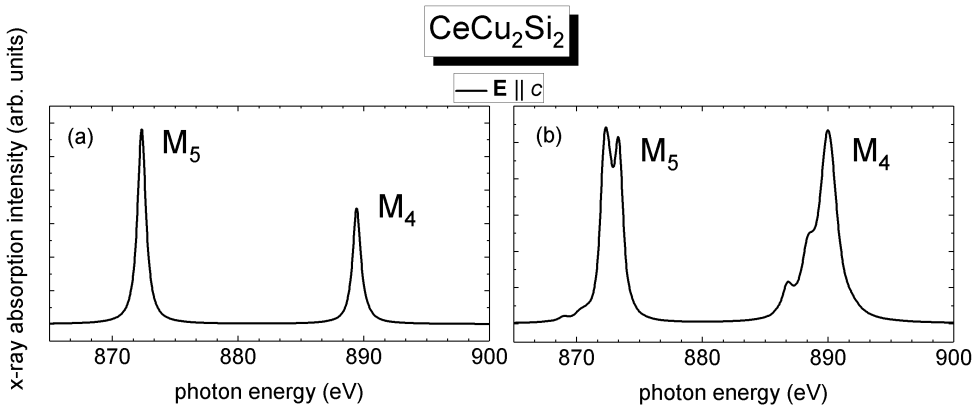

Figure 2.4: *Simulation of the XAS spectrum of $CeCu_2Si_2$ for light polarized parallel to the c tetragonal axis (a) without accounting for electron-electron and electron-hole interactions and (b) with the full interactions considered.*

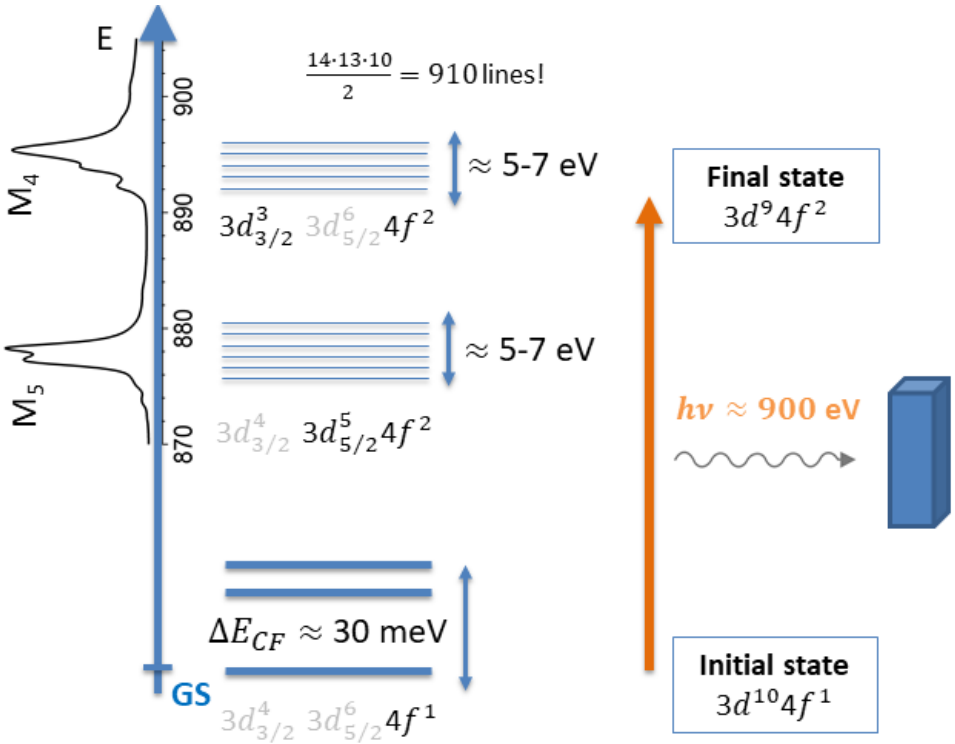

Figure 2.5: *Schematic representation of the absorption process at the $M_{4,5}$ Ce^{3+} edge. The initial state is the crystal-field ground-state. A photon excites an electron from the 3d subshell into the 4f subshell. The final state multiplet structure is made up by two sub-structures. They are set apart by the spin-orbit interaction on the 3d core-hole and give rise to the M_5 and M_4 edges.*

Finally, the background of the experimental spectrum (see arrows in Fig. 2.3) is due to non-bound final states. It shows as continuum edge jumps right after the M_4 and M_5 edges.

The multiplet structure visible in a XAS spectrum can provide a lot of information about the valence state, since different valence states yield different multiplet structures and energy positions of the peaks. Besides, sensitivity toward orbital occupation, spin state and crystal-field ground and excited states can also be achieved by considering the polarization dependence of absorption, as explained in the next section.

Polarization dependence

The dipole operator $\hat{D}$ governing the absorption process can be decomposed into its three cartesian components and written as $\hat{D} = \hat{D_x} + \hat{D_y} + \hat{D_z}$, with each component referring to the polarization direction of light.

The so-called isotropic spectrum can be obtained either by summing up spectra measured with different polarization on a single crystal or by performing a measurement on a powder sample. The use of linear or circular polarized light on a single crystal can provide useful information. In general, *linear dichroism* (LD), probed with linear polarized light, provides information about the orbital occupation, whereas *x-ray magnetic circular dichroism* (XMCD), measured with circular polarized light, provides knowledge about the spin and orbital moments [39, 40, 41, 42, 43, 44, 45, 46, 47, 48].

X-ray linear dichroism (XLD) and the determination of the crystal-field ground-state

In 2008 Hansmann *et.al* [49] showed for $CePd_2Si_2$ that low temperature linear polarized XAS is an effective probe for the $4f$ charge distribution of the ground-state, that is for the crystal-field ground-state wave-function. The core hole created in the absorption process has a typical lifetime of 1 fs, meaning that the lifetime broadening of the final states is around 0.5 eV. This is much larger than the splitting between these states. The experimental resolution is typically around 0.5 eV as well. Because of such large broadening, XAS is not able to resolve the splittings of the final states. and it may seem that the access to crystal-field information, and thus to the ground-state, is hindered. However, it is the use of linear polarized light and its dipole selection rules that allows to effectively probe the ground-state and its symmetry in particular.

Let us look at the matrix element $\langle \psi_f | \hat{D} | \psi_i \rangle$. It depends on the polarization, contained in the dipole operator, and on the initial state, i.e. the ground-state wave-function. These two dependencies directly affect the shape of the spectra. Let us consider a pure $J_z = \frac{5}{2}$ ground-state. If light is shone on the sample with polarization parallel and perpendicular to the c tetragonal axis, the two acquired spectra are different: $I_{\boldsymbol{E}\parallel c}$ and $I_{\boldsymbol{E}\perp c}$. If the ground-state is now a $J_z = \frac{3}{2}$ instead the two recorded spectra will be different compared to those of the $J_z = \frac{5}{2}$. The same holds for the remaining pure $J_z = \frac{1}{2}$. The absorption process for different pure J_z ground-states is schematically shown in Fig. 2.6 (a) and the corresponding simulated spectra in Fig. 2.6 (b). The linear dichroism is defined as the difference of two spectra measured with different linear polarization: $LD = I_{\boldsymbol{E}\parallel c} - I_{\boldsymbol{E}\perp c}$. The bottom part of Fig. 2.6 (b) shows the simulated LD of pure J_z states: it is clear that each state has its characteristic LD so that, by looking at it, we are effectively probing the ground-state wave-function symmetry.

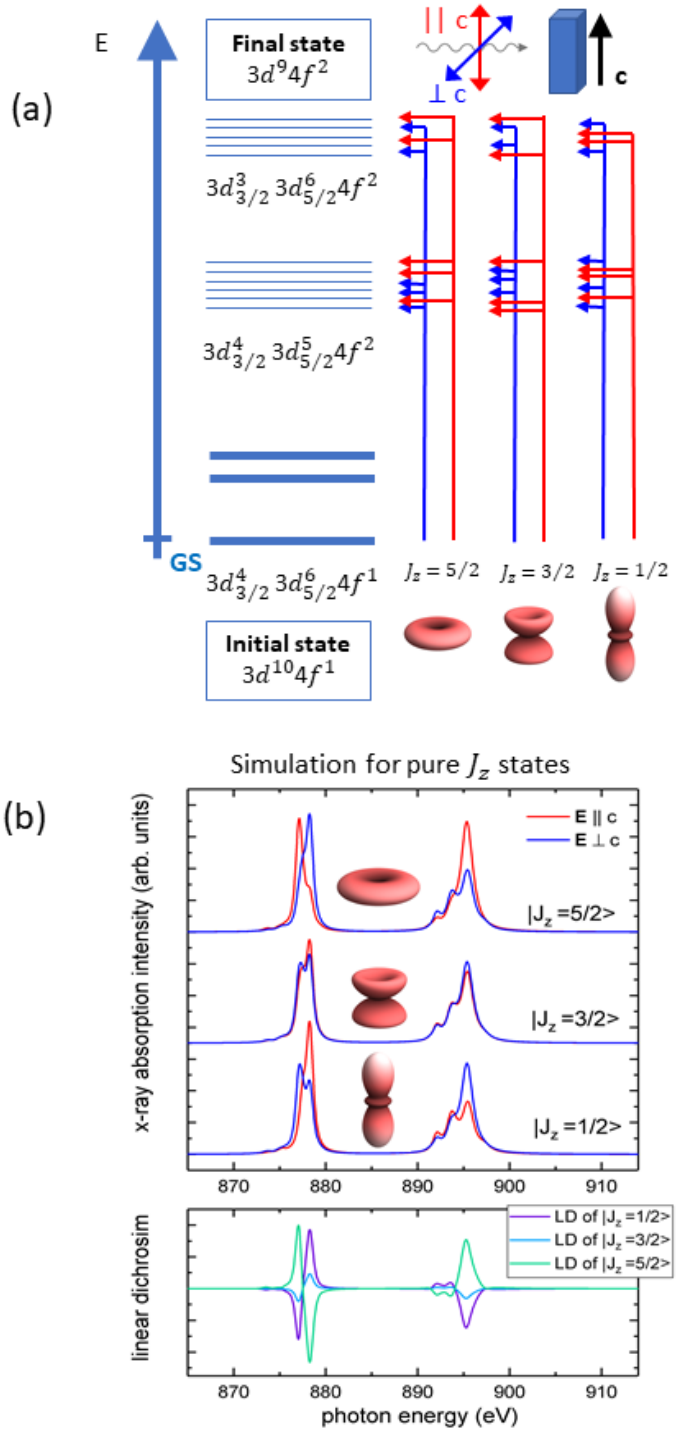

Figure 2.6: *(a) Schematic representation of the absorption process from pure J_z ground-states with light polarized in two directions, parallel (red) and pependicular (blue) to the c tetragonal axis.(b) Simulation of the polarized XAS spectra for pure J_z ground-states (top) and corresponding LDs (bottom).*

The Γ_7 states are given by an admixture of the pure $J_z = \frac{5}{2}$ and $J_z = \frac{3}{2}$ of the Hund's rule $J = \frac{5}{2}$ ground-state multiplet, according to:

$$\Gamma_7^{\pm} = \alpha \left| \pm\frac{5}{2} \right\rangle \pm \sqrt{1-\alpha^2} \left| \mp\frac{3}{2} \right\rangle \tag{2.8}$$

The top part of Fig. 2.7 shows the linear polarized XAS simulation for a $\Gamma_7^{\pm}$ ground-state. By varying the mixing parameter α, the J_z admixture in the ground-state changes. Since each pure J_z state has its own LD, the overall LD of the $\Gamma_7^{\pm}$ changes as well, as shown in the bottom part of Fig. 2.7.

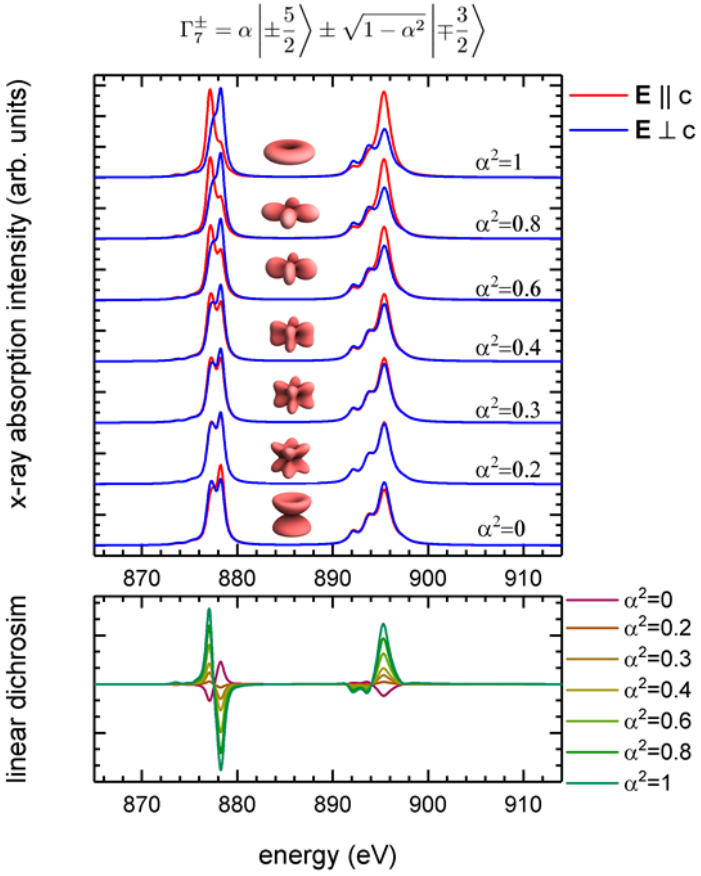

Figure 2.7: *(top) Simulated linear polarization dependent XAS spectra of the Ce^{3+} $M_{4,5}$ edge for different α^2 values of the $\Gamma_7^{\pm}$ ground-states wave function and (bottom) corresponding dichorism. Spectra are simulated with light parallel (red) and perpendicular to c (blue). The insets also show the corresponding charge density.*

On the whole, linear polarized XAS can effectively probe the crystal-field ground-state symmetry in rare-earths, without being impaired by the large lifetime broadening of the states and by the experimental resolution. It should be noted that this is rigorously true only if the temperature is low enough, so that only the ground-state is populated. If the temperature rises, then excited crystal-field states are populated as well, resulting in an LD given by a Boltzmann weighted sum of the LD of the single states. This can also be exploited as a way to shed light into excited crystal-field states.

A drawback of polarized XAS is the impossibility to resolve rotational symmetries

higher than two-fold symmetries. The infeasibility stems from the fact that such processes are governed by dipole excitations. This is why the + and the − sign cannot be determined although the two signs refer to two orbitals that are rotated by 45◦ one with respect to the other. If one wanted to determine the orientation of the ground-state wave function, one should then resort to techniques relying on higher multipole excitations, such as non-resonant inelastic x-ray scattering (NIXS). From a mathematical point of view, dipole-limited techniques are sensitive only to $|\alpha|$ or equivalently α^2, but not to its sign. In other words, linear polarized XAS is only sensitive to the relative J_z admixture in the ground state (given by $|\alpha|$).

X-ray magnetic circular dichrosim (XMCD) and spin state of the system

The absorption excitations are spin-sensitive if the experiment is performed with right and left circular polarized light. If the system possesses a net magnetic moment (due to magnetic order or an applied magnetic field) along the direction of the Poynting vector, then the XMCD, defined as the difference of two spectra measured with different circular polarization, contains information about the magnetic state. On the one hand, one can simulate the spectra and get the information by fitting the experimental data. However, useful sum rules were derived. The first sum rule, derived by Thole *et al.* [46], relates the integrated spectral intensity to the expectation value of the z-component of the angular momentum $< L_z >$. If we consider the $L_{2,3}$ edge it reads:

$$< L_z >= \frac{2l(l+1)(4l+2-n)}{c(c+1)-l(l+1)-2} \frac{\int_{L_2+L_3}(\mu^+ - \mu^-)dE}{\int_{L_2+L_3}(\mu^+ + \mu^- + \mu^0)dE} \tag{2.9}$$

where l is the orbital quantum number of the valence state, c is the orbital quantum number of the core state, n is the number of electrons in the valence state, $\mu^+(\mu^-)$ is the XAS spectrum for left (right) polarized light, μ^0 is the XAS spectrum for linearly polarized light, without polarization parallel to the quantization axis. The integrals are extended over the whole L_2 + L_3 edges energy range. Carra *et al.* [47] later derived a sum rule to obtain the z-component of the spin $< S_z >$ and intra-atomic magnetic dipole moment $< T_z >$:

$$c_1(n) < S_z > + c_2(n) < T_z >= \frac{\int_{L_3}(\mu^+ - \mu^-)dE - \frac{c+1}{c}\int_{L_2}(\mu^+ - \mu^-)dE}{\int_{L_3+L_2}(\mu^+ + \mu^- + \mu^0)dE} \tag{2.10}$$

where:

$$c_1(n) = \frac{l(l+1)-2-c(c+1)}{3c(4l+2-n)}$$

$$c_2(n) = \frac{l(l+1)[l(l+1)+2c(c+1)+4]-3(c-1)^2(c+2)^2}{6lc(l+1)(4l+2-n)}$$

An example of application of sum rules to the Fe $L_{2,3}$ edge is reported in Appendix **??**.

It is important to underline that XMCD, unlike common magnetization measurements, is element specific, since the photon energy is tuned to the absorption edge of the element under investigation.

2.1.3 Detection modes

An absorption experiment aims at measuring the change of the intensity before the sample $I_0(\nu)$ and after the sample $I_0(\nu, d)$, where d is the thickness of the sample. The absorption coefficient $\mu(\nu)$ is recovered from the law:

$$I(\nu, d) = I_0(\nu)e^{-\mu(\nu)d} \tag{2.11}$$

This particular way of performing absorption is known as *transmission mode*, it is bulk sensitive and works well for extremely thin samples ($<<$ 1 μm) or hard x-rays ($\hbar\omega \geq 3$ keV). Due to the practical difficulties of having such thin samples, this method is not common in the soft x-ray regime.

The absorption cross-section can also be measured in an indirect way with the so-called yield modes. Indeed, the absorption process causes the formation of a core hole, which is then bound to decay. This may happen through emission of fluorescence or secondary electrons of lower binding energy. The crucial assumption is that the absorption cross-section is proportional to the number of core holes and that the decay processes can be also linked to the number of core holes [38]. The *fluorescence yield mode* measures the photons emitted from the sample as a result of the fluorescent recombination of the excited electrons with the core holes. Typically the total fluorescence yield (TFY) method is used, where the measured signal is taken by summing over a broad range of photon energies. The typical penetration depth of soft x-rays is of the order of 100 nm, meaning that the technique is bulk sensitive. However, due to self absorption effects, the spectra can be distorted. In the *total electron yield mode* (TEY), on the other hand, the sample is grounded and its drain current is measured. As a matter of fact, after absorption, an excited electron can decay into the core hole leaving the energy difference between its original energy and the energy of the core hole to another electron, which is emitted via the Auger effect. This electron may not directly escape from the sample but scatter inelastically with other electrons and trigger a cascade of secondary electrons. An amount of electrons then leaves the sample, which is grounded. in order to re-establish charge neutrality, electrons from ground come into the sample and are measured as a drain current: this can be relatively large (10^{-10} A). The sensitivity of this method is around 4 to 20 nm although the mean free path of the electrons first emitted is much smaller. The short escape depth of the primary Auger electrons may be seen as a limit; however, saturation effects can be neglected because of the large difference between the x-ray penetration and the electron escape depth [50]. The TEY mode was used for the measurements reported in this thesis.

2.1.4 Atomic full multiplet theory and single-ion calculations

In order to simulate an XAS spectrum one should compute the intensity as in Eq. 2.7. A precise knowledge of the eigenstates of the system is then needed to compute the transition matrix elements $\left|\langle\psi_f|\,\hat{D}\,|\psi_i\rangle\right|$. Atomic full-multiplet theory, based either on crystal-field or ligand-field theory, aims at identifying a suitable Hamiltonian to describe the system, taking into account the electron-electron and electron-hole interactions in full. This is crucial in order to capture the correct spectral features of materials with correlated electrons. Both crystal-field theory and ligand-field theory concentrate on a single ion surrounded by its neighbours, a structure known as a *cluster*, but neglect the full translational symmetry of the crystal. The highly localized nature of the final excitonic state of the absorption process makes this assumption reliable. However, while crystal-field theory is a purely electrostatic model where these neighbours are thought of as point charges acting on the outer shell of the central ion, ligand-field theory also considers covalency with the neighbours.

In a full-multiplet calculation one builds an adequate Hamiltonian on a many-electron basis starting from single-electron wave functions. The dimension of the basis depends on the configuration we are considering. If we assume these single-electron wave-functions to be atomic-like, then they can be written as a product of an angular and radial part

$\psi(r,\theta,\phi) = R_n^l(r)Y_l^m(\theta,\phi)$, where the quantum numbers follow the usual convention. The correctly anti-symmetrized many-electron wave-function $\psi(r_1,...,r_N)$ can then be constructed from a Slater determinant of one-electron wave-functions:

$$\psi(r_1,...,r_N) = \begin{vmatrix} \psi_1(r_1) & \cdots & \psi_1(r_N) \\ \vdots & \ddots & \vdots \\ \psi_N(r_1) & \cdots & \psi_N(r_N) \end{vmatrix} \tag{2.12}$$

The Hamiltonian that we have to define to solve the for the eigenstates in the initial and final configurations of the absorption process should contain the terms in the following list. A more detailed presentation of the matter can be found in Ref. [51].

- The crystal-field potential, whose parametrization is described in Chapter 1.
- The spin-orbit interaction, described in first quantization by the term:

$$H_{SO} = \sum_{j=1}^{N_e} \zeta(r_j)\boldsymbol{l_j}\cdot\boldsymbol{s_j} \tag{2.13}$$

  where N_e is the number of electrons in the shell under consideration, ζ are the spin-orbit coupling constants, $\boldsymbol{l_j}$ and $\boldsymbol{l_j}$ are the angular momentum and spin.
- The electron-electron and electron-hole Coulomb interaction, central to reproduce the multiplet structure in materials with correlated electrons. It is described by the scattering between the two two-electron states $|ij\rangle$ and $|i'j'\rangle$ via the potential:

$$H_C(\boldsymbol{r_i},\boldsymbol{r_j}) = \frac{e^2}{|\boldsymbol{r_i}-\boldsymbol{r_j}|} \tag{2.14}$$

  As in the case of the crystal-field potential in Chapter 1, this potential can also be expanded in spherical harmonics as well, thus factorizing into an angular and into a radial part. The angular term is made up of integrals of spherical harmonics, which can be solved analytically. The radial part consists of the so-called Slater integrals:

$$R^k(iji'j') = e^2\int_0^\infty\int_0^\infty \frac{r_<^k}{r_>^{k+1}} R_i(r_i)R_j(r_j)R_j(r_i)R_i(r_j)r_i^2r_j^2dr_idr_j \tag{2.15}$$

  where k refers to the multipole order of the interaction. The integrals are not analytically solvable, but are numerically calculated and tabulated.
- A magnetic field term, in case a magnetic field is also present, written as:

$$H_{magn.} = \boldsymbol{B}\cdot(\boldsymbol{L}+2\boldsymbol{S}) \tag{2.16}$$

- Covalency, stemming from the hopping of electrons between the central ion and the surrounding ligands, not treated any longer as mere point charges acting on the outer shell of the central ion. This is the central further step of ligand-field theory with respect to crystal-field theory. Since the $4f$ electrons are so well localized, hopping is not a prominent feature in that case. All calculations done in this work were performed in the purely ionic picture of crystal-field theory. Nevertheless, one may resort to consider covalency to identify from which specific valence state of the Ce ion the further peaks not expected by ionic calculations were coming from. The

addition of covalency mimics the presence of different valences due to hybridization in the Kondo regime. To appreciate this one could look at Fig. 2.3 and 2.4 (b): the main absorption edges due to the $3d^{10}4f^1 \rightarrow 3d^9 4f^2$ transition are well reproduced by the simulation. However, the little satellites right after the main absorption lines of the M_4 and M_5 edges are not predicted by the calculation: by including covalency, one could tell that these features are due to the $3d^{10}4f^0 \rightarrow 3d^9 4f^1$ transition.

Once the Hamiltonian has been set up, both for the initial and final states, it can be diagonalized to calculate its eigenstates and eigenenergies. The spectrum is then calculated as explained at the beginning of this paragraph. As a final step, the calculated spectrum needs to be convoluted with a Gaussian and Lorentzian functions to account for the experimental resolution and lifetime broadening respectively.

All calculations in this thesis were performed with the code *Quanty* by M. Haverkort [52]. The atomic values for the spin-orbit coupling constants and the Slater integrals were taken from Cowan's code [37], based on the Hartree-Fock approximation. However, the values are not usually accurate for ions in a solid, particularly as far as Slater intergrals are concerned. This is mainly due to the fact that the presence of other charges in a solid partially screens the electron-electron and electron-hole interactions. Therefore, the atomic Slater integrals have to be reduced to account for this effect.

2.1.5 Simulation and fitting of linear polarized XAS spectra

In Chapter 3 full-multiplet calculations are used to simulate the Ce $M_{4,5}$ edge XAS spectra of $CeCu_2Si_2$. The simulation is based on a purely ionic crystal-field model: Ce only has a pure f^1 configuration (3^+ valence).

Let us consider the list of interactions listed above in the Ce^{3+} case we are condsidering here. For the initial state configuration $3d^{10}4f^1$ the Hamiltonian contains the crystal-field (A_2^0, A_4^0 and A_4^4 parameters) and the spin-orbit interaction of the f electron ($\zeta_{4f}^{initial}$). For the final state configuration $3d^9 4f^2$ the Hamiltonian contains the crystal-field (which we assume to be equal to that of the initial state), the spin-orbit interaction of the f electrons (ζ_{4f}^{final}) and of the d core hole (ζ_{3d}^{final}), the f-f electron-electron and f-d electron-hole interactions.

The aim of Chapter 3 is to obtain information about the crystal-field ground-state of $CeCu_2Si_2$. In order to do so, it is crucial to find the A_2^0, A_4^0 and A_4^4 parameters by fitting calculated spectra to experimental ones.

Reduction of the Slater integrals

Firstly, all interactions in the Hamiltonian other than the crystal-field need to be known. In particular, we have to determine the reduction factors for the atomic Slater integrals. This is done by fitting the experimental isotropic spectrum to the simulated one. We recall that tetragonal symmetry is characterized by two equivalent a and b crystallographic axes and a longer c axis. The isotropic spectrum is then defined, in general, as $I_{iso} = \frac{2I_{\mathbf{E}\perp c}+I_{\mathbf{E}\parallel c}}{3}$, where $I_{\mathbf{E}\perp c}$ and $I_{\mathbf{E}\parallel c}$ are the intensities for the polarization perpendicular and parallel to the c axis. The optimization of the Slater integrals is done on the isotropic spectrum since it does not show polarization dependence: the ground-state symmetry only influences the LD. Figure 2.8 shows the simulated isotropic spectrum for different pure J_z ground-states and they indeed look nearly identical.

Moreover, the isotropic spectrum is not influenced by the crystal-field. Figure 2.9 compares two simulations: the isotropic spectrum obtained from a $\Gamma_7^{\pm}$ ground-state and the isotropic spectrum obtained by removing the crystal-field in the simulation and

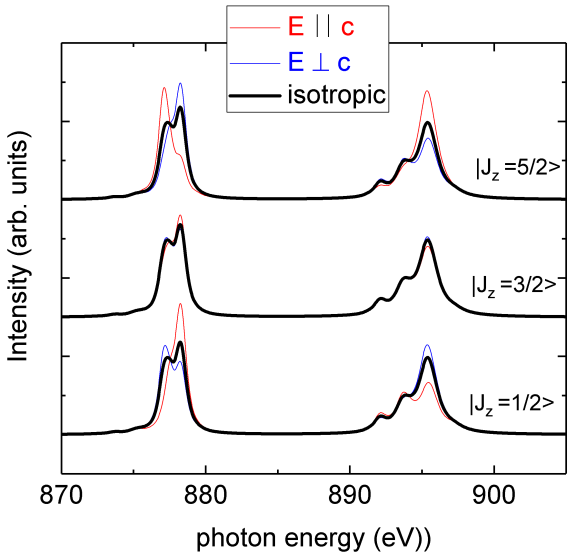

Figure 2.8: *Simulated isotropic spectra for pure J_z ground-states. Spectra for light polarized parallel and perpendicular to c are shown in red and blue respectively. The isotropic spectra are calculated as* $I_{iso} = \frac{2I_{E\perp c}+I_{E\parallel c}}{3}$.

summing the spectra for the pure J_z states of the lower $J = \frac{5}{2}$ multiplet. It can be seen that they look identical. A variation of, for example, 10% of the Slater integrals reductions would entail a much bigger effect on the spectrum instead.

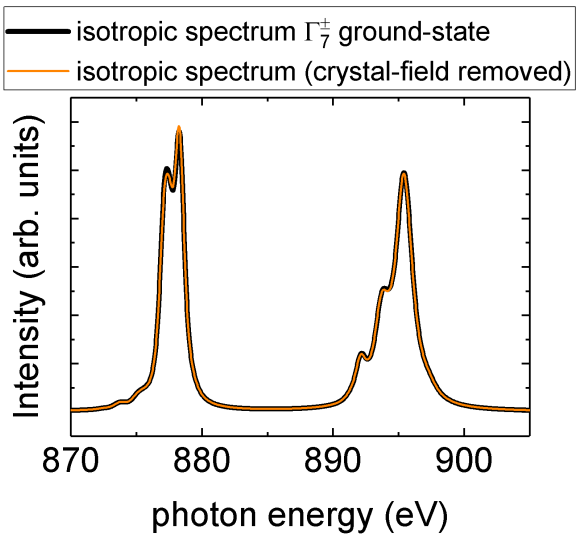

Figure 2.9: *Simulated isotropic spectrum obtained for a* $\Gamma_7^{\pm}$ *ground-state as* $I_{iso} = \frac{2I_{E\perp c}+I_{E\parallel c}}{3}$ *(black) and simulated isotropic spectrum obtained by removing the crystal-field from the simulation (orange).*

The crystal-field is unknown at the beginning of the fitting procedure. Hence, the simulated isotropic spectrum is practically obtained as in the orange curve of Fig. 2.9, by removing the crystal-field in the simulation and summing the spectra for the pure J_z

states of the of the lower $J = \frac{5}{2}$ multiplet. Since the crystal-field does not influence the isotropic spectrum, the optimized Slater integrals will also be good when the crystal-field is added to the simulation. The fit is mainly done on the M_5 edge. The reason is that the continuum edge jump is not included in the simulations and it is smaller right after the M_5 edge compared to the M_4 edge.

Determination of the mixing-parameter

From this point onwards the fit of the simulation to the experiment is mainly done looking at the LD, rather than at the spectra themselves, since the subtraction performed to obtain the dichroism eliminates continuum edge jumps and the parts of the spectra not included in the simulation (such as the spectral weight coming to the $4f^0$ contribution which, having $J = 0$ and being spherically symmetric, shows no dichroism). If the ground-state is a Γ_7 the knowledge of the mixing parameter α is needed to characterize it. This is not the case for a Γ_6 state, which is essentially a pure-state. Whether the ground-state is one or the other can be determined from the exhibited dichorism, as explained in section 2.1.2.

If the ground-state is a Γ_7 state, it is crucial to determine the adequate mixing parameter α in order to fit the spectrum. We still do not consider the complications of including the crystal-field in the simulation and construct the simulated spectrum as an incoherent superposition of pure $J_z = \pm\frac{5}{2}$ and $J_z = \mp\frac{3}{2}$ states. In this sense the spectrum is given by:

$$I = \alpha^2 I_{J_z=\pm\frac{5}{2}} + \beta^2 I_{J_z=\mp\frac{3}{2}} \tag{2.17}$$

The best fit gives the value of α.

Let us understand why this is a legitimate approach. As explained in Section 1.4.3, for a $4f^1$ system in a small tetragonal crystal-field (the influence of the $J = \frac{7}{2}$ multiplet can be neglected), the Γ_7 ground-state is given by:

$$\alpha \left| J = \frac{5}{2}, J_z = \pm\frac{5}{2} \right\rangle + \beta \left| J = \frac{5}{2}, J_z = \mp\frac{3}{2} \right\rangle \tag{2.18}$$

The XAS spectrum is proportional to $\sum_f |\langle\psi_f| D |\psi_i\rangle|^2$, where in our present case ψ_i is the ground-state wave-function. The intensity can then be written as:

$$I = \alpha^2 I_{J_z=\pm\frac{5}{2}} + \beta^2 I_{J_z=\mp\frac{3}{2}} + 2\alpha\beta I_{int} \tag{2.19}$$

where $I_{J_z=\pm\frac{5}{2}}$ is the spectrum of the pure $J_z = \frac{5}{2}$ state, $I_{J_z=\mp\frac{3}{2}}$ that of the pure $J_z = \frac{3}{2}$ state and I_{int} is an "intereference" term, given by

$$I_{int} = M_{\frac{5}{2},\frac{3}{2}} \tag{2.20}$$

where

$$M_{j,j'} \propto \sum_f \langle\psi_f| D |\psi_j\rangle \langle\psi_f| D |\psi_{j'}\rangle \delta(E_i + h\nu - E_f) \tag{2.21}$$

The interference term is then non-zero only if both matrix elements in 2.21 are non-zero, i.e. if there are final states that can be reached by both ground-state components $J_z = \frac{5}{2}$ and $J_z = \frac{3}{2}$. Let us consider our $4f^1$ system in D_{4h} tetragonal crystal-field and the dipole selection rules:

$$\Delta J = 0, \pm 1; \tag{2.22}$$

$$\Delta J_z = 0 \; for \; z - polarized \; light$$

$$\Delta J_z = \pm 1 \; for \; x(y) - polarized \; light$$

If we assume the crystal-field to be absent in the final state, so that the final state is made up of pure $\left|J = \frac{5}{2}, J_z\right\rangle$ states, we can write down the following table, relating the initial state components to the possible final states according to the selection rules mentioned above.

Initial state component	$\left\|J = \frac{5}{2}, J_z = +\frac{5}{2}\right\rangle$	$\left\|J = \frac{5}{2}, J_z = -\frac{3}{2}\right\rangle$	
final state via $\Delta J_z = 0$ and $\Delta J_z = 0$	$\left\langle J = \frac{5}{2}, J_z = +\frac{5}{2}\right\|$ $\left\langle J = \frac{3}{2}, J_z = +\frac{5}{2}\right\|$ $\left\langle J = \frac{7}{2}, J_z = +\frac{5}{2}\right\|$	$\left\langle J = \frac{5}{2}, J_z = -\frac{3}{2}\right\|$ $\left\langle J = \frac{3}{2}, J_z = -\frac{3}{2}\right\|$ $\left\langle J = \frac{7}{2}, J_z = -\frac{3}{2}\right\|$	no matches
final state via $\Delta J_z = \pm 1$ and $\Delta J_z = \pm 1$	$\left\langle J = \frac{5}{2}, J_z = +\frac{3}{2}\right\|$ $\left\langle J = \frac{7}{2}, J_z = +\frac{3}{2}\right\|$ $\left\langle J = \frac{3}{2}, J_z = +\frac{3}{2}\right\|$ $\left\langle J = \frac{7}{2}, J_z = +\frac{7}{2}\right\|$	$\left\langle J = \frac{5}{2}, J_z = -\frac{5}{2}\right\|$ $\left\langle J = \frac{7}{2}, J_z = -\frac{5}{2}\right\|$ $\left\langle J = \frac{3}{2}, J_z = -\frac{1}{2}\right\|$ $\left\langle J = \frac{5}{2}, J_z = -\frac{1}{2}\right\|$ $\left\langle J = \frac{7}{2}, J_z = -\frac{1}{2}\right\|$	no matches

It can be seen that no combination of J, J_z yields a final state accessible from both ground-state components.

Therefore, the XAS spectrum can indeed be described as an incoherent superposition of pure J_z states as in equation 2.17. This holds true as long as the crystal-field in the final state is neglected. If this is not the case the pure $|J, J_z\rangle$ are mixed in the final states. For example, if we consider $\Gamma_7^{\pm}$ final state (mixing of the $\left|J = \frac{5}{2}, J_z = +\frac{5}{2}\right\rangle$ and $\left|J = \frac{5}{2}, J_z = -\frac{3}{2}\right\rangle$ pure states, as in the first line of the table above) via $\Delta J_z = 0$ and $\Delta J_z = 0$, then the final state is accessible from both ground-state components. In any case, the interference term arising from the presence of the crystal-field in the final state is very small and the incoherent sum approximation may still be used. Figure 2.10 shows the comparison between a $\Gamma_7^{\pm}$ ground-state spectrum simulated with crystal-field included in both initial and final states and one where the spectrum is built as an incoherent superposition of J_z states. The differences are neglgible.

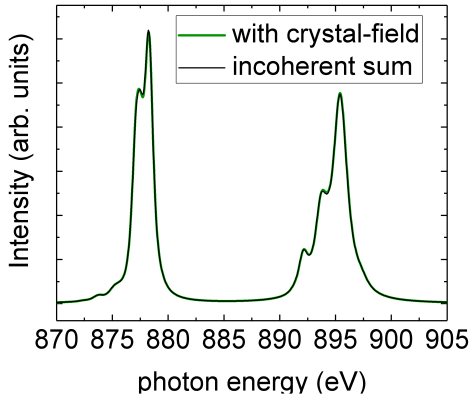

Figure 2.10: $\Gamma_7^{\pm}$ *ground-state spectrum simulated with crystal-field included in both initial and final states (green) and one where the spectrum is built as an incoherent superposition of* J_z *states (red).*

Using the crystal-field Hamiltonian

Once the mixing parameter has been determined, the crystal-field is finally added to the simulation. Its parameterization is achieved by specifying the crystal-field splittings ΔE_{21} and ΔE_{31}, since we already know α. This is totally equivalent to the set of parameters A_2^0, A_4^0 and A_4^4.

If temperature effects are taken into account, the crystal-field excited-states should be populated according to thermal statistics. In polarized XAS the excited crystal-field states contribute only indirectly via thermal occupation. The simulated spectrum is then obtained by summing up the spectra of the excited-states, in addition to that of the ground-state, and weighing them according to their Boltzmann factor $e^{-\frac{\Delta E}{k_B T}}$. Here ΔE is the energy difference between a given excited state and the ground-state. The crystal-field scheme is then influencing the spectrum as these splittings are varied. A correct determination of the splittings should be able to fit the experimental spectrum at different temperatures.

One should also consider that thermal population is not the only effect modifying the spectrum (and dichroism). In addition the hybridization to the conduction electrons, which in the pure crystal-field picture is not included in the simulations, will alter the spectra. Hybridization may lead to the presence of some excited crystal-field state character into the ground-state and this clearly influences the dichroism. Still sticking to a crystal-field picture, one could consider such effects by simply constructing the simulated dichroism as a linear combination of the dichorism calculated for the ground-state and for the excited-states, summed up with given weights. In the case of a Γ_7^+/Γ_7^- mixing, for example, the dichroism can be expressed in terms of a weight a as:

$$aLD_{\Gamma_7^-} + (1-a)LD_{\Gamma_7^+} \tag{2.23}$$

If one expresses the LD of the states as an incoherent sum of pure J_z states the last expression can be written as:

$$a[\alpha^2 LD_{\frac{5}{2}} + (1-\alpha^2)LD_{\frac{3}{2}}] + (1-a)[(1-\alpha^2)LD_{\frac{5}{2}} + \alpha^2 LD_{\frac{3}{2}}] \tag{2.24}$$

2.1.6 DEIMOS beamline in synchrotron SOLEIL

In this section we will briefly describe the layout of a XAS beamline, referring in particular to the DEIMOS beamline in synchrotron SOLEIL (Saint-Aubin, France). A detailed description of the beamline can be found in Ref. [6]. The beamline is dedicated to polarized XAS measurements in the soft x-rays regime. The scheme of the DEIMOS beamline is reported in Fig. 2.11.

The DEIMOS straight section before the beamline is equipped with two undulators. An Apple-II HU-52 undulator with 52.4 mm period allows to reach all linear (horizontal to vertical) and circular polarizations from 350 eV to 2500 eV. A variable diaphragm is located at 13.09 m from the middle of the straight section and allows to select the useful part of the polarized light, first or higher harmonics. A second EMPHU-65 undulator supplements the HU-52 undulator by enhancing sensitivity. The use of an electromagnet to generate the vertical magnetic field allows to switch rapidly (5 Hz repetition rate) from right to left circular polarization.

The first optical chamber, still located in the radiation protected hutch, allows to choose between two optical paths: M1a-M1b or M1a-M1c in Fig. 2.11, by translating in and out of the beam the M1b mirror. The mirrors M1b and M1c differ in their coatings, platinum and rhodium, respectively. The M1a-M1b path is optimized for high energy harmonics rejection below 1300 eV due to a working angle of 2.53°, whereas M1a-M1c is used for higher energies with a working angle of 1.20°. M1a is a flat mirror, while

M1b and M1c are toroidal. The horizontal deflecting toroidal mirror (M1b or M1c) focuses the light in the horizontal plane to a point located 200 mm after the M3 mirror (inside the monochromator chamber) while in the vertical direction light is collimated in an almost parallel beam. The power coming to the first optical chamber (maximum of 160 W on an angular acceptance of 0.2×0.2 mrad^2) is dissipated using a water cooled mirror.

The monochromator is equipped with two plane gratings, Gra and Grb (Gr in Fig. 2.11), which are respectively a variable groove depth grating with 1600 lines/mm, and a Mo_2C/B_4C alternate multilayer grating with 2400 lines/mm. The first grating is optimized for the energy range 240–1500 eV while the second grating is optimized for the energy domain 1000–2500 eV. The dispersed light is vertically deflected onto the M2 plane mirror and then deviated in the horizontal plane by a cylinder mirror M3 which focuses the beam on the exit slit.
The refocussing chamber contains a spherical mirror M4 and a toroidal mirror M5 (Wolter mirror combination). The two successive reflections in the horizontal plane are used to cancel the coma aberration in this plane. Two toroidal mirrors (M5a and M5b) are available and can be switched under vacuum in order to produce two different beam sizes in the end-station located 3 m downstream. The beam size on the sample is $\approx 80 \times 80$ μm^2 for M5a to $\approx 800 \times 800$ μm^2 for M5b.

Finally the beam comes to the end-station. The end-station consists in a superconducting magnet providing ± 7 T along the x-rays beam or ± 2 T perpendicular to the beam. The magnet is equipped with an inset allowing the cooling of the sample down to 250 mK. Below 1 K, the cooling is achieved by a ^{3}He-^{4}He dilution refrigerator from the company CryoConcept. A pressure of $\approx 10^{-10}$ mbar is present in the sample chamber.

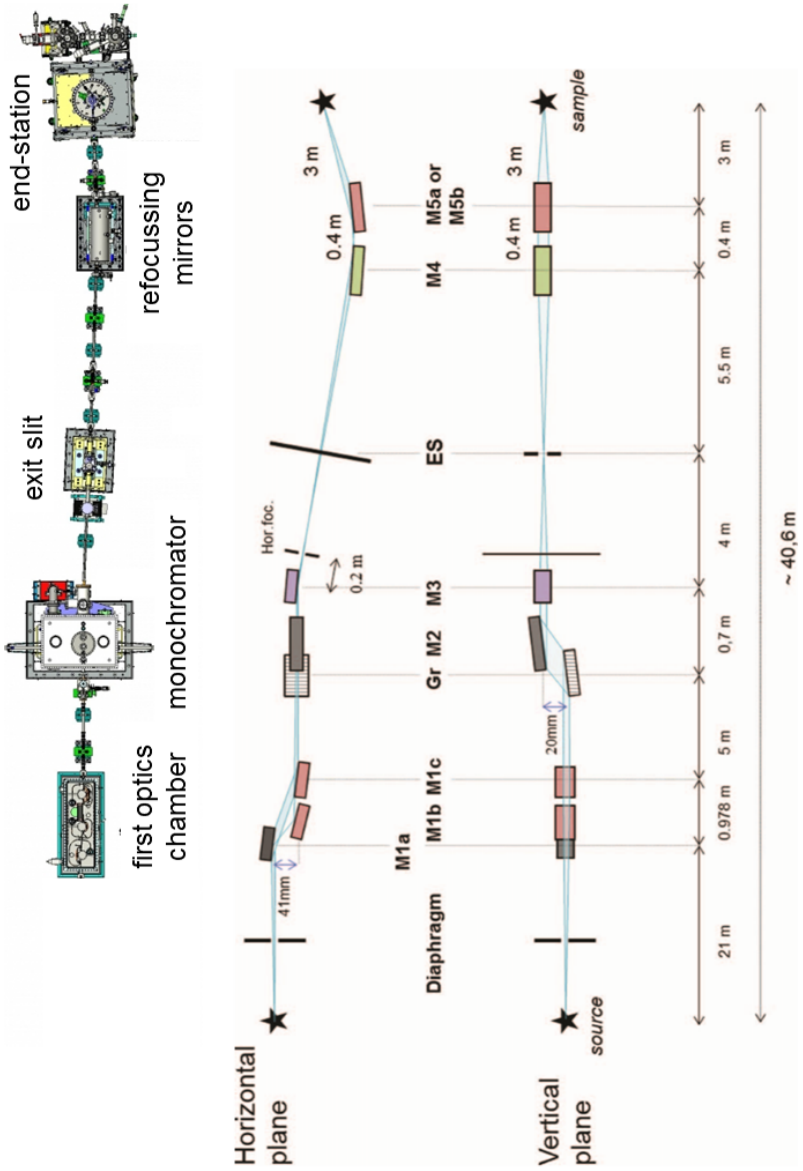

Figure 2.11: *Schematic layout of the DEIMOS beamline in synchrotron SOLEIL (Saint-Aubin, France). Figure adapted from [6] and [7].*

2.2 Photoelectron spectrosocpy

In a photoelectron spectroscopy experiment photons with sufficiently high energy impinge on the sample exciting electrons from occupied energy states into the vacuum via the photoelectric effect. The process involves a transition from an N-particle initial state to an $(N-1)$-particle final state.

2.2.1 Theoretical description

The photon energy $\hbar\omega$ required in a photoemission experiment has to be higher than the binding energy E_b of the electrons in the sample. Only then the excited electrons are able to leave the sample with a certain kinetic energy E_k. Such a quantity is related to the binding energy of the electrons in the sample by famous Einstein's equation, basically stating the conservation of energy in the process:

$$E_k = \hbar\omega - |E_b| - \phi_{sample} \tag{2.25}$$

Here ϕ_{sample} is the work function, that is the potential barrier at the surface that has to be overcome in order for the electrons to escape into vacuum. However, the analyzer which performs the measurement also has its characteristic work function $\phi_{analyzer}$, so that the measured kinetic energy can be written as:

$$E_k = \hbar\omega - |E_b| - \phi_{analyzer} \tag{2.26}$$

Knowing $\phi_{analyzer}$ one can recover E_b from the measurement of E_k and obtain the PES spectrum. The work function of the analyzer is usually determined by measuring the Fermi edge of a gold or silver sample.

A typical PES spectrum is characterized by the presence of some characteristic features.

- Sharp peaks due to the electrons elastically leaving the sample after the excitation. The lineshape is broadened by the finite experimental resolution (Gaussian broadening) and by the limited life-time of the excited states (Lorentzian broadening). Moreover, metallic samples tend to exhibit asymmetric lineshapes, as described by Doniach and Sunjic [53].

- A superimposed background of secondary electrons, due to electrons inelastically scattering and losing energy on their way out of the sample. A procedure to subtract the background was described by Shirley [54].

- Peaks coming from Auger electrons, whereby the decay of an electron into the core hole created in the photoemission process leaves its energy to some other electron, which can then escape from the sample. Since this process is independent of the photon energy, Auger lines always appear at the same kinetic energy.

- Lastly, in metals, plasmons can be excited by the Coulomb interaction between conduction electrons and a photoelectron, during its journey to the sample surface. The photoelectron excites plasmons losing a characteristic energy $\Delta E_{plasmon} = \hbar\omega_{plasmon}$, leading to the appearance of plasmon peaks at binding energy intervals of $N\Delta E_{plasmon}$ (N is an integer) above the main elastic peak.

A complete and satisfactory theoretical description of the photoemeission process can be found in Ref. [38]. For the scope of this thesis, however, a single-particle approach based on Eq. 2.26 is sufficient. An illustration is given in Fig. 2.12. The PES spectrum can be thought as a representation of the occupied density of states of the sample.

Nonethelss, one should keep in mind that such an approach cannot be trustworthy when dealing with strongly correlated systems. If one considers a magnetic material with partially filled d or f shells, for example, the strong coupling between the electrons in these shells and the core hole leads to characteristic multiplet structures which are not predicted by the one-electron picture and satellites due to different valences, similarly to XAS.

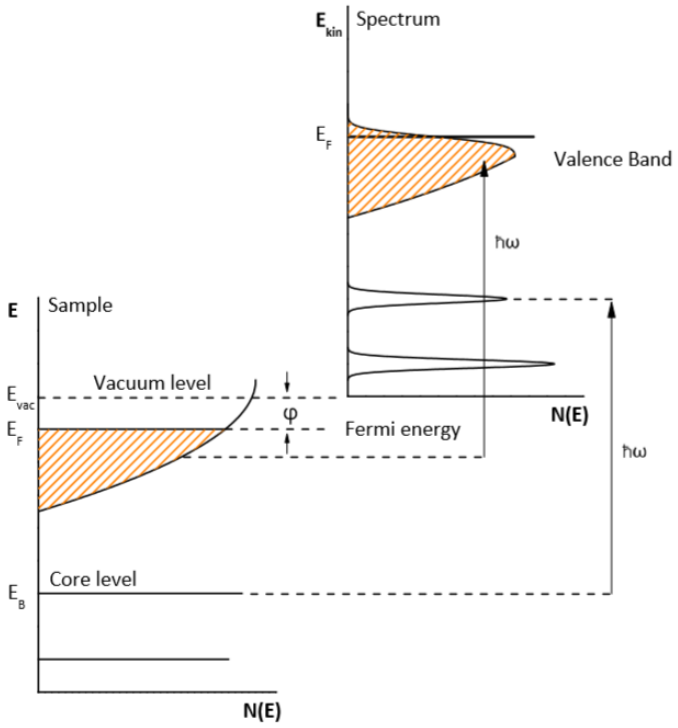

Figure 2.12: *One-electron interpretation of the relation between the PES spectrum as a function of the photoelectrons kinetic energy and the density of states of the sample. Figure adapted from [4].*

2.2.2 Experimental aspects and setup

The energy of the incoming photons can belong to the ultraviolet regime (UPS, 5-100 eV), to the soft x-ray range (XPS, 100-2000 eV) or to the hard x-ray domain (HAXPES, >2000 eV). UPS probes valence state with great resolution and surface sensitivity whereas XPS and HAXPES are better suited for core-levels and have higher bulk sensitivity. In this thesis radiation in the soft x-ray domain was used to perform PES.

The outcoming electrons are analyzed according to their kinetic energy E_k or their momentum p. Here we distinguish two modes. In *transmission mode* the electrons are sorted out according to their kinetic energy, whereas in *angle-resolved mode* also the direction of emission is considered. We just focus on what is used in this thesis, that is transmission mode.

PES is a versatile technique and can provide a lot of information on the sample. To mention a few aspects, the chemical composition can be recovered from the core level peaks positions and their intensities since every element has its specific set of binding

energies and photo-ionization cross-sections. Valence changes can be detected as shifts or as multiple peaks. In angular-resolved PES it is possible to reconstruct the dispersion $E(\boldsymbol{k})$ of the electrons bands from the energy and momentum distributions.

Photoionization cross-sections

The probability of emission of an electron from a certain electronic (sub-)shell upon absorption of a photon is given by the photoionization cross-sections, tabulated in [17, 18]. There exists a strong dependence on the (sub-)shell considered and on the photon energy. As a consequence, spectra recorded at different photon energies may show different features due to different cross-sections.

The analyzer

The electron analyzer is made up by a system of electron lenses and of the analyzer itself, where the electrons are sorted with respect to their kinetic energy. The analyzer is made up by two concentric hemispheres, in between which a deflecting electrostatic field is set and builds up the so-called pass energy, that is the center of the narrow energy window acceptance of the incoming electrons. The electron lenses focus the electrons onto the analyzer's entrance slit and accelerate/decelerate them from their kinetic energy to the pass energy. Once the electrons enter the analyzer, they are guided through the hemisphere by the static field and follow different trajectories according to their kinetic energies. Upon exiting the analyzer, they hit the detector in different spots. Just before the detector, micro-channel plates amplify the signal. The setup is schematically represented in Fig. 2.13.

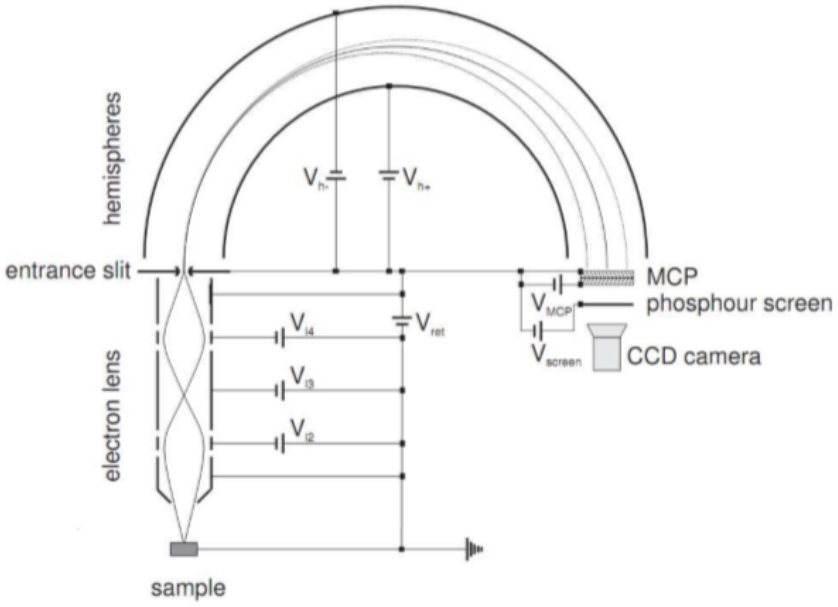

Figure 2.13: *Figure taken from [8]. Schematic representation of a hemispherical PES analyzer.*

Surface sensitivity

The probing depth of PES is limited by the escape depth of the excited photoelectrons. This quantity is claimed to be independent of the elements the electrons have to traverse and is only influenced by the electrons kinetic energy, as illustrated in the *universal curve* [55] in Fig. 2.14.

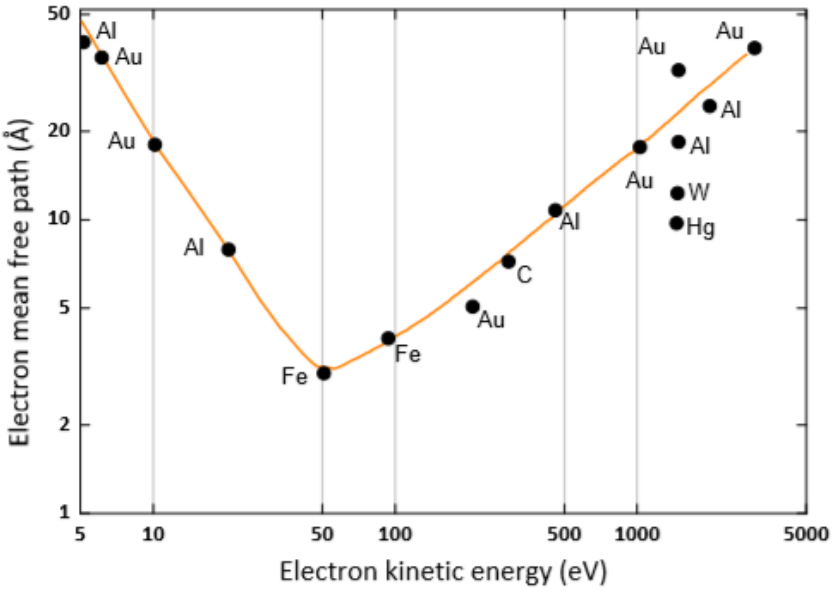

Figure 2.14: *Figure taken from [4]. Universal curve for the inelastic mean free path of electrons as a function of their kinetic energy (orange lines). The dots indicate the values for certain metals.*

The escape depths for usual PES experiments, working in the 15 to 1500 eV energy range, is about 3 to 20 Å, so that the technique is very surface sensitive.

2.3 Sample preparation

Soft x-rays are absorbed by air. Besides, the short mean free path of electron in air would prevent electron from reaching the analyzer in a PES experiment so that the beamline components are typically kept in a vacuum environment ($P \approx 10^{-7}$ mbar).

XAS in the TEY mode and PES experiments are very surface sensitive so that the samples have to be cleaved *in situ* in UHV. The measurement has to be performed in UHV to assure clean sample surfaces and to avoid surface aging while taking data. Ideally the sample chamber has a vacuum of the order of 10^{-10} mbar. The cleaving of the samples in this work was achieved with two alternative methods:

- In the post cleaving method a post is glued on top of the sample. By breaking it off a clean sample surface is recovered.
- In the knife cleaving method the sample is mounted so that it has a flat lateral surface exposed. This surface is then placed against an anvil and a knife, coming from the opposite side with respect to the anvil, cuts the sample leaving a clean surface exposed.

As far as XAS is concerned, since the signal is measured with the total electron yield mode, the sample has to be mounted on the sample holder in such a way that good electrical contact is guaranteed. The sample is then first of all glued to the sample holder with a thin layer of epoxy silver glue (EPO-TEK H21D), which is conductive, applied on the surface of the sample in contact with the holder. Then, to provide the stability necessary to withstand the cleaving process, TorrSeal (Loctite EA 1C) is applied to fix the sample. The cooling of the sample is achieved by cooling the sample rod and a good thermal contact is needed between sample and holder in order for this mechanism to work. The layer of silver glue helps to achieve this as well. Silver glue needs to be cured for 14 minutes at 150 °C, while TorrSeal needs to be cured for two hours at 60 °C or one hour at 80 °C or 20-30 minutes at 120 °C. Fig. 2.15 shows a drawing of a sample mounted for post cleaving for a XAS experiment.

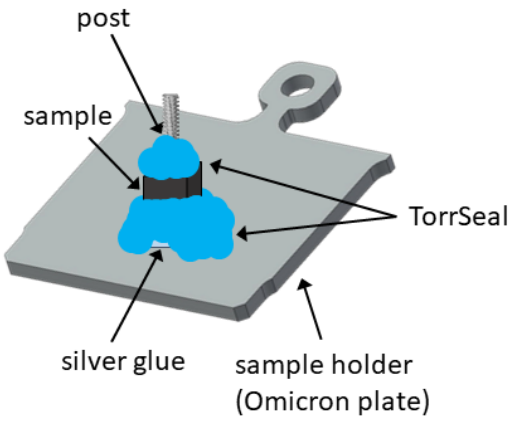

Figure 2.15: *Schematic drawing of a sample mounted for post cleaving for a XAS experiment. The post is attached to the top of the sample: the sample is cleaved by breaking it off. The sample is glued to the sample holder (an Omicron plate in this case) with silver glue and firmly attached to it with TorrSeal.*

In contrast to XAS, where the fact that TorrSeal is insulating can be exploited so that only the drain current coming from the sample is measured, in PES, any charging around the sample would ruin the measurement. As a consequence, in order to mount a sample for photoemission, first a droplet of TorrSeal is applied to the surface of the sample in contact with the sample holder, then the sample is fixed in place by silver-glue, which is conductive. Care must be taken so that the application of silver glue guarantees electrical contact with the sample holder, otherwise the sample will charge up when photoelectrons leave it. Since photoemission is very surface sensitive, particular care is deployed when cleaning the sample. Isopropanol is used to remove any residual dirt left by the aceton used to previously clean the sample, which would disturb the vacuum of the experiment. Fig. 2.16 shows a schematic drawing of a sample mounted for knife-cleaving for a PES experiment.

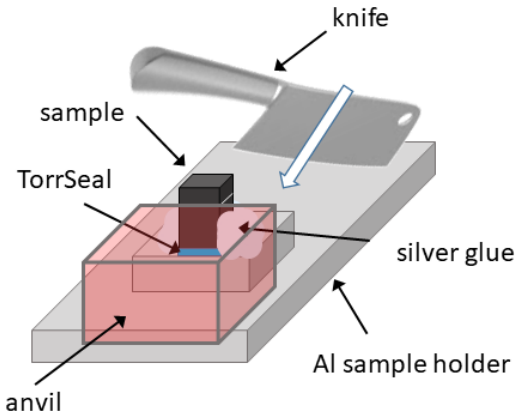

Figure 2.16: *Schematic drawing of a sample mounted for knife cleaving for a PES experiment. The sample is mounted on a podium, with a flat surface right on the edge of the podium: this surface can adhere to an anvil so that the knife can come from the other side and cleave the sample. The sample is glued to the sample holder with TorrSeal and firmly attached to it with silver glue.*

For XAS, in order to correctly probe the sample on specific directions, a precise alignment is crucial. The samples were aligned by the Laue method, which will be now described very briefly. A stationary single crystal is illuminated with a beam of "white" radiation, usually coming from a target metal with high atomic number (e.g. tungsten). Being the sample a single crystal, Bragg's condition for different wavelengths is satisfied by different crystallographic planes, giving rise to a diffraction pattern recorded as a transmission or back-reflection photograph. The Laue pattern indicates the orientation of the crystal in the given direction it sits in front of the Laue camera. By analyzing and fitting the Laue image, one can align the sample along a given crystallographic direction with high precision.

Chapter 3

$CeCu_2Si_2$

The focus of this Chapter is the investigation of the crystal-field ground-state wave function of $CeCu_2Si_2$ by means of linear polarized XAS in the temperature range from 250 mK to 250 K, thus covering the superconducting ($T_c = 0.6$ K) and Kondo transitions ($T_K \approx 10-20$ K). First, a general introduction to the material and the motivation behind the work is given. Then, the results and discussion are presented.

3.1 Introduction

3.1.1 Physical properties of $CeCu_2Si_2$

Unconventional superconductivity was first discovered in $CeCu_2Si_2$ by Steglich *et al.* [12] in 1979, paving the way to a whole new field of research, where superconductivity occurs on the brink of magnetism.

$CeCu_2Si_2$ crystallizes in a tetragonal structure (space group I4/*mmm*, see Fig. 3.1) and is a prototypical heavy-fermion compound.

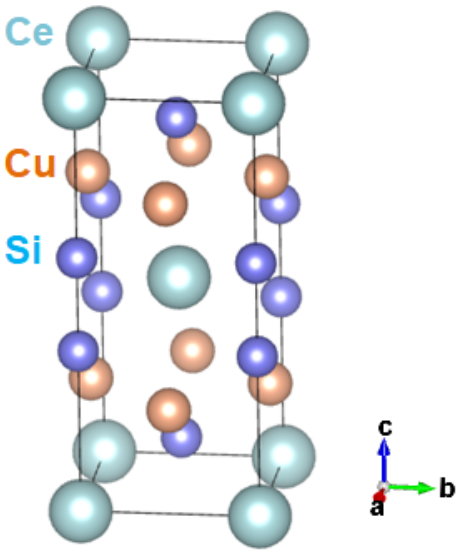

Figure 3.1: *Tetragonal unit cell of $CeCu_2Si_2$.*

The coefficient γ of the low temperature specific heat $C = \gamma T$ is of the order of $1\,\mathrm{Jmol^{-1}K^{-2}}$ [12]. Fig. 3.2 shows the low temperature specific heat of $CeCu_2Si_2$ divided by temperature as a function of temperature, measured in different magnetic fields. The valence of Ce in this compound is close to 3^+, i.e. the f-electron occupation is a bit smaller than 1; it is 0.96 according to Rüff et al. [56]. The single crystalline static susceptibility, shown in Fig. 3.3, shows a strong anisotropy and testifies to the existence of crystal-field effects, as expected in a tetragonal Ce compound with an $f^{n\approx1}$ configuration. The resistivity $\rho(T)$ amounts to (5-10)10^{-7} Ωm at 300 K, which is a typical value for a metal. In $CeCu_2Si_2$, however, in contrast to a metal, $\rho(T)$ rises as the temperature decreases and goes through a maximum at about 10 K, which is symptomatic for a heavy fermion material with a Kondo temperature of 10-20 K. Fig. 3.4 (a) shows the resistivity of $CeCu_2Si_2$ up to 300 K. Fig. 3.4 (b) shows the decrease of the resistivity below 1 K, upon entering the superconducting phase.

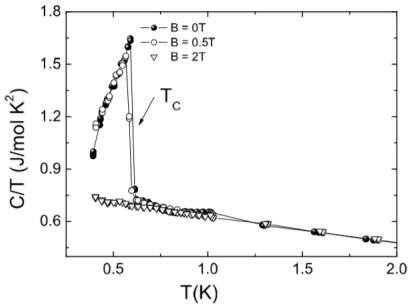

Figure 3.2: *Figure adapted from [9]. Temperature dependence of the specific heat for a $CeCu_2Si_2$ single crystal in different magnetic fields. The critical field is about 2 T. Below this value, a jump of the specific heat is observed at $T_c = 0.6\ K$.*

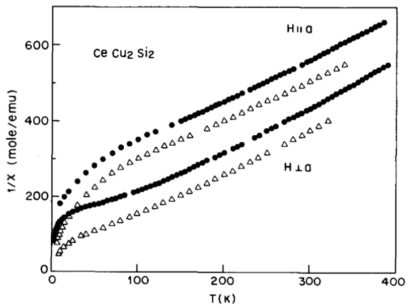

Figure 3.3: *Figure from [10]. Inverse magnetic suseptibility of two $CeCu_2Si_2$ single crystal samples along the two principal crystallographic directions. Circles refer to crystals grown from a Cu solvent, triangle to crystals grown from an In solvent.*

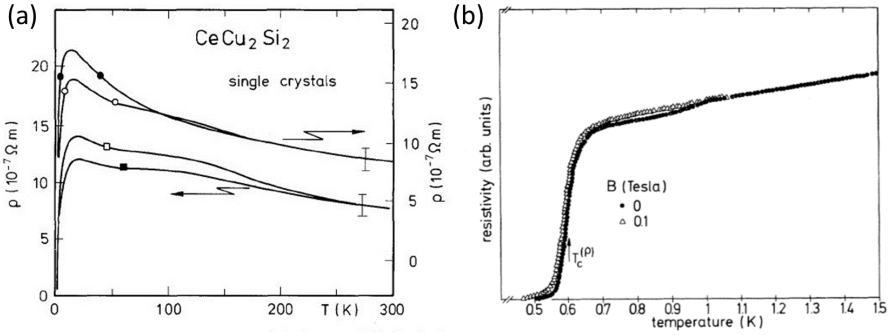

Figure 3.4: *(a) Figure from [11]. Temperature dependence of the resistivity for two $CeCu_2Si_2$ single crystals: one measured without annealing (circles) the other after 4 days of annealing at 1000 °C (squares). Closed (open) symbols refer to current parallel (perpendicular) to the tetragonal c axis. In both case the increase of $\rho(T)$ at low temperature can be seen, followed by its decrease. (b) Figure adapted from [12]. Drop of the resistivity of $CeCu_2Si_2$ below $T_c = 0.6\ K$.*

In 1979 Steglich *et al.* found a superconducnting transition at 0.6 K at ambient pressure, despite the presence of the paramagnetic Ce. It turned out that $CeCu_2Si_2$ is close to a magnetic quantum critical point. Fig. 3.5 reports the phase diagram of $CeCu_2Si_2$ as T against some external parameter g, which can be pressure or the Si stoichiometry for example.

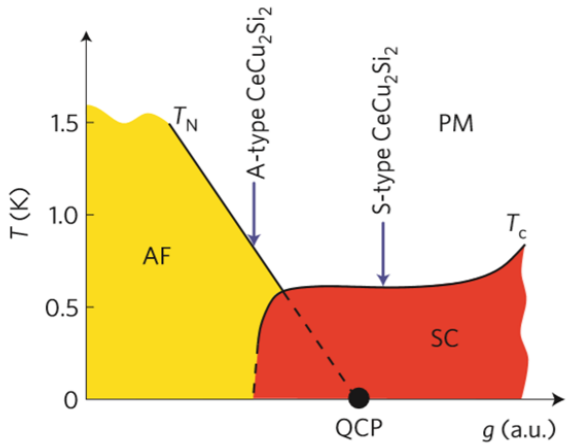

Figure 3.5: *Figure adapted from [13]. Phase diagram of $CeCu_2Si_2$ plotted as T versus some external control parameter, such as the Si stochiometry.*

Very small variations of the Si stoichiometry lead to an antiferromagnetic (A-type sample) or superconducting (S-type sample) ground-state, and in a small region close to the QCP both phases may coexist. Already in 1979 it was clear that superconductivity was unconventional, and there had been increasing consensus that spin fluctuations are the glue for the formation of Cooper pairs [13], whereby the symmetry of the superconducting phase must be *d*-wave [57, 13, 58].

Applying pressure to $CeCu_2Si_2$ shows that there are two superconducting domes in the P-T phase diagram, whose maxima are at $P_{C1} = 0.45$ Gpa, $T_{C1} = 600$ mK and $P_{C2} = 4.5$ Gpa, $T_{C2} = 2$ K. Substitution of Si with Ge leads to a separation of the domes, thus suggesting a different origin of the two superconducting phases, whereas in stoichiometric $CeCu_2Si_2$ and $CeCu_2Ge_2$ the two domes merge into a single, wide superconducting region [27]. Some theories suggest that these are two different superconducting phases, the one close to ambient pressure mediated by spin fluctuations and the one at 4.5 GPa mediated by valence fluctuations. For the latter, however, there is so far no proof [56].

Very recently the nature of the superconducting phase of $CeCu_2Si_2$ at ambient pressure has been contested: still accepting its unconventional nature, some suggest that the symmetry is rather $s++$ or $s--$ instead of *d*-wave [59, 60, 61].

3.1.2 Motivation to study the ground-state wave-function of $CeCu_2Si_2$

Some groups have brought forward ideas about the formation of the superconducting phase where the hybridization of $4f$ and conduction electrons has an impact on the ground-state wave function of Ce in $CeCu_2Si_2$, so that one or the other scenario becomes more or less favorable. For example, Qimiao Si from Rice University, USA and F. Steglich from Max Planck Insitute for Chemical Physics of Solids in Dresden [*private communication, unpublished*] propose a model where a hybridization induced intermixing of the Γ_6 state into the Γ_7 ground-state would support the *d*-wave scenario. Another

group (Pourovskii *et. al* [14]) investigated the electronic structure of $CeCu_2Si_2$ by means of local density approximation (LDA) plus dynamical mean-field theory (DMFT), as a function of pressure and temperature. Upon considering hybridization, which due to the different spatial orientation is stronger for the Γ_7^- than for the Γ_7^+, a strong P-T dependence of the occupation of the crystal-field states appears, as shown in Fig. 3.6.

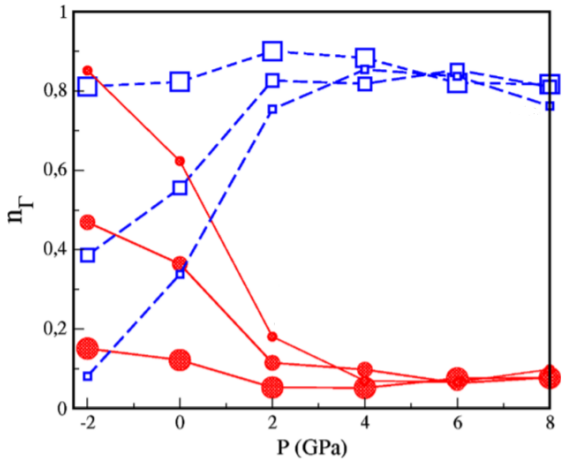

Figure 3.6: *Occupancies $n_{\Gamma_7^+}$ (red circles) and $n_{\Gamma_7^-}$ (blue squares). The large, medium and small symbols refer to 58, 14 and 7 K respectively. Figure adapted from [14].*

It can be noticed that:

- at ambient pressure a reoccupation occurs from about 60% of Γ_7^+ and 40% of Γ_7^- at 7 K to 20% of Γ_7^+ and 80% of Γ_7^- at 58 K.
- Above 4 GPa, the occupaton of the Γ_7^+ is about 80% for all temperatures.

Overall then, the Γ_7^+ is mostly occupied, apart from low temperature and pressure, where the Γ_7^- dominates.

On the whole, this was the motivation for us to measure the ground state wave function of $CeCu_2Si_2$ through the superconducting transition and through the Kondo regime in order to obtain results with high accuracy. XAS has been the method of choice since it allows to detect small changes as function of temperature.

3.1.3 What is known about the crystal-field in $CeCu_2Si_2$?

The Ce atoms in $CeCu_2Si_2$ sit in a tetragonal crystalline environment (point group D_{4h} for the Ce sites). The resulting tetragonal crystal-field splits the Hund's rule ground state of Ce^{3+} with $J = \frac{5}{2}$ into three Kramer's doublets (for more details see Section 1.4.3). The crystal-field scheme and Hamiltonian are fully determined by the two crystal-field transition energies and the mixing parameter α. The three Kramers doublets can be written as:

$$\Gamma_7^+ = \sqrt{1-\alpha^2}\left|\pm\frac{5}{2}\right\rangle + \alpha\left|\mp\frac{3}{2}\right\rangle \tag{3.1}$$
$$\Gamma_6 = \left|\pm\frac{1}{2}\right\rangle$$
$$\Gamma_7^- = \alpha\left|\pm\frac{5}{2}\right\rangle - \sqrt{1-\alpha^2}\left|\mp\frac{3}{2}\right\rangle$$

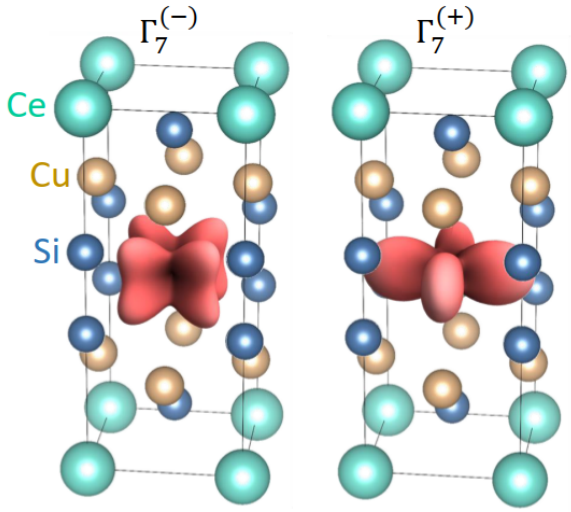

Figure 3.7: *Unit cell $CeCu_2Si_2$ with the Ce Γ_7^- (lobes pointing in the [110] direction, on the left) and Γ_7^+ orbitals (lobes pointing [100] direction, on the right) at the body center of the unit cell. Besides the different orientation, the two orbitals also have a different shape because of the different amounts of $J_z = \left|\pm\frac{5}{2}\right\rangle$ and $J_z = \left|\mp\frac{3}{2}\right\rangle$ in the wave-function (see Eq. 3.1). In the figure, the value $\alpha = 0.58$ is used for the mixing parameter, as will be clarified in section 3.3.1.*

Fig. 3.7 shows the unit cell of $CeCu_2Si_2$ where at a Ce site the Γ_7^- and Γ_7^+ orbitals are plotted.

The crystal-field transition energies have been determined by inelastic neutron scattering by Goremychkin *et al.* [62] on polycrystalline samples. Inelastic neutron scattering is the ideal tool to determine the level splittings, but the combination of phonon scattering and broad magnetic excitations in the same energy window prevents the unambiguous determination of the magnetic intensities. Two strongly broadened and almost degenerate crystal-field excitations were found at about 30 meV in $CeCu_2Si_2$ disproving previous neutron scattering results that found a magnetic transition at about 12 meV [63]. Therefore, still in Ref. [62], the ground-state wave function was determined with single crystal susceptibility measurements and the crystal-field parameters which reproduce the susceptibility yield $|\alpha| = 0.88$ and a Γ_7^+ or Γ_7^- ground-state. The sign $+$ or $-$ cannot be determined in inelastic neutron scattering because the technique is dipole limited. By means of directional dependent non-resonant inealstic x-ray scattering (NIXS), which overcomes the dipole limitations, Willers *et.al* established a Γ_7^- ground-state at 20 K [64]. However, the degree of J_z admixture in the Kondo regime, i.e. the value of $|\alpha|$, was not determined there.

3.2 Experiment and analysis

The method of choice for the measurement of the crystal-field ground-state wave-function was XAS at the rare earth $M_{4,5}$ edge ($3d^{10}4f^1 \rightarrow 3d^9 4f^2$ transition), in particular the LD. As explained in detail in Sec 2.1.2, the LD can effectively probe the ground-state symmetry when working at low temperatures and is very sensitive to small changes.

Two effects can modify the LD of the ground-state, namely hybridization to the conduction electrons, and contribution from excited crystal-field states according to their thermal population. In case of hybridization we may either see a reduction of LD due to some contribution of the f^0 configuration and/or due to a hybridization induced intermixing of excited crystal-field states into the ground-state. The latter can be understood in terms of an effective temperature $T_{eff} = T + T_K$, T_K being the Kondo temperature. The latter effect can lead to a reduction or enhancement of the LD depending on which state mixes into the crystal-field ground state. A hybridization induced reduction of LD has been observed, for example, in $CeRu_4Sn_6$ [65] and $CeCoIn_5$ [66]. Disetangling thermal population and hybridization effects may be tricky, but for $CeCu_2Si_2$ the crystal-field splittings ($\approx$ 30 meV) are much larger than T_K ($\approx 10 - 20$ K). It should then be possible to separate hybridization effects from changes due to the thermal population of excited crystal-field states, despite the logarithmic scale of the Kondo effect.

The experiment was performed at the DEIMOS beamline at synchrotron SOLEIL, in France. The peculiarity of this beamline is the presence of a cryomagnet with an inset that allows XAS to be performed in the mK regime. Below 1K, by ^{3}He-^{4}He dilution refrigeration, a sample temperature of 250 mK can be reached. Temperature stability was guaranteed within a few percent. The temperature difference between sample and thermocouple may vary between 50 and 100 mK, depending on how good thermal contact is. The energy resolution at the Ce $M_{4,5}$ edge ($h\nu \approx$ 870-910 eV) was about 0.4 eV. The samples were cleaved *in situ* with the post-cleaving method along the *ac* plane under UHV conditions (P$\approx 10^{-10}$ mbar) and then transferred under UHV to the insert of the main chamber, where the cryomagnet is located. A picture of a $CeCu_2Si_2$ sample after post cleaving is reported in Fig. 3.8.

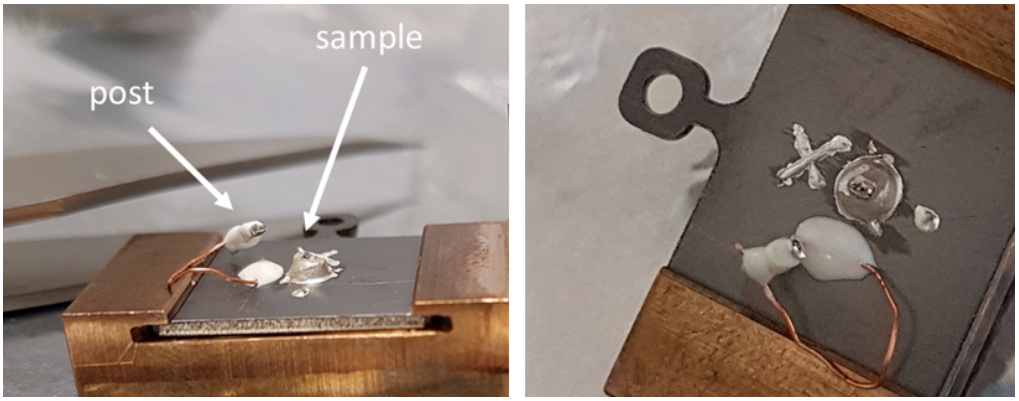

Figure 3.8: *Pictures of the sample, as mounted on the sample holder after the cleave and the experiment. The post and the sample, previously glued, can be distincly seen.*

Spectra were recorded with the total-electron-yield method, that is by measuring the drain current of the sample. This signal was then normalized to the incoming photon flux measured from the current I_0 at the focussing mirror. The measurement was done for the two linear polarizations $\mathbf{E} \parallel c$ and $\mathbf{E} \perp c$, where c is the four-fold tetragonal axis; the LD is defined as the difference between the two: $I_{LD} = I_{\mathbf{E}\parallel c} - I_{\mathbf{E}\perp c}$. Spectra

for the two polarizations were scaled such that their backgrounds match. This scaling is justified by the fact that a change of the polarization requires a different ondulator harmonic, which may lead to the beam hitting the focussing mirror in a different spot and therefore the measured I_0 may change for different polarizations. Several so-called *sandwiches* of $I_{\mathbf{E}\parallel c} - I_{\mathbf{E}\perp c} - I_{\mathbf{E}\perp c} - I_{\mathbf{E}\parallel c}$ were taken at each temperature at different sample spots and then normalized to the integrated intensity.

The data analysis was performed with the full multiplet code *Quanty* [67]. The atomic parameters for the $4f$-$4f$, $3d$-$4f$ Coulomb interactions and of the spin-orbit coupling constants were determined with the Cowan code [37]. Such parameters need to be reduced to account for configuration interaction effects not comprised in the Hartree-Fock scheme. The reductions of about 21% for the $4f$-$4f$ and 39% for the $3d$-$4f$ interactions were determined by optimizing the simulation without crystal-field to the experimental isotropic spectrum $I_{iso} = \frac{I_{\mathbf{E}\perp c} + 2I_{\mathbf{E}\parallel c}}{3}$. Fig. 3.9 (a) shows the experimental isotropic spectrum at 250 mK and Fig. 3.9 (b) the simulation with optimized reduction factors. The reduction factors should not vary with temperature, so that the same values were used for the simulations of the data at other temperatures. The simulation in Fig. 3.9 (b) reproduces the data reasonably well, only the edge jumps (see Chapter 2, Fig. 2.3) and the small satellites on the high energy tail of the main absorption lines are not captured. These satellites are a result of cf-hybridization and they represent the amount of f^0 in the initial state. The simulation, however, is based on a pure ionic single-ion crystal-field model, with only the Ce f^1 configuration. The f^0 satellite peaks ($3d^{10}4f^0 \rightarrow 3d^9 4f^1$ transition) are not present in the simulation, whereas the main absorption lines of the $M_{4,5}$ edges coming from the f^1 contribution in the ground-state ($3d^{10}4f^1 \rightarrow 3d^9 4f^2$ transition) are well reproduced. The f^0 spectral weight, however, does not contribute to the dichroism so that its presence does not affect the crystal-field analysis.

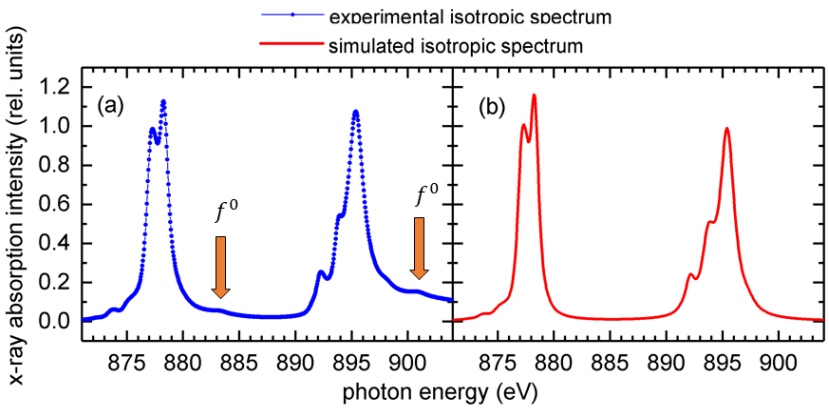

Figure 3.9: *Optimization of the simulated isotropic spectrum (a) to the experimental isotropic spectrum (b), in order to obtain the reduction factors of the 4f-4f and 3d-4f Coulomb interactions. The experimental data are those at 250mK. The orange arrows in (a) highlight the f^0 satellite peaks in the experimental spectrum.*

The detailed procedure utilized in the simulation and analysis of spectra is described in Section 2.1.5. The ground-state wave-function is determined by simulating the linear dichroism $LD = I_{\mathbf{E}\parallel c} - I_{\mathbf{E}\perp c}$, because edge jumps as well as the f^0 satellites cancel out in the LD signal. The temperature dependence of the dichroic signal has then been reproduced by taking into account the thermal occupation of excited crystal- field states, weighting the spectra of each crystal-field state by the corresponding Boltzmann factor.

3.3 Results

3.3.1 Ground-state wave-function from mK data

Figure 3.10 (a) shows the experimental XAS spectra of $CeCu_2Si_2$ at 250mK linear for polarization parallel ($\boldsymbol{E} \parallel c$, red) and perpendicular ($\boldsymbol{E} \perp c$, blue) to the c tetragonal axis.

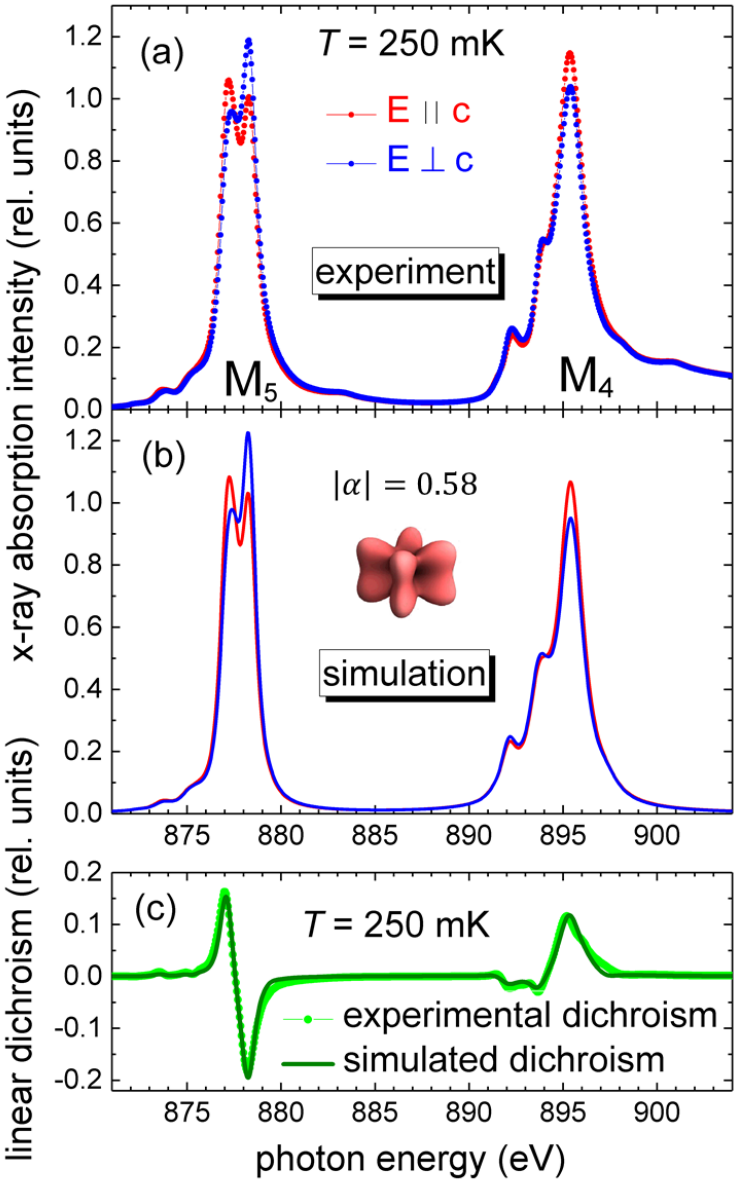

Figure 3.10: *(a) XAS data at 250mK, (b) simulation with Γ_7 ground-state wave-function and mixing parameter $|\alpha| = 0.58$ and (c) linear dichroism $LD = I_{\boldsymbol{E}\parallel c} - I_{\boldsymbol{E}\perp c}$, showing the agreement between data (light green dots) and simulation (dark green line). The inset of (b) shows the charge-density for a Γ_7 orbital with $|\alpha| = 0.58$.*

There is a clear linear dichroism and the comparison with the XAS simulations of the pure J_z states in Fig. 2.6 excludes immediately the Γ_6 as the ground-state because it would have the opposite polarization dependence. Hence, the ground-state symmetry is determined by the Γ_7.

Now the problem has been reduced to determining the mixing factor $|\alpha|$. $|\alpha|$ was obtained by fitting incoherent sums of the XAS spectra of the pure $J_z = \frac{3}{2}$ and $J_z = \frac{5}{2}$ states (for more details see Section 2.1.5). Willers *et. al* found that the ground-state is the Γ_7^- at 20K. Under this assumption, the ground-state wave function can be written as:

$$|gs\rangle = \Gamma_7^- = 0.58 \cdot \left|\pm\frac{5}{2}\right\rangle - 0.81 \cdot \left|\mp\frac{3}{2}\right\rangle$$

By looking at the definition of the states 3.1 it is clear that the Γ_7^+ excited state is also determined:

$$|ex\rangle = \Gamma_7^+ = 0.81 \cdot \left|\pm\frac{5}{2}\right\rangle + 0.58 \cdot \left|\mp\frac{3}{2}\right\rangle$$

The Γ_6 is a pure state, without any free parameter to adjust. Hence, the determination of the ground-state allows for the determination of all crystal-field levels.

3.3.2 Temperature dependence of the linear dichroism

In this section the variation of the LD within the temperature range from 250 mK to 250 K is discussed. We recall that the thermal occupation of higher crystal-field states upon rising the temperature results in a superimposed LD signal, adding to the one from the ground-state. If all three doublets are equally thermally populated, the dichorism becomes zero, since the electron distributions of the crystal-field split Hund's rule ground-state add up to a sphere.

Figure 3.11 (a) and (b) show the experimental LD from 250 mK to 250K. Starting from 250 mK, upon rising the temperature, the LD remains unchanged up to 5K. At 25 K a slight increase is registered (see inset of Fig. 3.11 (a)). It is then slightly reduced at 150 K and even more so at 250 K.

Fig. 3.11 (c) and (d) show the simulated LD. The simulations take into account the thermal population of the excited states Γ_7^+ at 29 $\pm$ 1 meV and Γ_6 at 33 $\pm$ 1.5 meV. The experimental decrease of the LD with rising temperature is grasped fairly well by just considering the thermal occupation of the excited states. The only thing that the simulation seems to fail to capture is the slight increase of the LD at 25K.

The reduction of the dichroism at 150 and 250 K can overall be ascribed to the population of the higher crystal-field states, captured by our simulated dichroism. For completeness, Fig. 3.12 also shows the experimental XAS data and the simulations for the whole range of temperatures. There as well, the only noticeable change of the spectra happens at high temperature because of thermal population of higher crystal-field states.

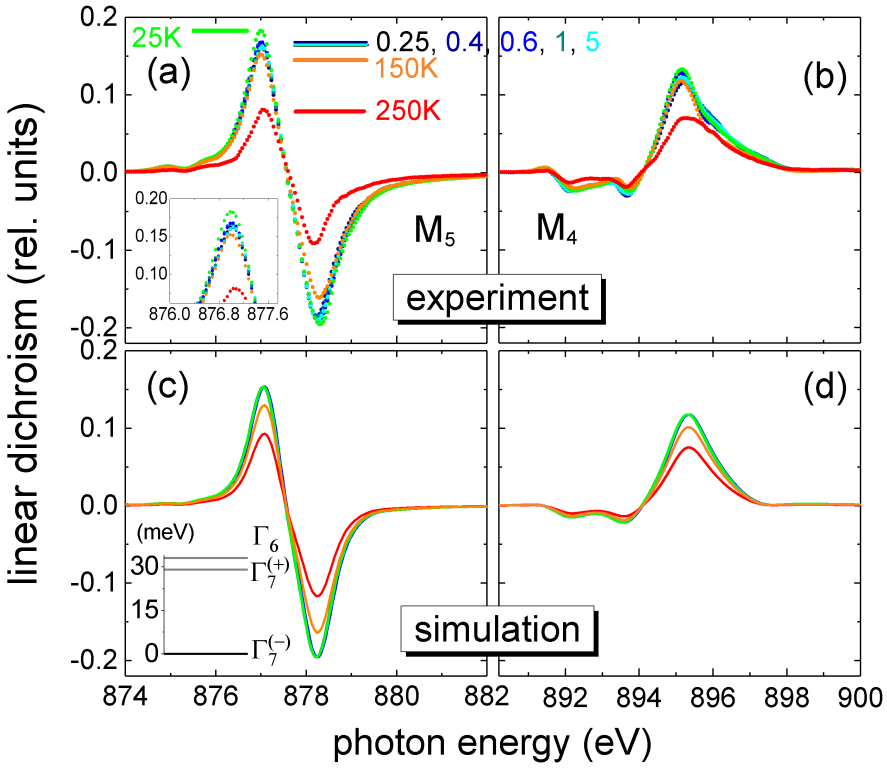

Figure 3.11: *Temperature dependence of the linear dichroism at the M_5 and M_4 edges: (a) and (b) are the experimental data, (c) and (d) the simulations. In the inset of (a) a zoom into the M_5 edge LD is represented. In that of (d) the crystal-field level scheme is reported.*

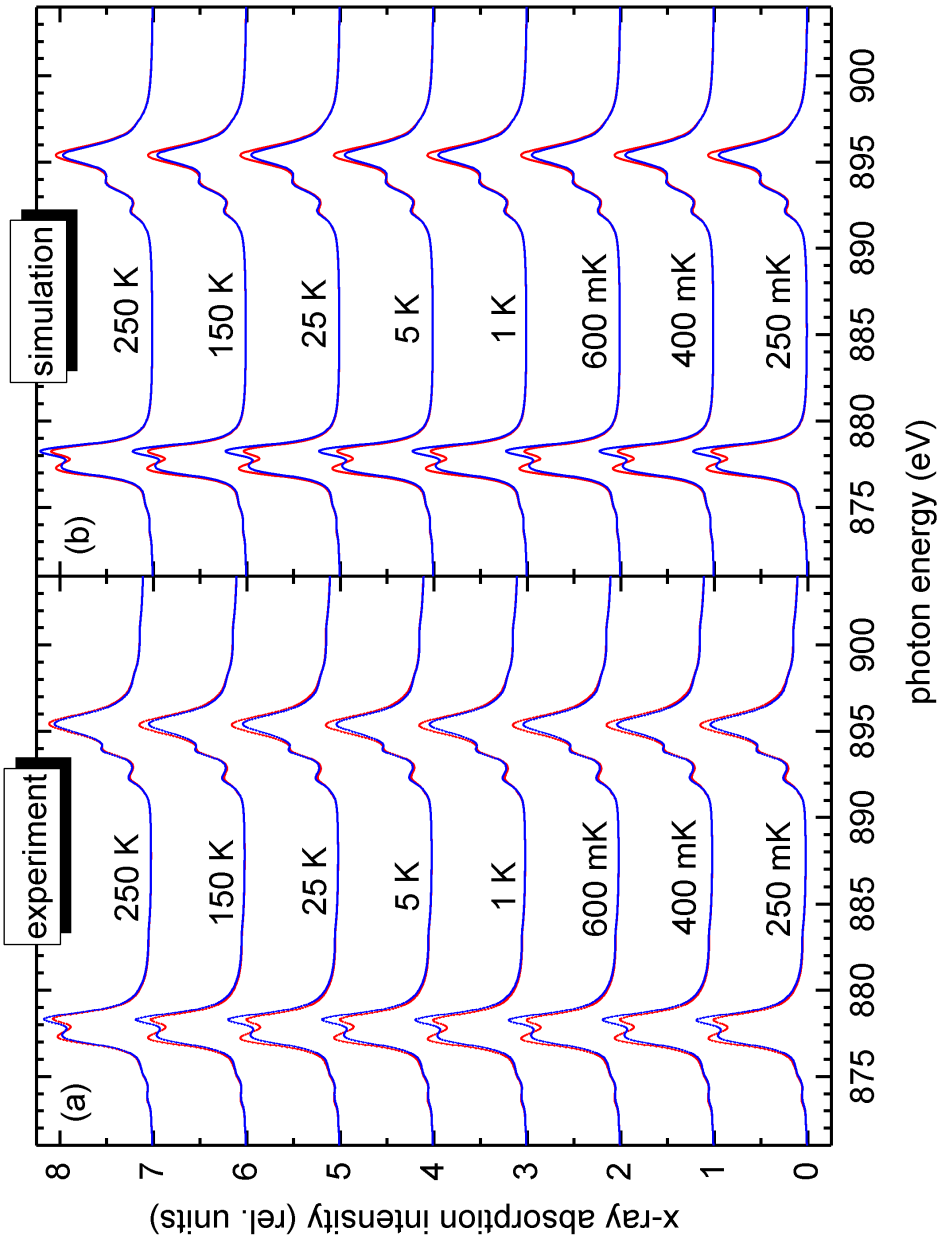

Figure 3.12: *Experimental (a) and simulated (b) XAS spectra from 250 mK to 250 K. The experimental spectra show some change at high temperature. The simulations, by only taking into account the thermal population of the crystal-field state, reproduce the data well.*

3.3.3 Temperature dependence of the $4f^0$ electron count

In this paragraph the relative $4f$ shell electron count is investigated. Fig. 3.13 shows the experimental isotropic spectra at different temperatures. They fall well on top of each other, since by construction ($I_{iso} = \frac{I_{\mathbf{E}\perp c}+2I_{\mathbf{E}\parallel c}}{3}$) the isotropic spectra show no polarization dependence. At a closer look, however, it can be seen that the small bumps at slightly higher energies than the main absorption edges show a temperature dependence. These satellite peaks are due to hybridization and the presence of some f^0 contribution in the ground-state.

Fig. 3.13 (b) and (c) show an enlargement of the f^0 satellite peaks in the isotropic spectra as a function of temperature, for the M_5 and M_4 edges respectively. The data from 250 mK to 5 K show very little variation and a decreasing trend is then established when rising the temperature to 25K, even more so at 150 and 250 K.

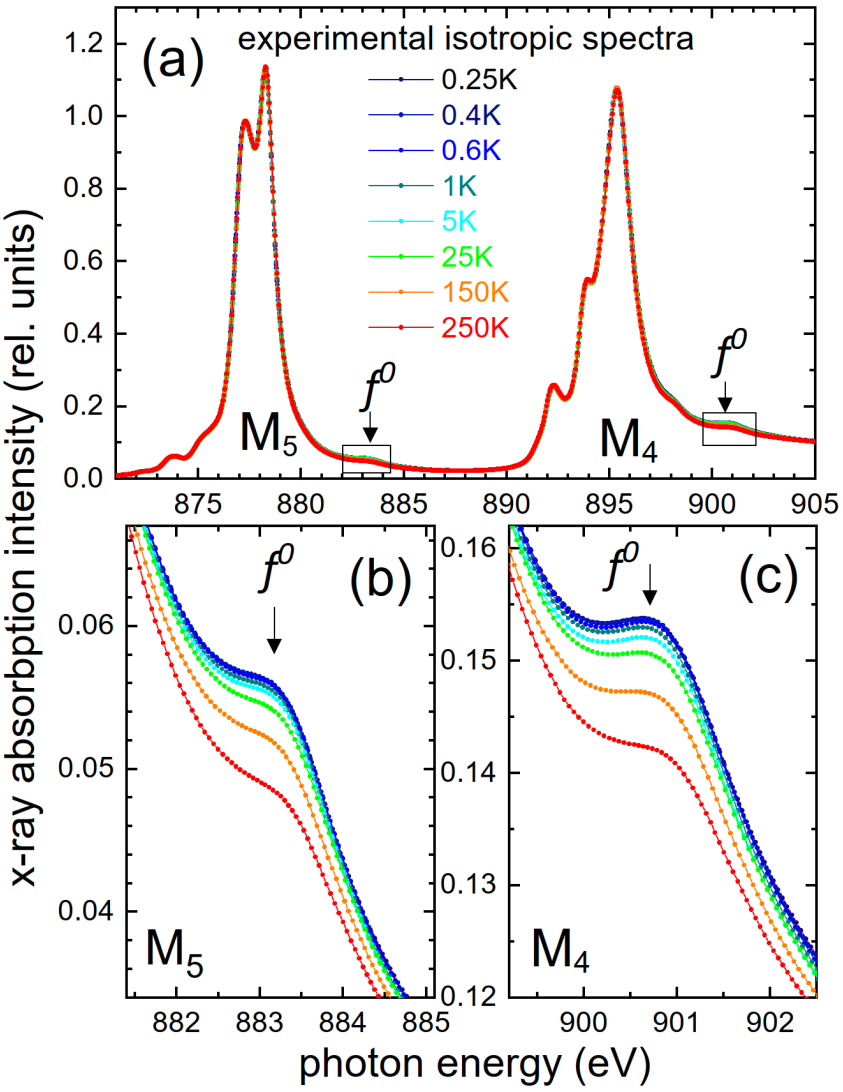

Figure 3.13: *Experimental isotropic spectra and their temperature dependence (a). (b) and (c) are enlarged regions corresponding to the small black rectangles in (a). The bumps in those regions are due to $4f^0$ intensity.*

3.4 Discussion

At 250 mK the temperature is so low that only the ground-state is significant to the spectra: it is then clear that the $\Gamma_7^{\pm}$ ground-state reproduces well the experiment with $|\alpha| = 0.58$. The sign + or - cannot be determined because XAS is a dipole limited technique. However, we can identify such a state with a Γ_7^- because of what was found in Ref. [64].

Looking at the temperature dependence of the LD and the corresponding simulations exclusively based on a single ion crystal-field model it is clear that the overall trend of the LD is explained in terms of thermal occupation of the excited-crystal field levels: as the temperature rises the quasi-quartet at ≈ 30 meV gets populated and the dichroism decreases. The ground-state wave-function as determined by the mK LD is showing no change, other than the effect coming from thermal population of excited crystal field-states.

The only aspect eluding the explanation of the temperature dependence of the dichroism in terms of thermal population of excited crystal-field states is the slight increase of the LD at 25K. Its origin might be trivial and could be due to some experimental artifact, although not clearly identified. A possibility could be that there are small shifts in energy. It should be noted that the beamline DEIMOS at SOLEIL does not work with reference samples in the beam, that could be used for aligning the spectra in energy. However, it could also be the physical fingerprint of the presence of hybridization we are expecting to see in one way or the other. In order to prove this it will be necessary to acquire data on a finer temperature mesh between 5 and 150 K. Such an experiment is already allocated for the end of December.

In the following potential fingerprints of hybridization in the present XAS data are discussed. The activation of hybridization at low temperature is clearly visible from the temperature trend of the f^0 satellite peaks in the isotropic spectrum (see Fig. 3.13 (b) and (c)). The absolute f occupation of the initial state can be deduced from the measured spectral weights only by performing a configuration interaction calculation (as described in Ref. [68]). However, it would involve the combination of a full-multiplet as well as configuration interaction calculation because the M-edges show a pronounced multiplet structure. Nevertheless, the temperature trend may be used as an estimation of the Kondo temperature. This is based on the ideas of Bickers, Cox and Wilkins [69], who have shown a correlation between the Kondo temperature and the f-shell occupation. Tjeng *et al.* applied it to $YbAl_3$ [15]. Figure 3.14 shows the f-shell occupation $n_f(T)$ of $YbAl_3$ against log(T) whereby the inflection point denotes T_K.

Accordingly, the temperature dependence of the f^0 spectral weight of $CeCu_2Si_2$ has been determined by subtracting a linear background from the satellite peaks highlighted by the little rectangles in Fig. 3.13 (a) for the M_5 and M_4 edge. The linear backgrounds in these ranges were chosen in order to pull to zero the f^0 intensity at 882.3 and 884.7 eV for the M_5 edge and at 899.8 to 902.5 eV for the M_4 edge, at all temperatures. Fig. 3.15 shows the f^0 satellite peaks of the isotropic spectra at different temperatures, once linear backgrounds have been subtracted.

Then, the integrated intensities $\tilde{n}$ of the spectra in Fig. 3.15 are taken as the relative f^0 contributions to the ground-state and in Fig. 3.16 the f-shell occupation $(1 - \tilde{n})$ is plotted against log(T). The temperature dependence is reminiscent of Fig. 3.14, but it does not show an inflection point, probably due the increasing population of excited crystal-field states. Such an issue in determining the Kondo temperature by means of the f^0 spectral weight has been pointed out by Kummer *et al.* [70]. Nonetheless, here, the f^0 spectral weight starts to decrease above 10 K, which is in agreement with a Kondo temperature of 10-20K.

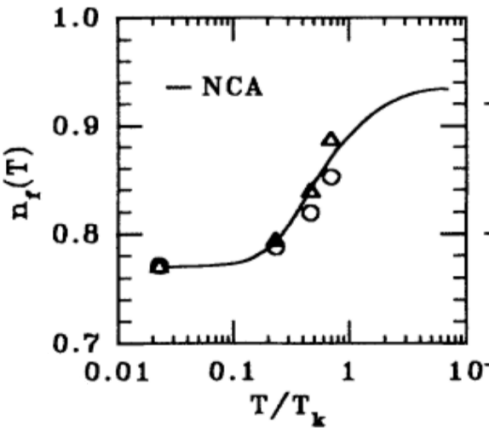

Figure 3.14: *Figure from Ref. [15]. f-shell occupation $n_f(T)$ of $YbAl_3$ against log(T), as obtained from the $4f^{13}_{\frac{7}{2}}$ PES intensities. Circles and triangles indicate different methods of estimating the bulk PES intensity. The solid line is a calculation done with the Anderson impurity model,in the noncrossing approximation (NCA).*

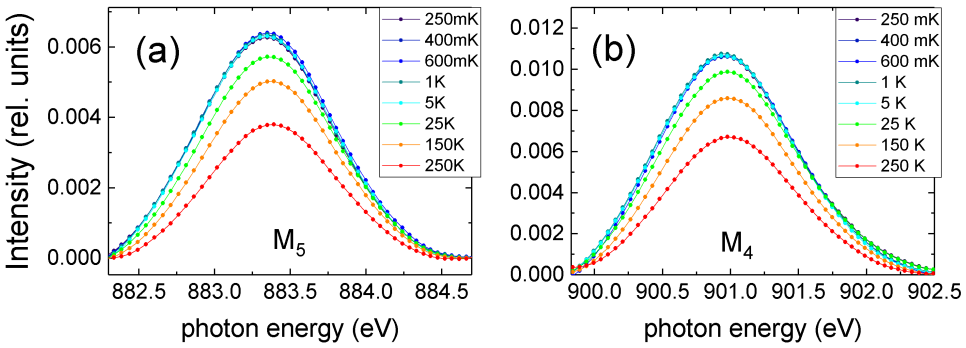

Figure 3.15: *f^0 satellite peaks of the isotropic spectra at different temperatures, once linear backgrounds have been subtracted, for the M_5 (a) and M_4 (b) edge.*

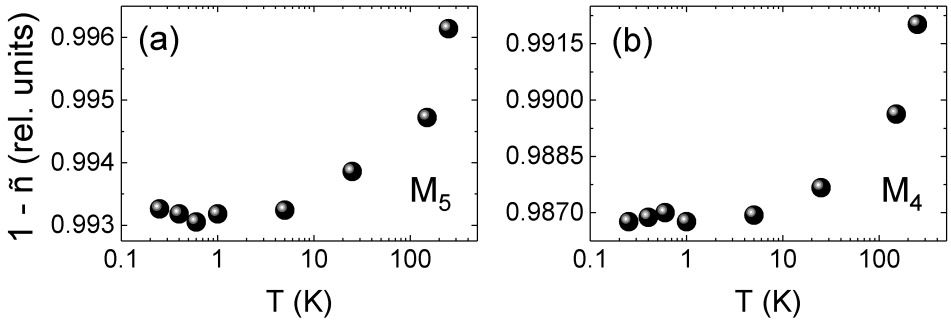

Figure 3.16: *Integral of the f^0 intensity highlighted by the small rectangles in Fig. 3.13 (a) plotted against* $\log T$.

The temperature dependence of the f^0 spectral weight shows the diminishing impact of the Kondo effect as temperature rises and how XAS is sensitive to it. Hence, we now look again at the temperature dependence of the LD and consider the singular data point at 25 K, that cannot be explained with thermal occupation of excited crystal-field states only. We discuss different possible scenarios justifying the increased LD at 25 K:

- In the Kondo regime the LD is diminished due to presence of the f^0 spectral weight. Some f^0 spectral weight would suggest some loss of f^1 spectral weight and hence some loss of LD, since the f^0 state does not give rise to dichroism. As temperature rises the Kondo effect is less effective: only then the undisguised LD due to the crystal-field anisotropy shows up. Possibly, this is the effect we see at 25K, i.e. at $T < 25$ K the LD is diminished and it starts to recover at $T > 25$ K. A solid proof of this scenario requires more temperature points between 5 and 150 K.

- An excited crystal-field state could mix into the ground state and lead to a decrease of LD as long as the Kondo effect is effective. The simulated dichorisms of the single crystal-field states are plotted in Fig. 3.17.

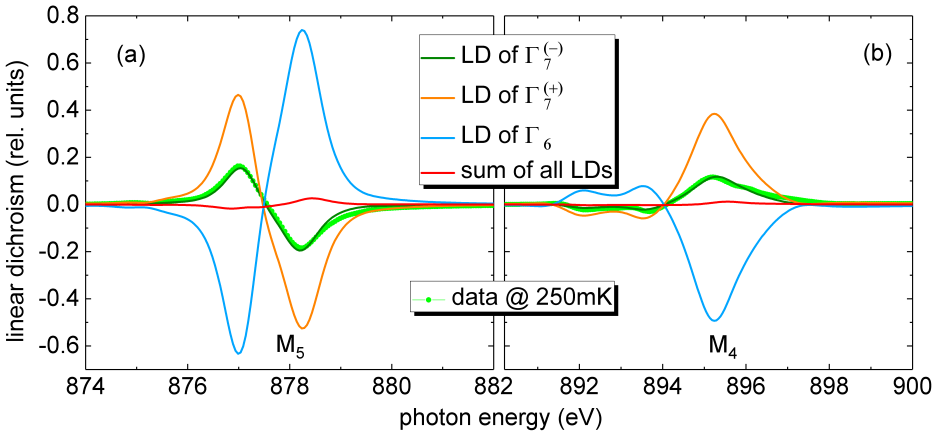

Figure 3.17: *Individual simulated linear dichroism of the three crystal-field doublets Γ_7^- (dark green), Γ_7^+ (orange) and Γ_6 (light blue) at the M_5 (a) and M_4 (b) edges. The experimental data are fitted well by the Γ_7^- dichroism. Notice that the sum is not exactly zero because of the impact of the crystal-field in the final state of the absorption process.*

The LD of the Γ_6 is opposite in sign to that of the Γ_7^- ground-state, whereas the LD of the Γ_7^+ is of the same sign and much larger than that of the ground-state. An intermixing of the Γ_7^+ into the ground-state at low T can therefore be excluded since it would lead to a wrong temperature dependence. The LD would not be reduced at low T. On the other hand, an intermixing of the Γ_6 can lead to the correct reduction of the LD. We construct a simulation by summing the dichroisms of the Γ_7^- and Γ_6 states with given weights to fit the experimental dichroism at low temperature:

$$LD = aLD_{\Gamma_7^-} + (1-a)LD_{\Gamma_6} \tag{3.2}$$

It turns out a $a = 3\%$ admixture of the Γ_6 into the ground-state can account for the experimental data.

We can now look at the conjecture of Pourovskii *et. al* [14] in the light of the measured dichorism. What can be compared to the experiment is the theorized orbital reoccupation happening at 0 GPa, from a 60 % Γ_7^+ and 40 % Γ_7^- at 7 K to a 20 % Γ_7^+ and 80 % Γ_7^- at 60 K. The dichroism at 7 K can be simulated as

$$LD_{7K}(\alpha^2) = 0.6LD_{\Gamma_7^+} + 0.4LD_{\Gamma_7^-} \tag{3.3}$$

which, as explained in Section 2.1.5, can be interpreted in terms of incoherent sums of pure J_z states as:

$$LD_{7K}(\alpha^2) = 0.6[(1-\alpha^2)LD_{\frac{5}{2}} + \alpha^2 LD_{\frac{3}{2}}] + 0.4[\alpha^2 LD_{\frac{5}{2}} + (1-\alpha^2)LD_{\frac{3}{2}}] \tag{3.4}$$

If α is optimized to reproduce the experimental dichroism, it turns out that the best fit is obtained with $\alpha^2 = 1$:

$$LD_{7K}(\alpha^2 = 1) = 0.6LD_{\frac{3}{2}} + 0.4LD_{\frac{5}{2}} \tag{3.5}$$

The red dashed line in Fig. 3.18 shows how $LD_{7K}(\alpha^2 = 1)$ compares to the data. If the same α value is used to calculate the dichroism for the suggested mixing at 60K

$$LD_{60K}(\alpha^2 = 1) = 0.2LD_{\Gamma_7^+} + 0.8LD_{\Gamma_7^-} \tag{3.6}$$

a much higher dichroism (dashed blue line in Fig. 3.18) than the one experimentally observed is obtained.

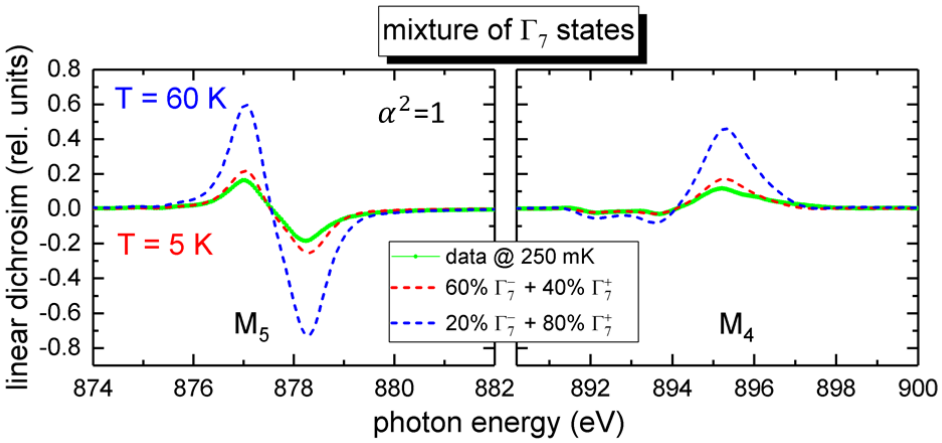

Figure 3.18: *Simulated dichroism based on the* Γ_7 *admixture by Pourovskii et al. [14] at 5 K (red dashed line) and 60 K (blue dashed line). The best fit, giving the smaller dichroism, is obtained for* $\alpha = 0$.

To summarize, the temperature dependence of the linear dichroism of $CeCu_2Si_2$ is well reproduced by taking into account the thermal occupation of excited crystal-field states at 30 meV. Only the LD at 25 K seems unusually larger. Although the reason could be trivial, since of experimental origin, scenarios have been discussed on how this could be explained in terms of the presence of hybridization of $4f$ and conduction electrons. On the basis of the unchanged dichroism below 150 K, an orbital reoccupation happening between the Γ_7 states seems unlikely.

Chapter 4

YFe_2Al_{10}

In this chapter the electronic structure of Fe in YFe_2Al_{10} is characterized by means of x-ray absorption (XAS) and photoelectron spectroscopy (PES).

Strongly correlated electron systems show a plethora of different ground-states, as a consequence of the interplay between competing interactions. The presence of a quantum critical point, which is a zero temperature phase transition, is ubiquitous in their phase diagrams, where an infinitesimal modification of composition, pressure or field can drive the system into one of its phases. As a consequence, quantum critical behaviour is often hidden by the onset of different phases near the QCP, making it difficult to univocally address it. YFe_2Al_{10} does not order magnetically down to 0.1 K [71], although an effective magnetic moment of the order of $0.5\,\mu_B$ has been determined from the slope of the static susceptibility in the temperature range 150 to 750 K [72, 73]. Detailed measurements of magnetic susceptibility, specific heat and resistivity suggest that YFe_2Al_{10} is on the verge to ferromagnetism at 0 K whereby applied magnetic fields tune the system away from the QCP [16].

4.1 Introduction

YFe_2Al_{10} crystallizes into an orthorhombic structure, described by the symmetry group *Cmcm* (no. 63). The material has a layered structure with nearly square nets of Fe atoms on the *ac* planes [74], as shown on the left in Fig. 4.1.

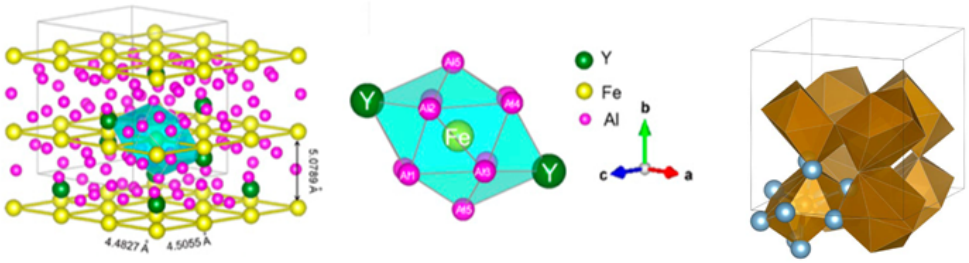

Figure 4.1: *Figure adapted from Ref. [16]. Layered crystal structure of YFe_2Al_{10} (left) and local octahedral Al-Y structure surrounding a single Fe atom (centre) and representation of several octahedral structure (right), one tilted with respect to the other. The unit cell is indicated by gray lines.*

The middle of Fig. 4.1 shows how each Fe atom is surrounded by a distorted octahedron

of Al atoms, capped with Y atoms, and the right-hand side of Fig. 4.1 points out how the Al octahedra are tilted one with respect to the other. Also other Fe aluminides like $CeFe_2Al_{10}$ and $YbFe_2Al_{10}$ have been investigated but in that case the Ce and Yb ion carry large effective moments of 3-5 μ_B. In YFe_2Al_{10} the magnetism that gives rise to the effective moment can only come from the the Fe ions since Y is a non magnetic ion. It is puzzling that the Fe sublattice does not order magnetically so that the natural question is: what prevents the Fe sublattice from ordering? It has been speculated that the correlations that drive the system to the brink of ferromagnetic order are derived from the hybridization of the Fe-based d-electrons with conduction electrons [16] in analogy to the Kondo effect in f-electron systems. Alternatively, the hopping of Fe d-electrons could be so strong that the valence state of Fe is ill defined. Disorder effects are known to be minimal, since single crystal x-ray diffraction measurements exhibit no evidence of deviations from stoichiometry or site disorder [74].

YFe_2Al_{10} could offer the possibility to experimentally access and gain insight into the undisguised quantum critical behaviour without corruption of other phases. The quantum critical behaviour of YFe_2Al_{10} has been investigated with magnetic susceptibility, specific heat and electrical resistivity measurements in Ref. [16] and with magnetization, magnetic nuclear resonance and nuclear quadrupole resonance in Ref. [75]. All experiments observe a crossover from quantum critical behaviour to ordinary Fermi liquid behaviour with increasing magnetic field. As an example, the dc suceptibility of YFe_2Al_{10} below 30 K is shown on a double logarithmic scale for applied fields from 0.05 to 6 T in Fig. 4.2. It shows that the susceptibility is showing saturation effects with applied field; it actually seems to diverge for $B \to 0$ T whereas it amounts to only $\approx 10^{-3}$ emu/mol Fe for applied fields between 2 and 6 T [16, 75, 71].

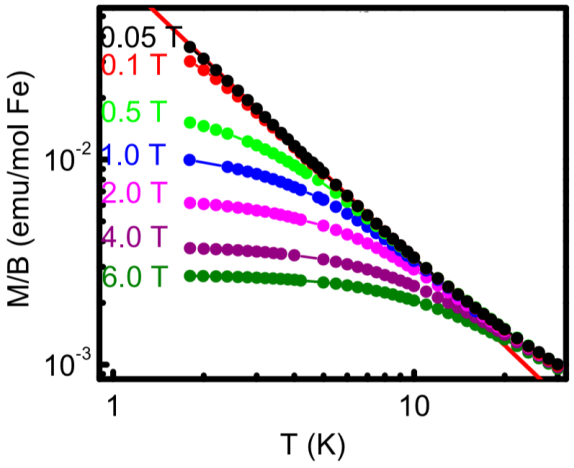

Figure 4.2: *Figure adapted from Ref. [16]. Temperature dependence of the dc susceptibility at different fixed fields.*

4.1.1 Motivation

Fe is the only magnetic atom in YFe_2Al_{10} so that the magnetism most likely comes from it. PES, XAS and also XMCD are element specific probes that not only will confirm or disprove that the magnetism comes from the Fe and not from impurities, but will also give insight into the valence state of Fe in YFe_2Al_{10}.
In a one-electron picture the weight given to a given configuration is purely statistical

whereas correlations tend to favour some configurations over the others. The characterization of YFe_2Al_{10} was started with density functional theory (DFT) and dynamical mean field theory (DMFT) calculations [1] by Philipp Hansmann at MPI-CPfS. Figure 4.3 shows the theoretical expected d-shell filling of the Fe ions for U = 0 and 4 eV, U being the *d-d* Coulomb repulsion. It turns out that for U = 0 eV the *d*-electron filling is an almost Gaussian distribution very much centered around 7, i.e. suggesting a Fe d^7. For U = 4 eV the distribution becomes narrower and the centering around 7 becomes more pronounced.

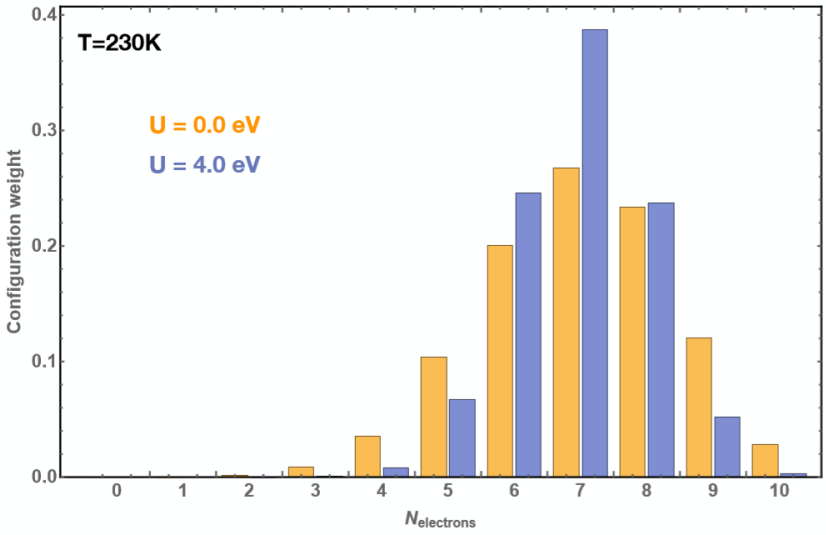

Figure 4.3: *Configuration distribution calculated from DMFT for U = 0 eV (yellow) and U = 4 eV (blue).*

In a d^6 low-spin configuration 3 electrons would have spin ↑ and the remaining 3 spin ↓, meaning that the total spin is minimized, thus giving rise to a rather low magnetic moment. Conversely, a d^7 configuration could hardly support the absence of moments, unless the magnetic moment is somehow *screened* by the conduction electrons.

Experiments were set up with the aim to spectroscopically investigate:

- the electronic structure of YFe_2Al_{10}, in particular the role played by correlations, with valence band PES.
- The valence state of Fe with XAS,
- The magnetic moment carried by the Fe atoms with XMCD.

The high resolution valence band PES data are compared with results from DFT and DMFT calculations. The XAS data are compared with data of oxide references of which the valence states are known. The susceptibility and magnetic moments are calculated from XMCD.

[1] DFT and DMFT are methods to calculate the electronic structure of materials. DFT is based on a single-particle approach and determines the properties of the system by using functionals of the spatially dependent electron density. DMFT is the method of choice for strongly correlated materials. It maps the many-body lattice problem to a many-body local problem, called impurity problem.

4.2 Experiment

Single crystals of YFe_2Al_{10} were provided by Meigan Aronson's group at the University of British Columbia, Vancouver, Canada.

The valence band PES measurements were performed at liquid nitrogen temperature at the TPS 45a beamline of the Taiwan Photon Source in Hsinchu, with 664.2 eV photon energy, and in the XPS lab at the MPI-CPfS in Dresden, with 1486.7 eV photon energy coming from an Al Kα source. In both cases the samples were cleaved *in situ* just before measuring and the energy resolution was 87 meV in Taiwan and 300 meV in Dresden. The work function of the analyzer was determined by measuring the Fermi edge of a gold reference sample. The measured valence bands were compared to DFT and DMFT calculations. The calculations incorporate the presence of on-site repulsion between electrons expressed in the parameter U. Calculations were performed for $U = 0\,eV$ and for $U = 4\,eV$, in order to estimate the degree of correlation of the systems. The calculations were done for 230 K. In order to compare the experimentally measured VB with the DFT and DMFT results, the calculated single particle spectral functions for Al3p, Al3s, Y4d, Y5s and $Fe3d$, making up the valence band, were manipulated in the following manner:

- they were multiplied by the Fermi function at the temperature of the experiment.
- They were convoluted by a Gaussian lineshape having full width at half maximum equal to the experimental resolution. This was not done for the DMFT calculations since they already exhibit a large inherent broadening.
- They were multiplied by the corresponding photoionization cross-sections at the photon energy used in the experiment. Cross-section are tabulated in Ref.s [17, 18].
- They were finally summed up to give the simulated valence band.

XAS data were recorded at the TPS 45a beamline of the Taiwan Photon Source in Hsinchu, while XMCD data were recorded at the BOREAS beamline at ALBA synchrotron in Spain, where a static magnetic field can be applied along the beam direction. In both cases the photon energy was tuned to the Fe $L_{2,3}$ absorption edge. The energy resolution was around 0.4 eV. The samples were cleaved *in situ* under UHV conditions ($P \approx 10^{-10}$ mbar) in dedicated chambers with the knife-cleave method and then transferred under UHV to a main chamber, where the measurement was performed at liquid nitrogen temperature. A picture of a YFe_2Al_{10} sample mounted for knife-cleaving for an absorption experiment is reported in Fig. 4.4.

Figure 4.4: *Picture of a YFe_2Al_{10} mounted on a sample holder for knife cleaving. The glue is covering the sample to fix it, the top part of the sample is left with no glue to allow the cleave.*

Spectra were recorded with the total-electron-yield method (TEY), that is by measuring the drain current of the sample. This signal was then normalized to the incoming photon flux measured from the current I_0 at the focussing mirror. As far as the XAS measurement is concerned, the sample was not oriented along any specific direction, whereas for the XMCD the measurement was performed for two circular polarizations C^+ and C^- with crystals having the c and b axis parallel to the field (and beam). Spectra for the two polarizations were scaled such that their backgrounds match. The XMCD is defined as the difference of spectra taken with different polarization: $XMCD = I_{C^-} - I_{C^+}$.

4.3 Results

4.3.1 Valence band PES and comparison with DFT and DMFT calculations

Fig. 4.5 shows a comparison between the valence band (VB) PES spectra of YFe_2Al_{10} measured with 664.2 eV photon energy (87 meV resolution) and measured with 1486.7 eV photon energy (300 meV resolution). Apart from the inherent larger broadening of the 1486.7 eV photon energy data, the main difference between the two spectra is manifested as a shift of the main peak of about 0.1 eV.

In order to clarify the possible reason of such a shift, the results of DFT and DMFT can be addressed. Fig. 4.6 shows the density of states (DOS) as calculated from DFT. It can be seen that Fe $3d$ is the main contribution to the VB. Fig. 4.7 shows the single particle spectral functions as calculated by DMFT with $U = 0\,eV$ and $U = 4\,eV$. Upon including the repulsive interaction between electrons $U \neq 0\,eV$, the simulated valence band exhibits a shift of the spectral weight from the region near the Fermi level to incoherent excitations at higher binding energies.

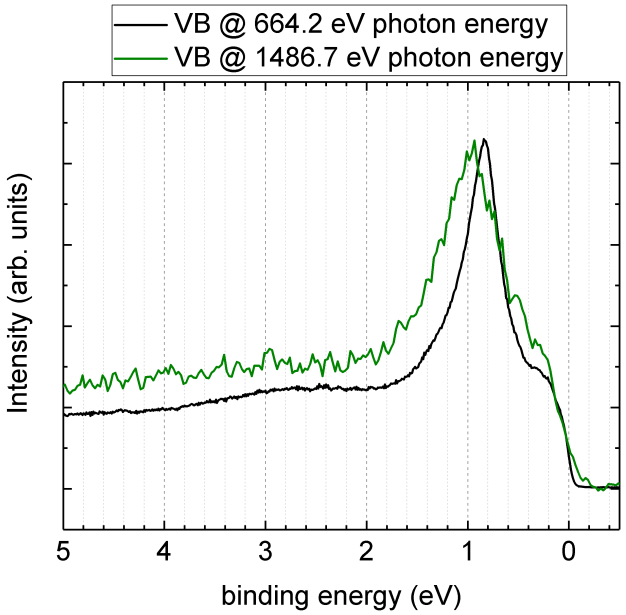

Figure 4.5: *Valence band PES spectrum measured at 664.2 eV and 87 meV resolution (black) and 1486.7 eV and 300 meV (green) photon energy.*

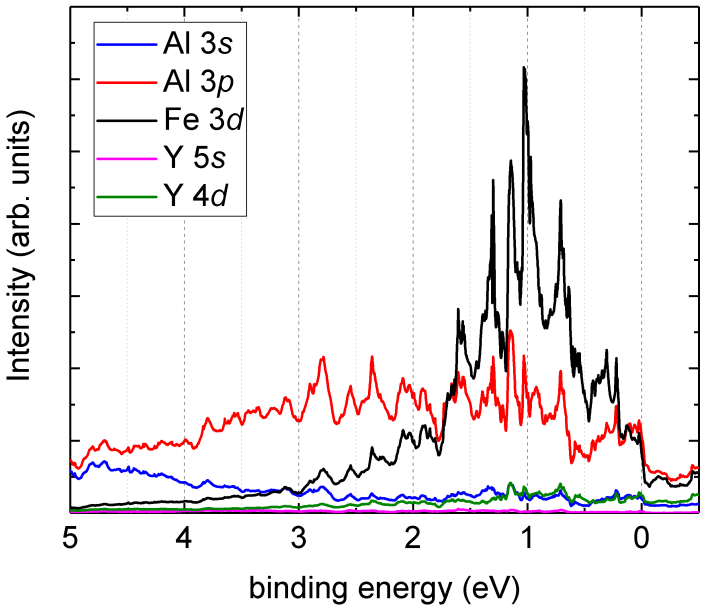

Figure 4.6: *DFT density of states.*

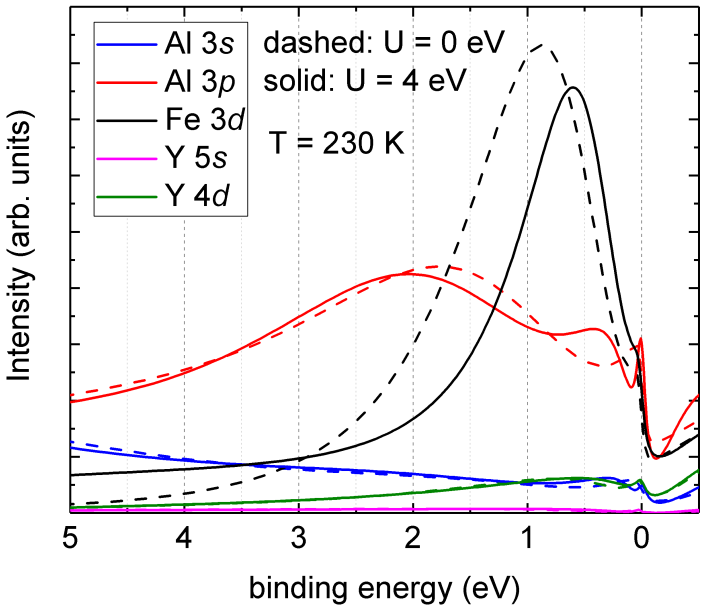

Figure 4.7: *DMFT single particle spectral functions for U=0 eV and U=4 eV.*

The main Fe $3d$ contribution, in particular, looks less broad and is shifted towards the Fermi level. The VB is dominated by the Fe $3d$ contribution just below the Fermi level, determining the main peak observed in the experiment. The Al $3p$ and $3s$ contributions become more relevant at slightly higher binding energies, while the Y $5s$ and $4d$ contribute very little to the valence band.

The impact of the photoionization cross-sections could be responsible for the observed shift since the energy dependence of the cross-sections is different for the respective elements. This will be investigated below. Table 4.1 reports the photoionization cross-sections of the Al, Fe and Y sub-shells considered here, as taken from Ref.s [17, 18]. The Al cross-sections at 1487 eV, as compared to the Fe ones, are indeed much higher than at 664.2 eV. One can then, for example, consider the DMFT single particle spectral functions, multiply them by the different cross-sections at different photon energies and see how the Al contribution is affecting the spectra at different photon energies. Fig. 4.8 shows the DMFT valence band (with U=0 eV) corrected with the cross-sections, at 1486.7 eV and 664.3 eV photon energies. The stronger Al contribution at 1487.6 eV photon energy does cause a higher intensity at binding energy higher than 2 eV. However, the position of the main peak seems to be shifted of only about 0.02 eV.

Photoionization cross sections σ per electron [kb]		
sub-shell	$h\nu = 664$ eV	$h\nu = 1487$ eV
Al $3s_{\frac{1}{2}}$	2.628	0.362
Al $3p_{\frac{1}{2}}$	0.816	0.046
Fe $3d_{\frac{3}{2}}$	9.124	0.379
Fe $3d_{\frac{5}{2}}$	8.981	0.370
Y $5s_{\frac{1}{2}}$	1.027	0.210
Y $4d_{\frac{3}{2}}$	5.254	0.428

Table 4.1: *Photoionization cross-sections at 664 eV and 1487 eV for the Al* $3s$ *and* $3p$*, Fe* $3d$*, Y* $5s$ *and* $4d$ *sub-shells. The values have been obtained via linear interpolation from the values given in [17, 18].*

Figure 4.9 shows the comparison between the measured VB PES spectra at 664.2 eV (a) and 1486.7 eV (b) photon energy with the DFT calculations, corrected by the cross-sections. Figure 4.10 shows the same comparison with the DMFT calculations, corrected by the cross-sections: the 664.2 eV data are compared to the U = 0 eV and U = 4 eV calculation in (a) and (b) respectively, while the 1486.7 eV data are compared to U = 0 eV and U = 4 eV calculation in (c) and (d).

The DFT calculation yields a DOS that peaks at binding energies that are slightly too high, more evidently for the 664.2 eV photon energy data (Fig. 4.9 (a)) than from the 1486.7 eV photon energy data (Fig. 4.9 (b)). Moreover, the shape of the calculation is broader than the experimental data.

As for the DMFT calculation, the calculation with U = 4 eV gives rise to a narrower peak that reproduces the data better but the main part of the DOS is shifted more towards the Fermi edge so that it overlaps worse with the experimental VB curves. Despite an excessively large inherent broadening, the U = 0 eV DMFT calculation seems to fit better the experiment for both photon energies. The main calculated peak of the DMFT (U = 0 eV) calculation, if we compare to the high-resolution data (664.2 eV photon energy, see Fig. 4.10 (a)), is still slightly shifted towards higher binding energies. This is in accordance with the DFT calculation, which should indeed coincide with the DMFT (U = 0 eV) calculation, apart from the broadening. A smaller value of U than 4 eV, e.g. U = 1 or 2 eV, should be able to fit the peak position correctly.

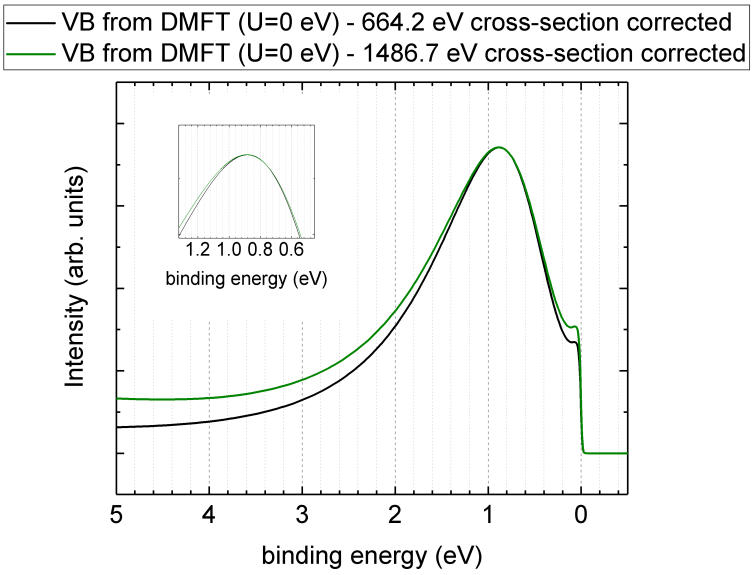

Figure 4.8: *Valence band calculated from the DMFT (U=0 eV) single particle spectral functions, weighed by the corresponding sub-shell cross-section at 664.2 eV (black) and 1486.7 eV (green). In the inset a blow-up of the main peak of the valence band at roughly 0.9 eV binding energy is shown.*

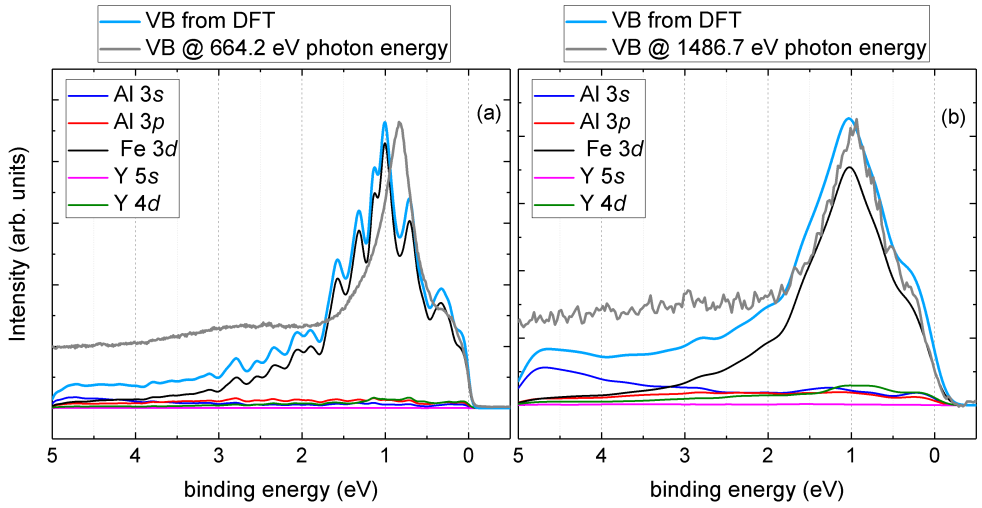

Figure 4.9: *Comparison between the DFT calculations and the measured VB PES spectra, (a) with 664.2 eV y and (b) with 1487.6 eV photon energy. In all the graphs the contribution from the single sub-shells, weighted by the cross-sections, are also reported.*

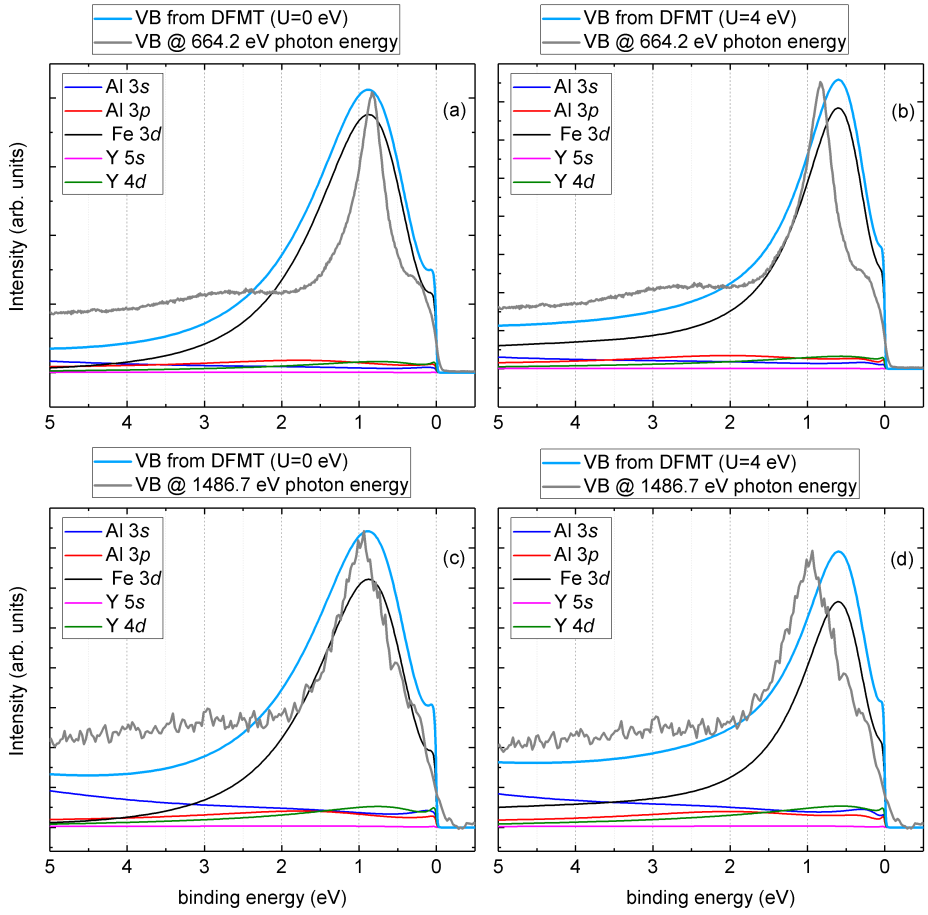

Figure 4.10: *Comparison between the measured VB PES spectra and the DMFT calculations. (a) 664.2 eV data and $U = 0$ eV simulation, (b) 664.2 eV data and $U = 4$ eV simulation, (c) 1487.6 eV data and $U = 0$ eV simulation and (d) 1487.6 eV data and $U = 4$ eV simulation. In all the graphs the contribution from the single sub-shells, weighted by the cross-sections, are also reported.*

4.3.2 XAS and comparison with reference samples

XAS is a powerful technique to probe the valence state, since even small changes in the valence have a high impact on the core hole potential and significantly modify the multiplet structure [39, 40, 41, 42, 43, 44, 45, 46, 47, 48].

The XAS Fe $L_{2,3}$ spectrum of YFe_2Al_{10} is plotted In Fig. 4.11, along with the spectra of three different iron oxide references. The three reference spectra of Fe_2O_3, Fe_3O_4 and FeO were provided by Zhiwei Hu from MPI-CPfS. The respective configurations of Fe are d^5, $d^{5.33}$ and d^6, corresponding to valence states of 3^+, 2.66^+, and 2^+. Figure 4.11 shows that the spectra are shifted towards lower photon energies for larger d-shell fillings (smaller valences). A clear multiplet structure cannot be observed in YFe_2Al_{10}, as compared to e.g. Fe_2O_3, because of its metallic nature. Furthermore, the L_3 edge of Fe in YFe_2Al_{10} peaks at higher photon energies than the one of the d^6 but at lower energies than the $d^{5.33}$ configuration. Hence, the comparison to the references suggests that the valence of Fe in YFe_2Al_{10} is larger than 2^+, but closer to 2^+ than in Fe_3O_4. The peak position of the L_3 edge does not not suggest a d^7 configuration. However, the energy distribution of the L_3 edge of YFe_2Al_{10} is fairly broad, thus allowing the possibility of a distribution of several configurations centered close to d^6.

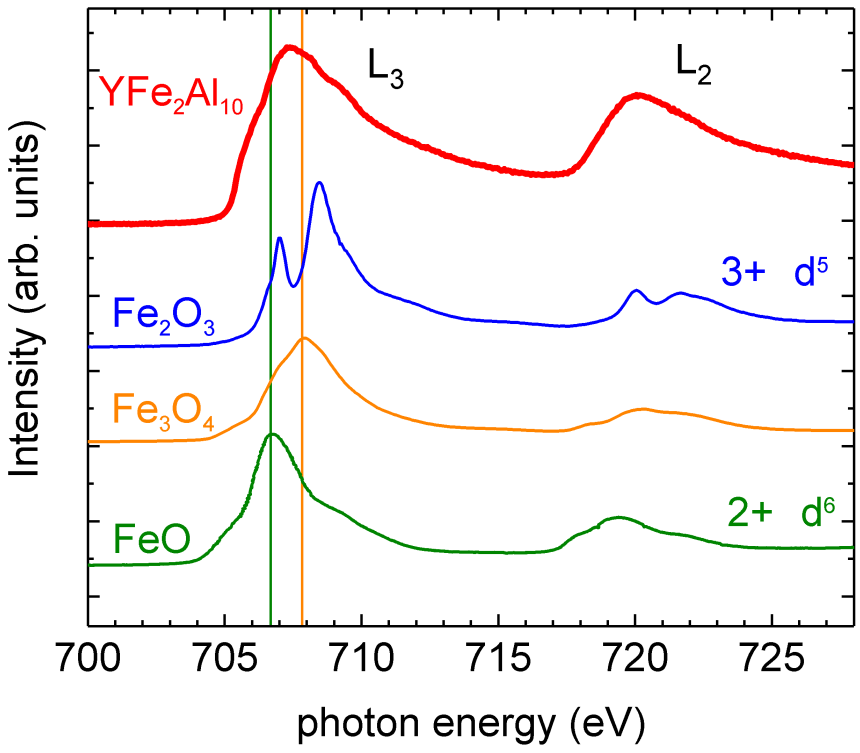

Figure 4.11: *Fe $L_{2,3}$ XAS spectra of YFe_2Al_{10} (red) and reference samples: Fe_2O_3 (blue, (d^5) 3^+ valence), Fe_3O_4 (orange, ($d^{5.33}$) 2.66^+ valence) and FeO (green, (d^6) 2^+ valence). Spectra of the references are courtesy of Zhiwei Hu.*

4.3.3 XMCD analysis and determination of the Fe magnetic moments

The XMCD measurement was performed with the field **B** parallel to the c and to the b crystallographic axes at temperatures of 3, 12, 30 K and with fields of 2 and 6 T.

We will now describe the application of sum rules to the Fe $L_{2,3}$ absorption edge. The discussion is based on what is reported in Ref. [48], where the authors experimentally confirmed the sum rules derived in Ref.s [46, 47] and reported in Sec. 2.1.2.

As an example, we will consider the Fe $L_{2,3}$ edge of YFe_2Al_{10}. Fig. 4.12 shows the spectrum recorded with a magnetic field of 6 T and beam parallel to the c tetragonal axis for both circular polarization C^+ and C^- (a), along with the XMCD $= I_{C^-} - I_{C^+}$ (b).

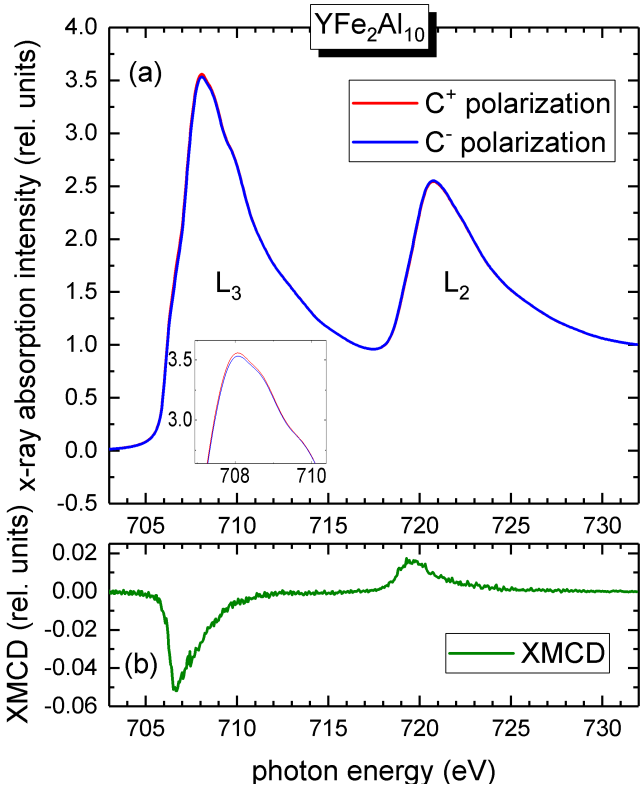

Figure 4.12: *(a) YFe_2Al_{10} Fe $L_{2,3}$ XAS spectrum with circular right and left polarized light. The field of 6 T is applied parallel to the c crystallographic axis and to the beam. In the inset a blow-up of the peak of the L_3 edge is shown, since the difference between the spectra recorded with different polarization is very small. (b) Corresponding XMCD at the $L_{2,3}$ edge.*

In order to apply the sum rules, one should calculate the following integrals.

- The integral q of the XMCD over the whole energy range of the $L_{2,3}$ edge.
- The integral p of the XMCD extended over the L_3 edge alone. The XMCD and its integrals q and p are reported in Fig. 4.13.
- The integral r of the L_3 and L_2 white lines area, which is obtained by integrating the linear polarized spectrum after the subtraction of the edge jumps, extended

over the whole $L_{2,3}$ range. The linear polarized spectrum is obtained as the sum of the spectra for the two polarizations $I_{C^+} + I_{C^-}$. The edge jumps are obtained as the sum of two *arctan* functions. The threshold of the two functions is set to the peak positions of the L_3 and L_2 edges. The heights of each *arctan* is set to $\frac{2}{3}$ and $\frac{1}{3}$ of the average intensity of the last 15 eV of the spectrum, according to their quantum degeneracy $(2j + 1)$. The linear polarized spectrum, background and integral r are shown in Fig. 4.14.

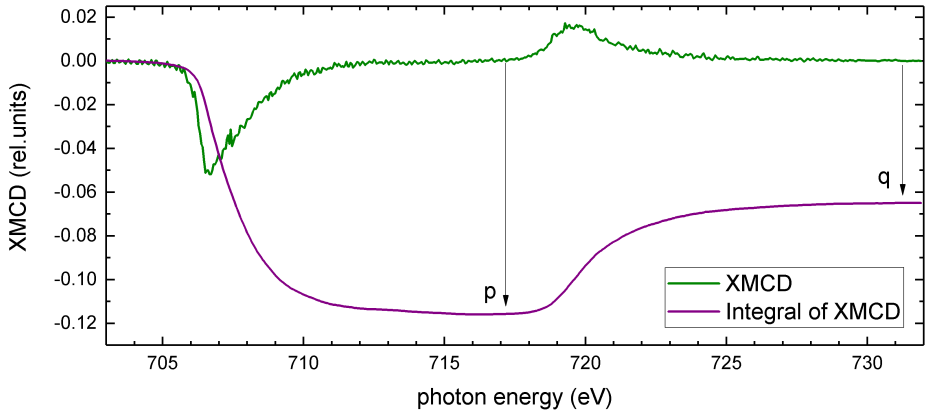

Figure 4.13: *XMCD (green) and its integral (purple). The values of q and p are highlighted by arrows.*

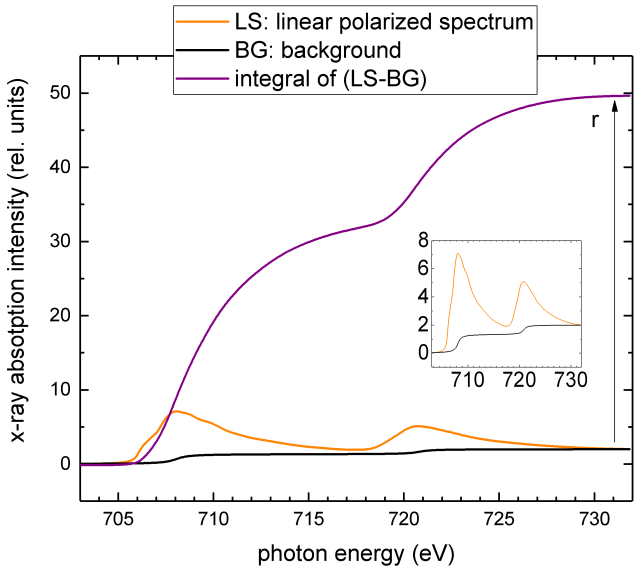

Figure 4.14: *Linear polarized spectrum (orange), edge jumps (black) and integral of the linear polarized spectrum once the edge jumps are subtracted (purple). The value of r is highlighted by the arrow. The inset shows the linear polarized spectrum and the edge jumps alone.*

The integration of the L_3 edge alone is done up to about 717 eV photon energy, while the integration over the whole $L_{2,3}$ range is done up to about 732-733 eV. Once these integrals have been computed, the angular and spin magnetic moments in units of Bohr magnetons per atom can be calculated as:

$$m_{orb} =< L_z >= -4q\frac{10 - n_{3d}}{3r} \tag{4.1}$$

$$m_{spin} = 2 < S_z >= -\frac{(6p - 4q)(10 - n_{3d})}{3r}$$

where the intra-atomic magnetic dipole moment expectation value $< T_z >$ has been neglected and n_{3d} is the number of electrons in the $3d$ sub-shell. The total moment along the field direction in Bohr magnetons per atom and the magnetic susceptibility are given by:

$$m_{tot} = m_{orb} + m_{spin} \tag{4.2}$$

$$\chi[emu/mol] = \frac{m_{tot}}{B[Oe]} \cdot (6.0221415 \cdot 100 \cdot 9.27400899) \tag{4.3}$$

We recall that the results of sum rules depend on the number of electrons in the $3d$ shell. As this is not entirely clear, we at first assume the Fe to be in the d^6 configuration. The results of the application of sum rules are reported in Table 4.2. If we assumed Fe to be in a d^7 configuration, as suggested by DMFT, the sum rules yield the values tabulated in Tab. 4.3. The XMCD analysis shows that the Fe magnetic moment is indeed very small for applied fields of 2 and 6 T. As a matter of fact, looking at Tables 4.2 and 4.3, the total moment along the direction of the field $m_{tot} = m_{spin} + m_{orb}$ is between about 0.005 and 0.05 μ_B per Fe atom. At 6 T and 3 K the susceptibility is flat (see Fig. 4.2) and the moments saturated: from XMCD we get 0.04 and 0.03 μ_B, for $n_{3d} = 6$ and $n_{3d} = 7$ respectively. The saturation moment in units of μ_B is in general given by:

$$m_{sat} = g_j J \tag{4.4}$$

Here g_j is the Landé g-factor. The so-called effective moment, instead, is given by:

$$m_{eff} = g_j\sqrt{J(J+1)} \tag{4.5}$$

For simplicity, let us consider the case of $J = S$, so that $m_{eff} = 2\sqrt{S(S+1)}$. Since the values m_{tot} of the moment determined at 6 T and 3 K are the saturated ones, we can say $m_{tot} = m_{sat} = 2S$. An effective moment of 0.3-0.4 μ_B has been determined in Ref.s [73, 71]. This would entail a value of the saturated moment m_{tot} = 0.044-0.077 μ_B, which is in agreement with our values at 6 T and 3 K (0.04 and 0.03 μ_B).

Figures 4.15 and 4.16 show the susceptibilities for 6 and 2 T as obtained from the XMCD data, one calculated for $n_{3d} = 6$ and one for $n_{3d} = 7$. The slightly smaller χ values that correspond to the calculation with $n_{3d} = 7$ are in better agreement with the susceptibility as measured with a susceptometer, so that XMCD points towards a d^7 configuration, in agreement with the DMFT calculation. There is no evidence of anisotropy between the b and c axis from the XMCD derived susceptibility.

However, XMCD confirms that the magnetic moments come from the Fe atoms in YFe_2Al_{10} and that the saturation of the magnetic susceptibility with applied magnetic field is indeed a feature of the Fe ions.

B = 6 T, $n_{3d} = 6$			
T [K]	χ [10^{-3}emu/mol]	m_{orb} [$10^{-3}\mu_B$/atom]	m_{spin} [$10^{-3}\mu_B$/atom]
3	4.1	7.7	36.3
12	3.9	7.1	35.1
30	2.4	5.1	20.2
3	4.5	7.1	40.9
12	2.5	6.6	19.9
30	1.7	1.6	17.1
B = 2 T, $n_{3d} = 6$			
T [K]	χ [10^{-3}emu/mol]	m_{orb} [$10^{-3}\mu_B/atom$]	m_{spin} [$10^{-3}\mu_B/atom$]
3	8.1	5.1	23.9
12	4.5	1.8	14.5
3	7.4	8.4	18.1
12	2.8	0.47	9.7
30	2.1	0.93	6.4

Table 4.2: *Results of the application of sum rules to the Fe $L_{2,3}$ edge assuming an occupation $n_{3d} = 6$ of the 3d shell. The susceptibility χ, the orbital m_{orb} and spin m_{spin} magnetic moments are reported, for **B** parallel to the c (in red) and b (in blue) axes.*

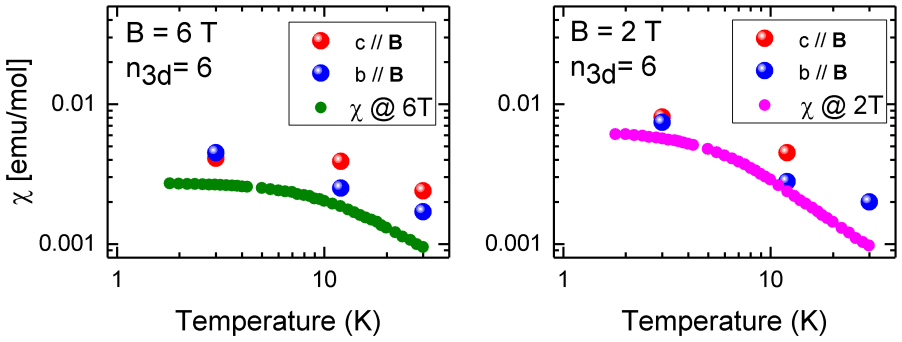

Figure 4.15: *Magnetic susceptibility as derived from the sum rules for applied fields of 6 T (a) and 2 T (b) parallel to the c (red) and b (blue) axes. An occupation $n_{3d} = 6$ of the 3d shell was assumed. The green points in (a) and magenta points in (b) represent the susceptibility as measured with a susceptometer in Ref. [16] for 6T and 2T respectively (they are also plotted in Fig. 4.2).*

B = 6 T, $n_{3d} = 7$			
T [K]	χ [10^{-3}emu/mol]	m_{orb} [$10^{-3}\mu_B$/atom]	m_{spin} [$10^{-3}\mu_B$/atom]
3	3.1	5.8	27.3
12	2.9	5.2	26.2
30	1.8	3.8	15.1
3	3.4	5.3	30.8
12	1.9	5	14.9
30	1.3	1.2	12.7
B = 2 T, $n_{3d} = 7$			
T [K]	χ [10^{-3}emu/mol]	m_{orb} [$10^{-3}\mu_B/atom$]	m_{spin} [$10^{-3}\mu_B/atom$]
3	6.1	3.8	18
12	3.4	1.3	10.8
3	5.6	6.3	13.6
12	2.1	0.35	7.2
30	1.5	0.7	4.8

Table 4.3: *Results of the application of sum rules to the Fe $L_{2,3}$ edge assuming an occupation $n_{3d} = 7$ of the 3d shell. The susceptibility χ, the orbital m_{orb} and spin m_{spin} magnetic moments are reported, for **B** parallel to the c (in red) and b (in blue) axes.*

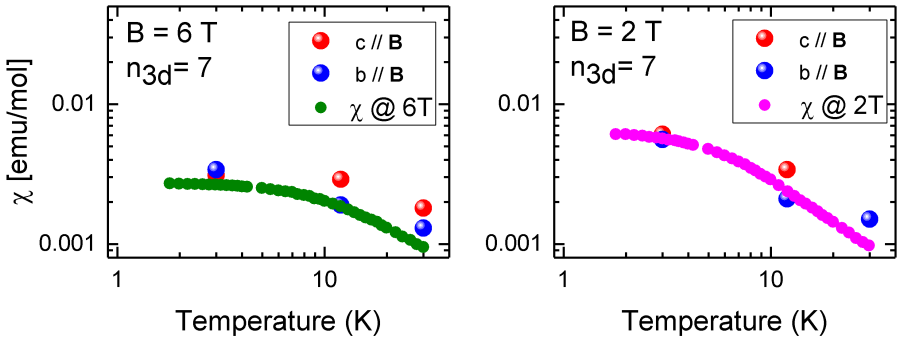

Figure 4.16: *Magnetic susceptibility as derived from the sum rules for applied fields of 6 T (a) and 2 T (b) parallel to the c (red) and b (blue) axes. An occupation $n_{3d} = 7$ of the 3d shell was assumed. The green points in (a) and magenta points in (b) represent the susceptibility as measured with a susceptometer in Ref. [16] for 6T and 2T respectively (they are also plotted in Fig. 4.2).*

4.4 Summary

In this section we briefly summarize our findings on the magnetic character of the Fe atoms in YFe_2Al_{10} and their role in the electronic structure.

DMFT provides a reasonable fit of the experimental VB spectrum. However, the width of the calculated main Fe $3d$ peak is too broad. A U values of 4 eV produces a smaller peak width than the calculation with $U = 0$ eV, but the peak position is too close to the Fermi edge. A U value of e.g. 1 or 2 eV may provide a better fit. Nevertheless, the issue of an excessively large peak width still has to be resolved.

The comparison of the Fe $L_{2,3}$ XAS data of YFe_2Al_{10} with oxide reference samples suggests that the configuration (valence) of Fe in YFe_2Al_{10} is close to d^6 (2^+) but not to d^7.

The magnetic field dependence of the low temperature susceptibility in YFe_2Al_{10} has been confirmed; by increasing the field the static susceptibility becomes smaller. XMCD even reproduces the size of the static susceptibility accurately by assuming a d^7 configuration, thus proving that its saturation with applied field is a feature of Fe in $YFe2_2Al_{10}$. The conclusion of the experiments could be that the Fe is very much like a d^6 configuration according to XAS but that there seems to be quite charge fluctuations so that it is possibly effectively a d^7 and therefore the susceptibility calculated by assuming a d^7 configuration fits better than the d^6 one. The high field (6 T) and low temperature (3 K) calculated moments are in accordance with the effective magnetic moments determined in e.g. neutron scattering or by fitting the high-temperature susceptibility.

The results of these measurements have stimulated further DMFT calculations, aiming at reproducing the PES valence band data.

Chapter 5

Conclusions

In this thesis aspects of the crystal-field of $CeCu_2Si_2$ and of magnetism, valence and correlations of YFe_2Al_{10} have been investigated. In the following we summarize our findings and suggest possible future developments.

The ground-state wave-function of $CeCu_2Si_2$ in the mK regime has been probed with linear polarized soft XAS at the Ce $M_{4,5}$ edge and determined as a Γ_7 state with mixing parameter $|\alpha| = 0.58$, by fitting the experimental LD with full-multiplet single-ion calculations. The knowledge of the $-$ character of the Γ_7 ground-state from previous NIXS measurements [64] and of the crystal-field splittings from INS ($\approx 30\,\mathrm{meV}$) [62] allow for the complete determination of the crystal-field scheme in the mK regime:

$$\begin{aligned}
\mathrm{ground-state}: \ \Gamma_7^- &= 0.58 \left|\pm\frac{5}{2}\right\rangle - 0.81 \left|\mp\frac{3}{2}\right\rangle \\
1^{\mathrm{st}}\ \mathrm{excited}: \ \Gamma_7^+ &= 0.81 \left|\pm\frac{5}{2}\right\rangle + 0.58 \left|\mp\frac{3}{2}\right\rangle \\
2^{\mathrm{nd}}\ \mathrm{excited}: \ \Gamma_6 &= \left|\pm\frac{1}{2}\right\rangle
\end{aligned}$$

The experimental LD is unchanged from 250 mK to 5 K, then shows a slight increase at 25 K and decreases as temperature is raised to 150 and 250 K, due to thermal population of excited crystal-field states. The full-multiplet single-ion simulated LD reproduces well the experimental behaviour by just taking into account thermal population of excited-crystal field states: the overall trend of the LD can be explained in these terms and the ground-state wave-function is not subject to major changes in the temperature range considered here.

The small deviation from thermal occupation that possibly exists at 25 K has been discussed in terms of hybridization of f and conduction electrons. The smaller LD at temperatures below 25 K could be due to the larger amount of f^0 at low temperature or be explained in terms of a 3% intermixing of the excited Γ_6 state into the Γ_7^- ground-state, although it seems unlikely in view of a Kondo temperature of only 10 to 20 K. The intermixing of the Γ_7^+ excited state can be excluded, since it would yield the wrong temperature trend of the linear dichrosim. Finally, a possible Γ_7^--Γ_7^+ orbital reoccupation at low temperature seems unlikely, since the measured LD below 150 K exhibits no substantial change.

More temperature points between 10 and 100 K are needed to accurately monitor the effect of hybridization around 25 K. The higher 25 K LD could be an artifact of experimental origin. Future new experiments are already scheduled. Nevertheless, linear

polarized soft XAS has proven a powerful method to probe the crystal-field ground-state with high precision. The technique was also applied to $CeCoIn_5$ during the same beam-time at the DEIMOS beamline in synchrotron SOLEIL, but a bad cleave did not allow for the acquisition of good enough data. In the future, it will be interesting to probe the ground-state wave-function and the impact of hybridization for other Ce heavy-fermion compounds, such as $CeCoIn_5$.

The VB PES spectra of YFe_2Al_{10} have been acquired at 1486.7 and 664.2 eV photon energies, and compared with DFT and DMFT calculations, performed by P. Hansmann at MPI CPfS. In spite of an excessively large inherent broadening of all calculations, the position of the main peak in the VB is better reproduced when considering no correlations (DMFT with U=0 eV). The DMFT with U=4 eV has a smaller width of the main peak, bu its position is shifted towards the Fermi edge. A value of U of about 1 or 2 eV should be able to fit the peak position correctly. This is a recently started project, where all calculations are still at a preliminary stage. Further refinements of the calculations, in order to correctly fit the peak position and width of the PES VB, are currently object of theoretical efforts at MPI CPfS.

The XAS spectrum at the Fe $L_{2,3}$ edge, compared to iron oxide references, suggests that the valence of Fe in YFe_2Al_{10} is slightly larger than 2^+ (d^6 configuration), but smaller than 2.66^+. This does not comply to the configuration distribution given by DMFT (d^7), but there seems to be quite large charge fluctuations.

The Fe $L_{2,3}$ XMCD analysis reveals a susceptibilty that saturates at high magnetic fields in accordance with previous susceptometry measurements, even as far as its size is concerned if we assume $n_{3d} = 7$. Very small magnetic moments per Fe atom are predicted by XMCD (0.005 to 0.05 μ_B). The effective magnetic moments, estimated on the basis of the high field and low temperature measured saturated moments, are in accordance with the effective magnetic moments determined in e.g. neutron scattering or by fitting the high-temperature static susceptibility.

Bibliography

[1] J. Kondo. The electrical resistance of gold, copper and lead at low temperatures. *Physica.*, 1:1115, 1934.

[2] H.R. Ott, O. Marti, and F. Hulliger. Low temperature thermal conductivity of $CeAl_3$. *Solid State Commun.*, 49(12):1129, 1983.

[3] D. I. Khomskii. *Basic aspects of the quantum theory of solids: order and elementary excitations.* Cambridge University Press, 2010.

[4] F. Strigari. *Hybridization and crystal-field effects in Kondo insulators studied by means of core-level spectroscopy.* PhD thesis, Cologne, 2015.

[5] P. Koerner. Diploma thesis, Cologne, 2008.

[6] P. Ohresser, E. Otero, F. Choueikani, K. Chen, S. Stanescu, F. Deschamps, T. Moreno, F. Polack, B. Lagarde, J.-P. Daguerre, F. Marteau, F. Scheurer, L. Joly, J.-P. Kappler, B. Muller, O. Bunau, and P. Sainctavit. DEIMOS: a beamline dedicated to dichrosim measurements in the 350-2500 eV energy range. *Rev. Sci. Instr.*, (85):013106, 2014.

[7] DEIMOS web page: https://www.synchrotron soleil.fr/en/beamlines/deimos.

[8] J. Gegner. PhD Thesis,University of Cologne, 2010.

[9] H. S. Jeevan. *Crystal Growth and Investigation of $CeCu_2Si_2$ and $YbRu_2Ge_2$: Competition/Co-existence of Superconducting, Dipolar and Quadrupolar order.* PhD thesis, TU Dresden, 2010.

[10] B. Batlogg, J. P. Remeika, A. S. Cooper, and Z. Fisk. Magnetism and superconductivity in $CeCu_2Si_2$ single crystals. *J. Appl. Phys*, (55):1984, 1984.

[11] K. A. Gschneidner and L. Eyring. *Handbook on the Physics and Chemistry of Rare Earths.*

[12] F. Steglich, J. Aarts, C. D. Bredl, W. Lieke, D. Meschede, W. Franz, and H. Schafer. Superconductivity in the Presence of Strong Pauli Paramagnetism: $CeCu_2Si_2$. *Phys. Rev. Lett*, 43(25):1892–1896, 1979.

[13] O. Stockert, J. Arndt, E. Faulhaber, C. Geibel, H. S. Jeevan, S. Kirchner, M. Loewenhaupt, K. Schmalzl, W. Schmidt, Q. Si, and F. Steglich. Magnetically driven superconductivity in $CeCu_2Si_2$. *Nat. Phys.*, 7:119–124, 2010.

[14] L.V. Pourovskii, P. Hansmann, M. Ferrero, and A. Georges. Theoretical prediction and spectroscopic fingerprints of an orbital transition in $CeCu_2Si_2$. *Phys. Rev. Lett.*, 112:106407, 2014.

[15] L. H. Tjeng, E.-J. Cho S.-J. Oh, H.-J. Lin, C. T. Chen, G.-H. Gweon, J.-H. Park, J. W. Allen, T. Suzuk, M. S. Makivic, and D. L. Cox. Temperature dependence of the Kondo resonance in $YbAl_3$. *Phys. Rev. Lett.*, 71(9):1419, 1993.

[16] L. S. Wu, M. S. Kim, K. Park., A. M. Tsvelik, and M. C. Aronson. Quantum critical fluctuations in layered YFe_2Al_{10}. *PNAS*, 111(39):14088, 2014.

[17] M.B.Trzhaskovskaya, V.I.Nefedov, and V.G.Yarthemsky. Photoelectron angular distribution parameters for elements Z=1 to Z=54 in the photoelectron energy range 100-5000 eV. *Atomic Data and Nuclear Data Tables*, (77):97, 2001.

[18] M.B.Trzhaskovskaya, V.K.Nikulin, V.I.Nefedov, and V.G.Yarzhemsky. Non-dipole second order parameters of the photoelectron angular distribution for elements Z=1-100 in the photoelectron energy range 1–10 keV. *Atomic Data and Nuclear Data Tables*, (92):245, 2006.

[19] V. Anisimov and Y. Izyumov. *Electronic Structure of Strongly Correlated Materials.* Springer, 2010.

[20] P. W. Anderson. Localized magnetic states in metals. *Phys. Rev.*, 124:41, 1961.

[21] J. Kondo. Resistance minimum in dilute magnetic alloys. *Prog. of Theor. Phys.*, 32:37, 1964.

[22] G. R. Stewart. Heavy-fermion systems. *Rev. Mod. Phys.*, 56:755, 1984.

[23] P. Misra. *Heavy-fermion systems.* Handbook of metal physics. Elsevier, 2008.

[24] S. Doniach. The Kondo lattice and weak antiferromagnetism. *Physica B+C*, 91:231, 1977.

[25] K. Andres, J. E. Graebner, and H. R. Ott. 4f virtual-bound-state formation in $CeAl_3$ at low temperatures. *Phys. Rev. Lett.*, 35:1779, 1975.

[26] H. V. Löhneysen, T. Pietrus, G. Portisch, H. G. Schlager, A. Schröder, M. Sieck, and T. Trappmann. Non-Fermi-liquid behavior in a heavy-fermion alloy at a magnetic instability. *Phys. Rev. Lett.*, 72:3262, 1994.

[27] H. Q. Yuan, F. M. Grosche, M. Deppe, C. Geibel, G. Sparn, and F. Steglich. Observation of two distinct superconducting phases in $CeCu_2Si_2$. *Science*, 302:2104–2107, 2003.

[28] C. Petrovic, P. G. Pagliuso, M. F. Hundley, R. Movshovich, J. L. Sarrao, J. D. Thompson, Z. Fisk, and P. Monthoux. Heavy-fermion superconductivity in $CeCoIn_5$ at 2.3 K. *J. Phys.: Condens. Matter*, 13:L337, 2001.

[29] N. D. Mathur, F. M. Grosche, S. R. Julian, I. R. Walker, D. M. Freye, R. K. W. Haselwimmer, and G. G. Lonzarich. Magnetically mediated superconductivity in heavy fermion compounds. *Nature*, 304:39–43, 1998.

[30] F. Grosche, S. Julian, N. Mathur, and G. Lonzarich. Magnetic and superconducting phases of $CePd_2Si_2$. *Physica B: Condens. Matter*, 223-224:50, 1996.

[31] R. Movshovich, T. Graf, D. Mandrus, J. D. Thompson, J. L. Smith, and Z. Fisk. Super-conductivity in heavy-fermion $CeRh_2Si_2$. *Phys. Rev. B*, 53:8241, 1996.

[32] H. Schneider and D. Wohlleben. Electrical and thermal conductivity of $CePd_3$, YPd_3, $GdPd_3$ and some dilute alloys of $CePd_3$ with Y and Gd. *Z. Phys. B: Condens. Matter.*, (44):193, 1981.

[33] M.Sundermann, F.Strigari, T.Willers, J.Weinen, Y.F.Liao, K.-D.Tsuei, N.Hiraoka, H.Ishii, H.Yamaoka, J.Mizuki, Y.Zekk, E.D.Bauerg, .L.Sarrao, J.D.Thompson, P.Lejay, Y.Muroi, .Yutani, T.Takabatake, A. Tanaka, N. Hollmann, and L.H. Tjeng andA. Severing. Quantitative study of the f occupation in $CeMIn_5$ and other cerium compounds with hard x-rays. *J. Electron Spectrosc.*, (209):1, 2016.

[34] H. Bethe. Termaufspaltung in kristallen. *Annalen der Physik*, 395:133, 1929.

[35] J. Van Vleck. Theory of the variations in paramagnetic anisotropy among different salts of the iron group. *Phys. Rev.*, 42(2):208, 1932.

[36] C. J. Ballhausen. *Introduction to ligand field theory.* McGraw-Hill, New York, 1962.

[37] R. D. Cowan. *The theory of atomic structure and spectra.* University of California Press, 1981.

[38] F. de Groot and A. Kotani. *Core Level Spectroscopy of Solids.* CRC Press, BocaRaton, 2008.

[39] M. Sacchi, F. Sirotti, and G. Rossi. Crystal field induced linear dichroism in the 3d x-ray absorption of rare-earths. *Solid State Commun.*, 81(12):977, 1992.

[40] B.T. Thole, G. van der Laan, and G. A. Sawatzky. Strong magnetic dichroism predicted in the $M_{4,5}$ x-ray absorption spectra of magnetic rare-earth materials. *Phys. Rev. Lett.*, (55):2086, 1985.

[41] G. van der Laan, B.T. Thole, , G. A. Sawatzky, J. B. Goedkoop, J. C. Fuggle, J.-M. Esteva, R. Karnatak, J. P. Remeika, and H. A. Dabkowska. Experimental proof of magnetic x-ray dichroism. *Phys. Rev. B*, 34(9):6529, 1986.

[42] G. Schütz, W. Wagner, W. Wilhelm, P. Kienle, R. Zeller, R. Frahm, and G. Materlik. Absorption of circularly polarized x rays in iron. *Phys. Rev. Lett.*, 58(7):737, 1987.

[43] F. Baudelet, E. Dartyge, A. Fontaine, C. Brouder, G. Krill, J.P. Kappler, and M. Piecuch. Magnetic properties of neodynium atoms in Nd-Fe multilayers studied by magnetic x-ray dichroism on Nd L_{II} and Fe K edges. *Phys. Rev. B*, 43(7):5857, 1991.

[44] C. T. Chen, F. Sette, Y. Ma, and S. Modesti. Soft-x-ray magnetic circular dichroism at the $L_{2,3}$ edges of nickel. *Phys. Rev. B*, 42(11):7262, 1990.

[45] T. Jo and G. A. Sawatzky. Ground state of ferromagnetic nickel and magnetic circular dichroism in Ni 2p core x-ray-absorption spectroscopy. *Phys. Rev. B*, 43(10):8771, 1991.

[46] B. T. Thole, P. Carra, F. Sette, , and G. van der Laan. X-ray circular dichroism as a probe of orbital magnetization. *Phys.Rev.Lett.*, (68):1943, 1992.

[47] P. Carra, B. T. Thole, M. Altarelli, and X. Wang. X-ray circular dichroism and local magnetic fields. *Phys.Rev.Lett.*, (70):694, 1993.

[48] C. T. Chen, Y. U. Idzerda, H.-J. Lin, N. V. Smith, G. Meigs, E. Chaban, E. Pellegrin G. H. Ho, and F. Sette. Experimental confirmation of the x-ray magnetic circular dichroism sum rules for iron and cobalt. *Phys. Rev. Lett.*, (75):152, 1995.

[49] P.Hansmann, A.Severing, Z.Hu, M.W.Haverkort, C.F.Chang, S.Klein, A.Tanaka, H.H. Hsieh, H.-J.Lin, C.T.Chen, B.Fåk, P.Lejay, and L.H.Tjeng. Determining the crystal-field ground state in rare earth heavy fermion materials using soft-x-ray absorption spectroscopy. *Phys.Rev.Lett.*, (100):066405, 2008.

[50] R. Nakajima, J. Stöhr, and Y. U. Idzerda. Electron-yield saturation effects in L-edge x-ray magnetic circular dichroism spectra of Fe, Co, and Ni. *Phys. Rev. B*, 59(9):6421, 1999.

[51] M. W. Haverkort. *Spin and orbital degrees of freedon in transtion metal oxides and oxide thin films studied by soft x-ray absorption spectroscopy.* Ph.D. thesis, Cologne, 2005.

[52] M. W. Haverkort. *Quanty* for core level spectroscopy excitons, resonances and band excitations in time and frequency domain. *J. Phys.: Conf. Ser.*, (712):12001, 2016.

[53] S.Doniach and M.Sunjic. Many-electron singularity in x-ray photoemission and x-ray line spectra from metals. *J. Physics C : Solid State Phys.*, (3):285, 1970.

[54] D. A. Shirley. High-resolution x-ray photoemission spectrum of the valence bands of gold. *Phys. Rev. B*, (5):4709, 1972.

[55] S. Hüfner. *Photoelectron Spectroscopy: Principles and Applications.* Advanced Texts in Physics. Springer, Berlin-Heidelberg, 2003.

[56] J.P. Rueff, S. Raymond, M. Taguchi, M. Sikora, J.-P. Itieand F. Baudelet, D. Braithwaite, G. Knebel, and D. Jaccard. Pressure-induced valence crossover in superconducting $CeCu_2Si_2$. *Phys. Rev.. Lett.*, 106:185405, 2011.

[57] G. Pang, M. Smidman, J.Zhang Si, L. Jiao Si, Z. Weng Si, E. M. Nica Si, Y. Chen Si, W. Jiang Si, Y. Zhang Si, W. Xie Si, H. S. Jeevan Si, H. Lee Si, P. Gegenwart Si, F. Steglich Si, Q. Si, and H. Yuan. Fully gapped d-wave superconductivity in $CeCu_2Si_2$. *Proceedings of the National Academy of Sciences*, (115):5343, 2018.

[58] O. Stockert and F. Steglich. Unconventional quantum criticality in heavy-fermion compounds. *Annual Review of Condensed Matter Physics*, (2):79, 2011.

[59] S. Kittaka, Y. Aoki, Y. Shimura, T. Sakakibara, S. Seiro, C. Geibel, F. Steglich, H. Ikeda, and K. Machida. Multiband superconductivity with unexpected deficiency of nodal quasiparticles in $CeCu_2Si_2$. *Phys. Rev. Lett.*, (112):067002, 2014.

[60] T. Yamashita, T. Takenaka, Y. Tokiwa, J. A. Wilcox, Y. Mizukami, D. Terazawa, Y. Kasahara, S. Kittaka, T. Sakakibara, M. Konczykowski, S. Seiro, H. S. Jeevan, C. Geibel, C. Putzke, T. Onishi, H. Ikeda, A. Carrington, T. Shibauchi, and Y. Matsuda. Fully gapped superconductivity with no sign change in the prototypical heavy-fermion $CeCu_2Si_2$. *Sci. Adv.*, (3), 2017.

[61] T. Takenaka, Y. Mizukami, J. A. Wilcox, M. Konczykowski, C. Geibel S. Seiro, Y. Tokiwa, Y. Kasahara, C. Putzke, Y. Matsuda, A. Carrington, and T. Shibauchi. Full-gap superconductivity robust against disorder in heavy-fermion $CeCu_2Si_2$. *Phys. Rev. Lett.*, (119):077001, 2017.

[62] E. A. Goremychkin and R. Osborn. Crystal-field excitations in $CeCu_2Si_2$. *Phys. Rev. B*, 47(21):280–290, 1993.

[63] S. Horn, E. Holland-Moritz, M. Loewenhaupt, F. Steglich, H. Scheuer, A. Benoit, and J. Flouquet. Magnetic neutron scattering and crystal-field states in $CeCu_2Si_2$. *Phys. Rev. B*, (23):3171, 1981.

[64] T. Willers, F. Strigari, N. Hiraoka, Y. Q. Cai, M. W. Haverkort, K.-D. Tsuei, Y. F. Liao, S. Seiro, C. Geibel, F. Steglich, L. H. Tjeng, and A. Severing. Determining the in-plane orientation of the ground-state orbital in $CeCu_2Si_2$. *Phys. Rev. Lett.*, 109:046401, 2012.

[65] M. Sundermann, F. Strigari, T. Willers, H. Winkler, Prokoev, J. M. A. Ablett, J.-P. Ruff, D. Schmitz, E. Weschke, M. Sala-Moretti, A. Al-Zein, A. Tanaka, M. W. Haverkort, D. Kasinathan, L. H. Tjeng, S. Paschen, and A. Severing. $CeRu_4Sn_6$: a strongly correlated material with nontrivial topology. *Scientic Reports*, (5):17937, 2015.

[66] M. Sundermann, A. Amorese, F. Strigari, B. Leedahl, L. H. Tjeng, M. W. Haverkort, H. Gretarsson, H. Yava, M. Moretti Sala, E. D. Bauer, P. F. S. Rosa, J. D. Thompson, and A. Severing. Orientation of the ground-state orbital in $CeCoIn_5$ and $CeRhIn_5$. *Phys. Rev. B*, (99):235143, 2019.

[67] M. W. Havekort. *Quanty* for core level spectroscopy - excitons, resonances and band excitations in time and frequency domain. *J. Phys.: Conf. Ser.*, 712:012001, 2006.

[68] O. Gunnarsson and K. Schonhammer. Electron spectroscopies for Ce compounds in the impurity model. *Phys. Rev. B*, 28(8):4315–4341, 1983.

[69] N. E. Bickers, D. L. Cox, and J. W. Wilkins. Self-consistent large-N expansion for normal-state properties of dilute magnetic alloys. *Phys. Rev. B*, (36):2016, 1987.

[70] K. Kummer, C. Geibel, C. Krellner, G. Zwicknagl, C. Laubschat, N.B. Brookes, and D.V. Vyalikh. Similar temperature scale for valence changes in Kondo lattices with different Kondo temperatures. *Nat. Commun.*, 2011:9, 2018.

[71] K. Park, L. S. Wu, Y. Janssen, M. S. Kim, C. Marques, and M. C. Aronson. Field-tuned Fermi liquid in quantum critical YFe_2Al_{10}. *Phys. Rev. B*, (84):094425, 2011.

[72] P. Khuntia, A. Strydom, F. Steglich, and M. Baenitz. Quenching of spin fluctuations in the 3d and 4f aluminides YFe_2Al_{10} and $YbFe_2Al_{10}$: a comparative ^{27}NMR and specific heat study. *Phys. Status Solidi*, 250(3):528, 2013.

[73] W. J. Gannon, L. S. Wub, I. A. Zaliznyakc, W. H. Xu, A. M. Tsvelik, Y. Qiu, J. A. Rodriguez-Rivera, and M. C. Aronson. Local quantum phase transition in YFe_2Al_{10}. *PNAS*, 115(27):6995, 2018.

[74] A. Kerkau, I. L. Wu, K. Park, Yurii P., M. Brando, M. C. Aronson, and G. Kreiner. Crystal structure of yttrium iron aluminium (1/2/10), YFe_2Al_{10}. *New Cryst. Struct.*, (227):289, 2012.

[75] P. Khuntia, A. M. Strydom, L. S. Wu, M. C. Aronson, F. Steglich, , and M. Baenitz. Field-tuned critical fluctuations in YFe_2Al_{10}: evidence from magnetization, ^{27}Al NMR, and NQR investigations. *Phys. Rev. B*, (86):220401, 2012.